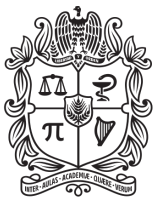

UNIVERSIDAD
NACIONAL
DE COLOMBIA

Desarrollo e implementación de un método libre de base para el estudio de efectos cuánticos nucleares (Nu-APMO: Numerical Any Particle Molecular Orbital)

Edwin Fernando Posada Correa

Universidad Nacional de Colombia
Facultad de Ciencias, Departamento de Química
Bogotá, Colombia
2017

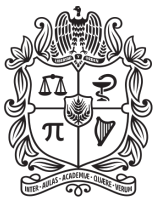

UNIVERSIDAD
NACIONAL
DE COLOMBIA

Theoretical development and computational implementation of a basis-set-free methodology for the study of nuclear quantum effects (Nu-APMO: Numerical Any Particle Molecular Orbital)

Edwin Fernando Posada Correa

Universidad Nacional de Colombia
Chemistry Department
Bogotá, Colombia
2017

Desarrollo e implementación de un método libre de base para el estudio de efectos cuánticos nucleares (Nu-APMO: Numerical Any Particle Molecular Orbital)

Edwin Fernando Posada Correa

Tesis presentada como requisito para optar al título de:
Doctor en Ciencias Química

Director:
Ph.D., Andrés Reyes Velasco

Grupo de Investigación:
Química Cuántica y Computacional

Universidad Nacional de Colombia
Facultad de Ciencias, Departamento de Química
Bogotá, Colombia
2017

Theoretical development and computational implementation of a basis-set-free methodology for the study of nuclear quantum effects (Nu-APMO: Numerical Any Particle Molecular Orbital)

Edwin Fernando Posada Correa

Thesis presented in partial fullfilment of the requirements for the degree of:
Doctor in Science - Chemistry

Advisor:
Ph.D., Andrés Reyes Velasco

Research Group:
Quantum and Computational Chemistry

Universidad Nacional de Colombia
Chemistry Department
Bogotá, Colombia
2017

Acknowledgments

I gratefully acknowledge the support of my advisor, Dr. Andrés Reyes, the company of the Quantum and Computational Chemistry group, and the contributions of M.Sc. Félix Moncada for Papers I and III; Dr. Néstor Aguirre for Paper II; M.Sc. Jhonathan Romero for Paper I and Dr. Guiseppe Piero for Chapter 4.

The present work has been possible thanks to the financial support of Colciencias (grant *Becas Doctorados Nacionales*, reference 567) and International Centre for Theoretical Physics (ICTP) (*Training and Research in Italian Laboratories (TRIL) Fellow*, reference 2352). Finally, I would like to thank the support of my family and friends. This thesis is dedicated to them.

Resumen

En este trabajo se propone el método del orbital nuclear molecular para cualquier tipo de partícula libre de base a nivel de teoría Hartree-Fock (APMO-GBHF). Este método esta basado en la metodología basada en grids propuesta por Becke y Dickson[1] y ha sido implementado y paralelizado en un nuevo paquete computacional llamado Nu-APMO. El método ha sido aplicado para calcular las energías y densidades a nivel Hartree-Fock (HF) en varios sistemas electrónicos y multiespecie. Los resultados han mostrado que las energías totales obtenidas con APMO-GBHF son comparables con las correspondientes al límite HF. Adicionalmente, los resultados han arrojado una mejora sustancial en la descripción de la cúspide nuclear en densidades electrónicas y no electrónicas. Este método es el primer paso para desarrollar métodos correlacionados en el marco del método del orbital nuclear molecular para cualquier tipo de partícula sin errores debidos al conjunto base.

Palabras clave:

Métodos libres de base, APMO, métodos basados en grids, límite Hartree-Fock, metodologías multicomponente y cúspide de Kato.

Abstract

In this work, we propose the any-particle molecular orbital grid-based Hartree-Fock approach (APMO-GBHF) as an initial step to realizing APMO explicit correlated Gaussian (APMO-ECG) and APMO second-quantized methods without basis set errors. Our approach is along the lines of the method developed by Becke and Dickson.[1] The method APMO-GBHF has been implemented in a new software named Nu-APMO, which has been parallelized with OpenMP and CUDA frameworks. The proposed methodology has been applied to several electronic and multispecies molecular systems. The results of these calculations have shown that the total Hartree-Fock (HF) energies obtained with APMO-GBHF are comparable with the HF basis-set limit. Additionally, it has been found a considerable improvement of the nuclear cusp description for electronic and non-electronic densities.

Keywords:

Basis-set-free methods, APMO, grid-based methods, Hartree-Fock limit, multicomponent methodologies and Kato's cusp.

Contents

Acknowledgments ix

Abstract xi

Nomenclature xii

1. Introduction 2
- 1.1. Multi-component methodologies . . . 2
- 1.2. Exotic molecules . . . 4
- 1.3. This work . . . 5

2. Theoretical background 6
- 2.1. Any particle molecular orbital (APMO) theory . . . 6
  - 2.1.1. APMO-HF approach . . . 6
- 2.2. Grid-based Hartree-Fock . . . 8
  - 2.2.1. Multicenter numerical integration . . . 8
  - 2.2.2. Poisson's equation for polyatomic molecules . . . 13
  - 2.2.3. Grid-based HF solver . . . 17

3. Theoretical development 19
- 3.1. Extension of the GBHF formulation for APMO . . . 19
- 3.2. Numerical calculation of APMO-GBHF operator . . . 23
  - 3.2.1. One-particle operator . . . 23
  - 3.2.2. Two-particle operators . . . 24
  - 3.2.3. Grid refinement . . . 25
  - 3.2.4. Results . . . 26
- 3.3. Variational optimization for numerical APMO-HF orbitals . . . 28
  - 3.3.1. Calculation of the orbital correction . . . 29
  - 3.3.2. Calculation of new orbitals . . . 30
  - 3.3.3. Results . . . 30

4. Computational implementation 36
- 4.1. Program structure . . . 37
  - 4.1.1. Python interface . . . 38
  - 4.1.2. C++ library . . . 39

4.2. Performance and parallelization 41
4.2.1. Testing configuration and environment 41
4.2.2. Multicenter integrator 42
4.2.3. Two-electronic Coulomb integration 50

5. Results **55**
5.1. Summary of the papers 55

6. Conclusions and perspectives **58**

Appendices **59**

A. Paper I **60**

B. Paper II **68**

C. Paper III **83**

D. Paper IV **93**

1. Introduction

1.1. Multi-component methodologies

In the last decades, many theoretical models have been developed to extend regular electronic structure methods to study atomic and molecular systems comprising electrons and other quantum species.[2–7] In the early stages of these Multi-Component (MC) methodologies, the main goal was to describe hydrogen-bonding systems, hydrogen transfer processes, and small hydrogen-containing molecules beyond the Born-Oppenheimer approximation (BOA). Such description was done by using single-particle molecular orbitals for both electrons and nuclei, allowing a simultaneous quantum-mechanical treatment of those particles. Figure 1-1 illustrates the evolution of MC methodologies. A comprehensive review of MC methodologies can be found in reference.[8]

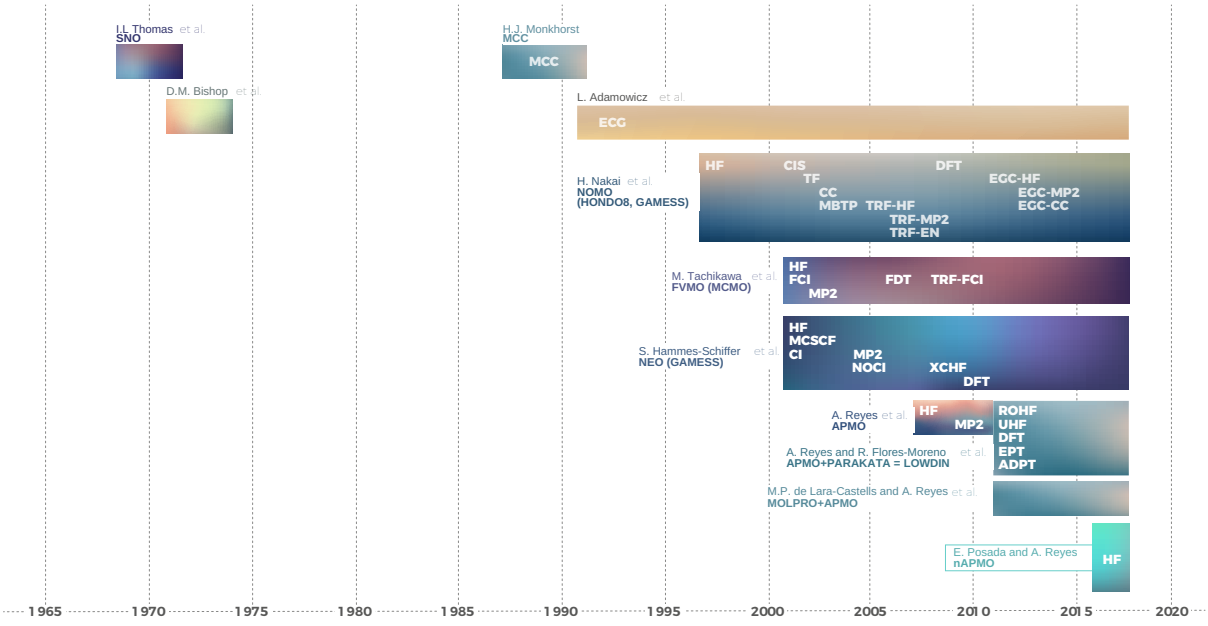

Figure **1-1**.: Scheme illustrating the evolution over the time of methodological and computational MC implementations.

The underlying idea of MC methodologies was put forward in the late 1960s by Thomas

and collaborators.[2, 9] In these contributions, they performed calculations in a mean-field framework for CH_4, NH_3 and H_2O molecules. In these calculations, electrons and hydrogen nuclei were treated quantum-mechanically while heavier nuclei were treated as point charges.

Over the past few years, there has been a remarkable interest in MC methodologies as a possible way to describe isotopic effects or hydrogen tunneling. Tachikawa *et al.*[3] presented the MC equations for nuclei and electrons under the name, dynamically extended molecular orbital (DEMO), and applied the method to the $[e^+;F^-]$, HF and DF systems. Later, Tachikawa and Osamura [10] performed the first mean field MC calculations on different isotopomers of H_2 as well as of those of LiH in which all the nuclei were treated quantum-mechanically. These works led to a series of applications on the isotope effects in hydrogen-containing molecules. Furthermore, Hammes-Schiffer *et al.* implemented the MC method under the acronym NEO (nuclear-electronic orbital), and developed the Configuration Interaction (NEO-CI), the Møller Plesset perturbation theory of second order (NEO-MP2) and the Multi-configurational Self-consistent Field (NEO-MCSCF) versions of the MC approach to include interparticle correlations.[7, 11–16]

The use of MC methodologies to analyze systems beyond BOA rises new conceptual difficulties not appearing in BOA methods such as: (a) the incorrect description of rotational and translational motion, due to the non-separability of the MC wave-function into internal and center-of-mass (CM) parts and (b) the inability to describe the nuclear-electronic cusps efficiently.[17] To face these difficulties, Nakai *et al.* developed the nuclear orbital plus molecular orbital (NOMO) method, including the removal of translational and rotational contamination from the Hamiltonian.[4, 18–21] In addition, Hammes-Schiffer *et al.*, implemented the explicitly correlated Hartree-Fock (NEO-XCHF) MC approach to improving the description of the nuclear-electronic cusp.[22]

More recently, the Any-Particle Molecular Orbital (APMO) approach was developed.[6, 23] Restricted HF (APMO-RHF) equations were implemented in the original code [6] which was extended to include interparticle correlations at MP2 level (APMO-MP2) [23] and to remove the translational contamination at HF level.[24] The main advantage of the APMO implementation is its capability of describing systems containing any combination of quantum species, allowing the study of atomic or molecular systems containing exotic species such as positrons or negative muons.[25] Further extensions with the PARAKATA code [26] (the LOWDIN package [27]) allowed the description of quantum particles using either Density Functional Theory (DFT) or auxiliary perturbation theory (ADPT), as well as the calculations with the electron propagator theory (EPT).[28] A complete review of LOWDIN package can be found in reference.[27]

In contrast to the application of MC methodologies to analyze molecular systems beyond

BOA, when MC models are used to describe exotic molecules, (*i.e.* molecular systems containing subatomic particles such as positrons, muons, among others) nuclei are treated as point charges under the BOA. Still, the accuracy of MC mean field calculations for these systems is limited as a result of basis set related problems.

Although the application of the MC-translation-free and MC-XCHF methods has provided better results, these applications have revealed the slow convergence of the energies with angular momenta, number of basis functions and positions of such basis functions. Finding an appropriate basis set to represent exotic particles, within the MC models, poses a serious challenge since there are not well established and physically motivated hierarchies for this purpose such as in the electronic counterpart. For instance, in the case of positronic atoms and molecules, due to the high dependence of the basis set on the chemical environment, basis set coefficients, exponent and centers are usually crafted for each system following in many cases the physical or chemical intuition.

The main goal of this contribution is to face those basis set related issues in MC methodologies by changing the representation of the wavefunction. Moreover, to restrict the analysis to basis set related issues, we focus our study on exotic systems.

The explanation of what an exotic system is and an overview of the chosen numerical representation of the MC wavefunction within the APMO framework is featured below.

1.2. Exotic molecules

According to Nature journal, exotic atoms and molecules are forms of basic matter in which one subatomic particle is replaced by another with the same charge. For instance, an electron can be replaced with a muon, a pion or an antiproton. Positronium is obtained by swapping the proton in a hydrogen atom by a positron.[29] In this work we have performed calculations on muonic atoms (*i.e.* atoms in which one electron has been replaced by a negative muon) and the positronium hydride (PsH).

In the case of muonic atoms, we have discriminated analytically the nuclear mass and quantum muon effects on chemical properties of muonic and regular atoms. This study has revealed that the differences in the ionization potentials of isoelectronic muonic atoms and regular atoms are of the order of millielectronvolts. For the valence ionizations of muonic helium and muonic lithium, the nuclear mass effects are more important. On the other hand, for 1s ionizations of muonic atoms heavier than beryllium, the quantum muon effects are more important. Also, this study presents an assessment of the nuclear mass and quantum muon effects on the barrier of $He\mu + H_2$ reaction. Further details of this contribution can be found in Appendix C.

In addition, we have performed APMO grid-based Hartree-Fock (APMO-GBHF) calculations for muonic helium, reporting energies within the millihartree on the HF-limit energies.

On the other hand, we have also analyzed the positronium hydride (PsH) system. This system comprises one proton, two electrons, and a positron. A detailed description of this system can be found in [30–32] and references therein. Our APMO-GBHF reports energies within 10×10^{-4} Hartree to the complete basis set extrapolation (CBS).

Details of these calculations can be found in chapter 3 and in Appendix D.

1.3. This work

In this contribution, we propose the Any-Particle Molecular Orbital grid-based Hartree-Fock (APMO-GBHF) approach as an initial step to realizing APMO explicit correlated Gaussian (APMO-ECG) and APMO second-quantized methods without basis set errors. The development of this approach is along the lines of the method developed by Becke and Dickson[33].

As mentioned before, the application of our methodology to several exotic systems have shown that basis set related problems in the ground state are mitigated since the resulting energies are comparable with those in the complete basis set extrapolation (CBS) of HF limit. In this regard, it is expected a rapid convergence of the energy when static and dynamic correlations come into place through APMO-post-HF and APMO-ECG methods, as a result of the improvement of the ground state orbitals.

This document is organized as follows: In chapter 2, we present the theoretical foundation of this work, including the APMO formalism and the fundamentals on the grid representation including the grid-based integration for polyatomic molecules. Then, in chapter 3, we describe in detail the new theoretical formalism developed within this work. Next chapter 4 we include all technicals details behind the computational implementation of the proposed theory of chapter 3. Then in chapter 5 we summarize the reported results concerning the published and submitted papers. Finally in chapter 6 we provide some conclusions and perspectives.

2. Theoretical background

2.1. Any particle molecular orbital (APMO) theory

2.1.1. APMO-HF approach

In this section, we summarize the equations of the APMO Hartree-Fock (APMO-HF) approach.[6] Let us consider a system containing N^Q fermionic quantum particles and N^C point charge nuclei. The Hamiltonian, H, of this system is written in terms of kinetic and potential energy operators

$$\hat{H} = -\sum_{i}^{N^Q} \frac{1}{2M_i}\nabla^2 + \sum_{i}^{N^Q}\sum_{j>i}^{N^Q} \frac{q_i q_j}{\mathbf{r}_{ij}} + \sum_{i}^{N^Q}\sum_{j}^{N^C} \frac{q_i q_j}{\mathbf{r}_{ij}} + \sum_{i}^{N^C}\sum_{j>i}^{N^C} \frac{q_i q_j}{\mathbf{r}_{ij}}, \tag{2-1}$$

where q_i is the charge of particle i. The first term in equation (2-1) represents the kinetic energy operator of quantum species i with mass M_i, the second term corresponds to the pair interaction between two quantum species. Then, the third term describes the interaction between quantum species and point charges, and finally, the last term denotes the pair potential between two point charges.

At the APMO-HF level of theory, the molecular wave-function, Ψ_0, is expressed as a product of single-configurational wave-functions, Φ^α, for each quantum species α:

$$\Psi_0(\mathbf{r}^\alpha, \ldots, \mathbf{r}^{N^Q}) = \prod_{\alpha}^{N^Q} \Phi^\alpha(\mathbf{r}^\alpha). \tag{2-2}$$

Here, each Φ^α is expressed in terms of molecular orbitals (MO) ψ_i^α, obtained by solving the corresponding Fock equations. The expectation value of the total energy at APMO-HF level of theory, using equations (2-1) and (2-2), is given by

$$\begin{aligned} E_0 &= \langle\Psi_0|\hat{H}|\Psi_0\rangle \\ &= \sum_{\alpha}^{N^Q}\Bigg[-\frac{1}{2M_\alpha}\sum_{i}^{N^\alpha}\langle\Phi^\alpha|\nabla_i^2|\Phi^\alpha\rangle + q_\alpha\sum_{i}^{N^\alpha}\langle\Phi^\alpha|\sum_{j}^{N^C} q_j\mathbf{r}_{ij}^{-1}|\Phi^\alpha\rangle + q_\alpha^2\sum_{i,j>i}^{N^\alpha}\langle\Phi^\alpha|\mathbf{r}_{ij}^{-1}|\Phi^\alpha\rangle \\ &\qquad + \sum_{\beta>\alpha}^{N^Q}\sum_{i}^{N^\alpha}\sum_{j}^{N^\beta} q_\alpha q_\beta\langle\Phi^\alpha\Phi^\beta|\mathbf{r}_{ij}^{-1}|\Phi^\alpha\Phi^\beta\rangle\Bigg] + \sum_{i,j>i}^{N^C}\frac{q_i q_j}{\mathbf{r}_{ij}}, \end{aligned} \tag{2-3}$$

where, N^α corresponds to the number of particles of species α, and the potential energy operator for quantum species has been split in two components; a intra-species and a inter-species or coupling interaction. Using general rules for matrix elements,[34] the total energy is expressed in terms of one or two-body integrals, as ($i^\alpha \equiv \psi_i^\alpha(\mathbf{r})$)

$$E_0 = \sum_\alpha^{N^Q} \left[\sum_{i=1}^{N^\alpha} \langle i^\alpha | h^\alpha | i^\alpha \rangle + \frac{1}{2} q_\alpha^2 \sum_i^{N^\alpha} \sum_j^{N^\alpha} \langle i^\alpha j^\alpha \parallel i^\alpha j^\alpha \rangle + \sum_{\beta>\alpha}^{N^Q} q_\alpha q_\beta \sum_i^{N^\alpha} \sum_j^{N^\beta} \langle i^\alpha j^\beta | i^\alpha j^\beta \rangle \right] + \sum_{i,j>i}^{N^C} \frac{q_i q_j}{r_{ij}}, \quad (2\text{-}4)$$

with one-particle operator $h^\alpha(\mathbf{r})$

$$h^\alpha = -\frac{\nabla^2}{2M_\alpha} + \sum_i^{N^C} \frac{q_\alpha q_j}{|\mathbf{r} - \mathbf{R}_i|}. \quad (2\text{-}5)$$

The Hartree-Fock (HF) equation for each particle of species α, is given by

$$f^\alpha \psi_i^\alpha = \varepsilon_i^\alpha \psi_i^\alpha, \qquad \forall i \in \alpha, \quad (2\text{-}6)$$

where f^α is an effective Fock operator for quantum species α written as

$$f^\alpha = h^\alpha + q_\alpha^2 \sum_{j\in\alpha} [J^\alpha - K^\alpha] + \sum_{\beta\neq\alpha}^{N^Q} q_\alpha \sum_{j\in\beta} q_\beta J^\beta. \quad (2\text{-}7)$$

The operators J and K, are Coulomb and exchange operators, defined as

$$J^\gamma(1)\psi_i^\alpha(1) = \left[\int d\mathbf{r}_2 \psi_j^{\gamma *}(2) \frac{1}{\mathbf{r}_{12}} \psi_j^\gamma(2) \right] \psi_i^\alpha(1), \qquad \text{for } \gamma = \alpha, \beta, \quad (2\text{-}8)$$

$$K^\alpha(1)\psi_i^\alpha(1) = \left[\int d\mathbf{r}_2 \psi_j^{\alpha *}(2) \frac{1}{\mathbf{r}_{12}} \psi_i^\alpha(2) \right] \psi_j^\alpha(1). \quad (2\text{-}9)$$

Equation (2-7) shows that the effective field experienced by one quantum species depends on the MOs of the remaining species. In the standard MO-LCAO approach, approximate HF orbitals ψ_i^α are constructed as linear combinations of atomic basis functions χ_i^α:

$$\psi_i^\alpha = \sum_j c_{ji} \chi_i^\alpha(\mathbf{r}), \quad (2\text{-}10)$$

the coefficients c_{ji} are obtained from the solution of the Roothaan-Hall equation:

$$F^\alpha C^\alpha = S^\alpha C^\alpha \varepsilon^\alpha, \quad (2\text{-}11)$$

with matrices F^α and S^α defined by

$$F_{ij}^\alpha = \langle \chi_i^\alpha | f^\alpha | \chi_j^\alpha \rangle, \tag{2-12}$$
$$S_{ij}^\alpha = \langle \chi_i^\alpha | \chi_j^\alpha \rangle. \tag{2-13}$$

The expansion coefficients in equation (2-10) are then given by $c_{ji} = C_i$. This reduces the problem to calculating overlap integrals $\langle \chi_i^\alpha | \chi_j^\alpha \rangle$ and matrix elements of F^α in the way of equation (2-4) so that the APMO-HF total energy becomes:

$$E_{APMO-HF} = \sum_\alpha^{N_Q} \sum_{ij}^{N_\chi^\alpha} P_{ji}^\alpha \left(h_{ij}^\alpha + F_{ij}^\alpha \right) + E^{coup}$$

$$E^{coup} = \sum_\alpha^{N_Q} \sum_\beta^{N_Q} \sum_{ij}^{N_\chi^\alpha} \sum_{kl}^{N_\chi^\beta} \left(P_{ji}^\alpha P_{lk}^\beta (\chi_i^\alpha \chi_j^\alpha | \chi_k^\beta \chi_l^\beta) \right), \tag{2-14}$$

where E^{coup} is the coupling energy describing the interaction between particles of different quantum species.

The optimized set of coefficients c_{ji} for all quantum species α is obtained by minimizing equation (2-14) variationally. At each step of the minimization procedure, the calculation of the total APMO-HF energy is preceded by one of the following calculations:

- Full convergence of the self-consistent field (SCF) procedure, equation (2-11), for each quantum species.
- Single-iteration of the SCF for each quantum species.

In either case, convergence is reached when the variation of the total APMO-HF energy is lower than a specified threshold value, usually 10^{-10} Hartree.

2.2. Grid-based Hartree-Fock

2.2.1. Multicenter numerical integration

The linear combination of molecular orbitals (LCAO), along with the dominant use of Gaussian chemical basis sets,[34] have been the primary computational approach for *ab initio* non-solid-state quantum chemical methods. The use of Gaussian-type orbitals (GTO) is motivated by the low computational cost of evaluating the necessary integrals compared to other alternatives such as Slater-type orbitals (STO).

Usually, numerical integration is required when alternative representations to GTO are used in *ab initio* non-solid-state computational implementations. In principle, straightforward

discrete integration in Cartesian coordinates is not recommended for the case of molecular (*i.e.* multicenter) systems since these integrals are dominated by cusps at atomic nuclei.

Several approaches have been proposed to perform multicenter numerical integration for polyatomic molecules. For instance, integration in standard orthogonal curvilinear or prolate spheroidal coordinates for the particular case of two-center systems,[35, 36] cellular partitioning of the molecular space into discrete regions or "cells" with the positions of the nuclei followed by numerical integration within each region,[37] discretization of the molecular space with three-dimensional finite elements,[38] decomposition of the integrands into single-centered (*i.e.* atom-centered) contributions followed by its integration in monocentered grids,[33, 39] among others.

The decomposition of the integrand in single-centered components (DSC) has been widely used in Density Functional Theory (DFT) for the numerical integration of several functionals. As a consequence, many improvements have been performed over DSC in the last decades such as the adaptive grid refinement for efficient integration.[40–45] These improvements makes the DSC a reliable strategy to perform multicenter numerical integration in polyatomic systems.

In the present work, DSC has been chosen as the primary strategy to calculate the required integrals within a basis-set-free multi-component framework. The DSC strategy as it was proposed by Becke [33] is described below.

According to Becke, any multicenter molecular function, $F(\mathbf{r})$, can be decomposed as a sum of single-center components, $F_n(\mathbf{r})$:

$$F(\mathbf{r}) = \sum_n F_n(\mathbf{r}), \tag{2-15}$$

so that the integration of the multicenter molecular function $F(\mathbf{r})$ can be reduced to a sum of single-center integrations in the following manner:

$$\int F(\mathbf{r}) d\mathbf{r} = \sum_n I_n, \tag{2-16}$$

where

$$I_n = \int F_n(\mathbf{r}) d\mathbf{r}. \tag{2-17}$$

The single-center components $F_n(\mathbf{r})$ are calculated by multiplying the function $F(\mathbf{r})$ with a set of n-centered relative weight functions $w_n(\mathbf{r})$, as follows:

$$F_n(\mathbf{r}) = F(\mathbf{r}) w_n(\mathbf{r}) \tag{2-18}$$

Each $w_n(\mathbf{r})$ has unit value on the vicinity of its own center, but vanishes uniformly near to other centers. Figure **2-1** illustrates the behavior of the relative weight function $w_n(\mathbf{r})$.

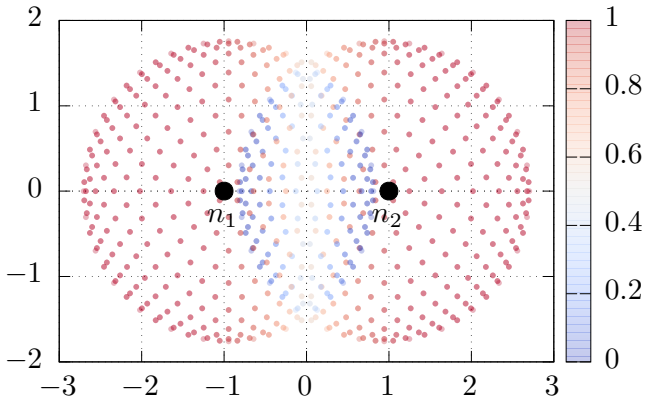

Figure **2-1**.: Two overlapped spherical grids with centers n_1 and n_2 with their corresponding $w_n(\mathbf{r})$ values (color-bar)

Relative weight function

The relative weight function for the n-th center, in a molecular system with k centers, can be expressed as:

$$w_n(\mathbf{r}) = P_n(\mathbf{r}) / \sum_m^k P_m(\mathbf{r}), \tag{2-19}$$

where $P_n(\mathbf{r})$ corresponds to a "cell function" which has unity value if $\mathbf{r}$ lies inside the cell, and vanishes if $\mathbf{r}$ lies outside. This cell function is defined as

$$P_n(\mathbf{r}) = \prod_{m \neq n}^k s(\mu_{mn}), \tag{2-20}$$

with a cutoff function $s(\mu_{mn})$ that depends on the geometrical value μ_{mn}. This hyperboloidal argument μ_{mn}, is calculated as

$$\mu_{mn} = \frac{\mathbf{r}_m - \mathbf{r}_n}{R_{mn}} \tag{2-21}$$

where $\mathbf{r}_m$ and $\mathbf{r}_n$ denote the distances from the point $\mathbf{r}$ to the centers m and n, respectively, and R_{mn} is the inter-center distance. The cutoff function $s(\mu_{mn})$ has been chosen to soften the step discontinuity at $\mu_{mn} = 0$, and to comply with the following requirements:

$$\begin{aligned} s(-1) &= 1, \\ s(+1) &= 0, \end{aligned} \tag{2-22}$$

$$\frac{ds}{d\mu}(-1) = \frac{ds}{d\mu}(+1) = 0. \tag{2-23}$$

The derivative constraints of equation (2-23) ensure that $s(\mu_{mn})$ does not have nuclear cusps. The simplest $s(\mu_{mn})$ satisfying the above constrains is given by

$$s(\mu_{mn}) = \frac{1}{2}\left[1 - f_i(\mu_{mn})\right] \tag{2-24}$$

where the recursive function $f_i(\mu_{mn})$ corresponds to

$$\begin{aligned} f_1(\mu_{mn}) &= p(\mu_{mn}), \\ f_2(\mu_{mn}) &= p[p(\mu_{mn})], \\ f_3(\mu_{mn}) &= p\{p[p(\mu_{mn})]\}, \ldots, \end{aligned} \tag{2-25}$$

with $p(\mu_{mn})$ defined as

$$p(\mu_{mn}) = \frac{3}{2}\mu_{mn} - \frac{1}{2}\mu_{mn}^3. \tag{2-26}$$

Figure **2-2** shows the behavior of the cutoff function at different i. In the present work i has been set to three (*i.e.* $s_3(\mu)$), following Becke's recommendations.

Finally, atomic size adjustments have to be done on coordinate μ_{mn} for heteronuclear systems. This adjustment is made by using the atomic radii reported by Cordero *et al.*[46] Further details can be found in reference [33].

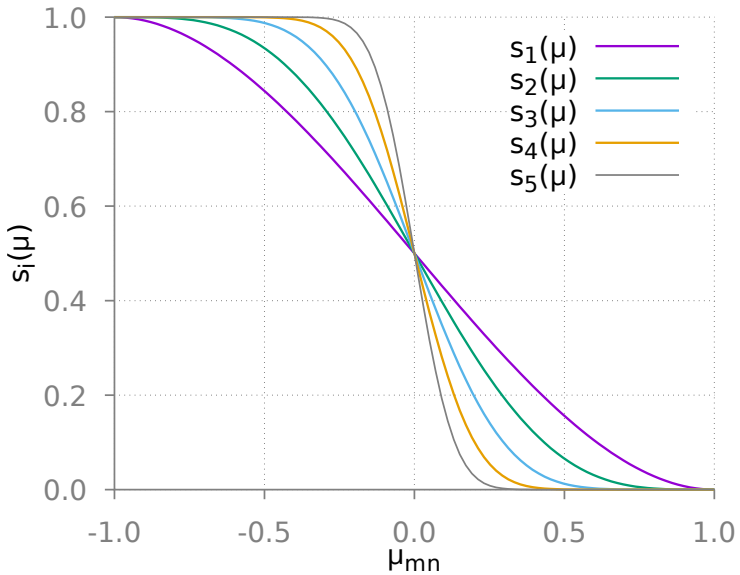

Figure **2-2**.: Cutoff function $s_i(\mu)$, (equation (2-24)) with different i parameter.

Single-center integrations

As shown in equations (2-16) and (2-17), the integration of $F(\mathbf{r})$, can be simplified to the integration of single-center components. Each single-center integral, I_n, is calculated numerically in a spherical coordinate system centered at n, more explicitly

$$I_n = \iiint F_n(r, \vartheta, \varphi) r^2 \sin\vartheta dr d\vartheta d\varphi \tag{2-27}$$

This three-dimensional integral can be calculated using Gauss-type quadratures for two-dimensional integration on the surface of the unit sphere. Therefore, the integral of equation (2-27) can be rewritten as

$$I_n = \iint F_n(r, \Omega) r^2 dr d\Omega \tag{2-28}$$

where Ω denotes the solid angle. The integration over solid angle Ω is carried out using Lebedev grids.[47] A Lebedev grid is characterized by its rank ℓ_{quad} and is designed to integrate spherical harmonics, $Y_{\ell m}$, up to $\ell = \ell_{quad}$.

Finally, radial integration is performed by using Gauss-Chebyshev quadratures of the second kind. Moreover, the standard Gauss-Chebyshev integration interval $-1 < x < +1$, must be mapped into the semi-infinite interval $0 < r < \infty$. This mapping can be achieved through the following coordinate transformation

$$r = r_m \frac{1+x}{1-x} \tag{2-29}$$

where r_m corresponds to the half of the atomic radius for all atoms,[46] except for the hydrogen atom, in which case the factor $1/2$ is not applied. It is important to point out that other numerical quadratures can be used to increase the accuracy of the integration.[40–43]

Results

In order to check the correct implementation of the multicenter molecular integration strategy explained above, we have chosen as a test, the integrand

$$F(\mathbf{r}) = \rho(\mathbf{r}), \tag{2-30}$$

for diatomic systems: H_2, Li_2, Be_2, B_2, C_2, N_2 and O_2, at their equilibrium geometry. For convenience, the total density, $\rho(\mathbf{r})$, has been modeled as the sum of free atomic densities optimized at HF level of theory with LOWDIN quantum chemistry package software,[27] using the 6–31+G** basis-set.[48] Table **2-1** shows the obtained results.

Even though small grids were used in the calculations presented in table **2-1**, our results report an accuracy of 10^{-5}. Moreover, improved accuracies are expected upon enlargement

		Radial Points		
System	Exact	20	25	30
H_2	2.0	1.999 95	1.999 98	2.000 00
Li_2	6.0	6.000 11	5.999 99	6.000 05
Be_2	8.0	7.999 31	7.999 75	8.000 01
B_2	10.0	9.998 13	9.999 67	10.000 02
C_2	12.0	11.998 08	11.999 91	12.000 03
N_2	14.0	13.999 42	14.000 34	14.000 10
O_2	16.0	16.000 07	16.000 07	15.999 91

Table **2-1**.: Numerical integration of $\rho(\mathbf{r})$ for different diatomic molecules. 110 angular points were used in this calculation.

of grid points. In this regard, additional exploration of the accuracy among different grid sizes was performed for O_2 and O systems.

The results of this exploration (figure **2-3**), show that the accuracy not only depends on the number of grid points but also on the number of centers of the system. For instance, in the case of the O atom, the spherical symmetry leads to a fast convergence of the integral value, requiring small angular grids to provide an error of 1×10^{-12}. In contrast, in the case of multicenter systems (with two or more centers), such as the O_2 molecule, spherical symmetry is no longer available, requiring larger angular and radial grids to reach a similar precision.

2.2.2. Poisson's equation for polyatomic molecules

Let us recall Poisson's equation

$$\nabla^2 V(\mathbf{r}) = -4\pi\rho(\mathbf{r}), \tag{2-31}$$

for the potential $V(\mathbf{r})$ of an arbitrary density distribution $\rho(\mathbf{r})$ in a multicenter system. Solving equation (2-31) is equivalent to solving the integral

$$V(\mathbf{r}_2) = \int \frac{\rho(\mathbf{r}_1)}{r_{12}} d\mathbf{r}_1, \tag{2-32}$$

for all points $\mathbf{r}_2$. Combining the solution of Poisson's equation and the multi-center numerical integration explained above, the two-center integrals, *i.e.* the expectation values from equation (2-8)

$$\langle \psi_i^\alpha(\mathbf{r}_1) | J_j^\alpha(\mathbf{r}_1) | \psi_i^\alpha(\mathbf{r}_1) \rangle = \langle ij|ij \rangle = \iint \psi_i^{\alpha *}(\mathbf{r}_1) \psi_j^{\alpha *}(\mathbf{r}_2) \mathbf{r}_{12}^{-1} \psi_i^\alpha(\mathbf{r}_1) \psi_j^\alpha(\mathbf{r}_2) d\mathbf{r}_1 d\mathbf{r}_2, \tag{2-33}$$

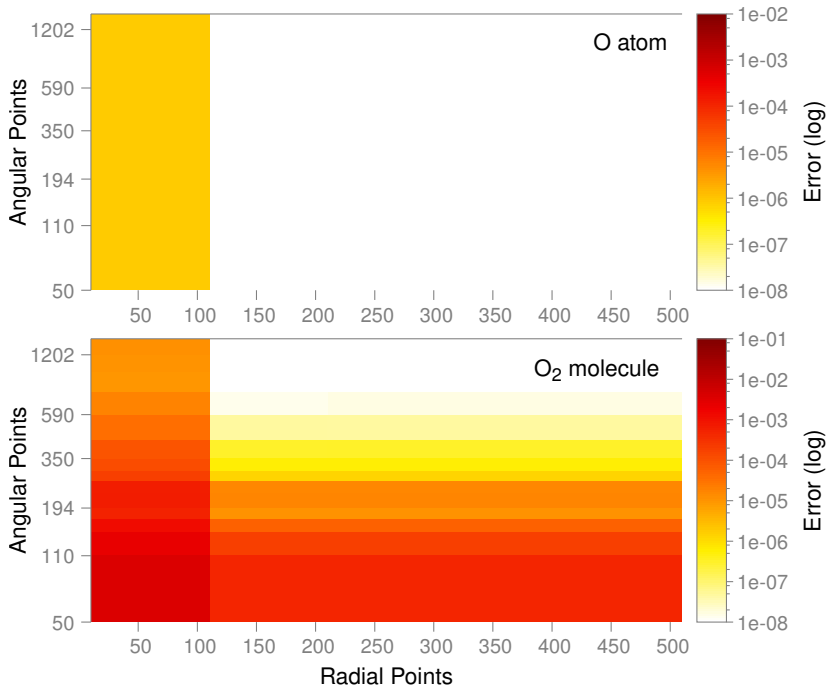

Figure **2-3**.: Averaged error calculating $\int \rho(\mathbf{r})d\mathbf{r}$ for O_2 molecule with different grid sizes. Color in logarithmic scale. 6–31+G** basis-set used.

can be calculated by solving Poisson's equation for potential $V_{ii}(\mathbf{r}_2)$ of charge distribution $\psi_i^\alpha(\mathbf{r}_1)\psi_i^{\alpha*}(\mathbf{r}_1)$ and then evaluating the integral

$$\langle ij|ij\rangle = \int V_{ii}(\mathbf{r}_2)\psi_j^\alpha(\mathbf{r}_2)\psi_j^{\alpha*}(\mathbf{r}_2)d\mathbf{r}_2. \tag{2-34}$$

In order to solve equation (2-31), charge distribution $\rho(\mathbf{r}_1)$, ρ for simplification, has to be decomposed into single-center components as showed in equation (2-18), that is:

$$\rho_n = \rho w_n. \tag{2-35}$$

Each single-center charge distribution leads to a n single-center Poisson's equations of the form

$$\nabla^2 V^{(n)} = -4\pi\rho_n, \tag{2-36}$$

so that the total potential V can be calculated by summing all $V^{(n)}$ potentials. To solve equation (2-36) one can express the single-center charge distribution as a multi-polar expansion [49] of the form

$$\rho_n(r,\vartheta,\varphi) = \sum_{\ell m} \rho_{\ell m}(r)Y_{\ell m}(\vartheta,\varphi), \tag{2-37}$$

where $Y_{\ell m}(\vartheta, \varphi)$ are real spherical harmonics functions, and $\rho_{\ell m}(r)$ are functions of the r variable only. $\rho_{\ell m}(r)$ functions can be calculated through orthogonality of the spherical expansion as follows

$$\rho_{\ell m}(r) = \int_{\Omega} \rho_n(r, \vartheta, \varphi) Y_{\ell m}(\vartheta, \varphi) d\Omega. \tag{2-38}$$

The integrals in equation (2-38), can be calculated using the already mentioned Lebedev quadratures.[47] In principle, the multipolar expansion is infinite; however, the truncation order of the expansion $l_{\max}$ is chosen as half of the order of the Lebedev quadrature l_{quad}

$$l_{\max} = l_{quad}/2. \tag{2-39}$$

Similarly, potential $V^{(n)}$ can be expressed as,

$$V^{(n)}(r, \vartheta, \varphi) = \sum_{\ell m}^{l_{\max}} r^{-1} U_{\ell m}(r) Y_{\ell m}(\vartheta, \varphi). \tag{2-40}$$

Replacing the expansions in equations (2-37) and (2-40), into equation (2-36), and using the following identities:

$$\nabla^2 = \frac{1}{r} \frac{\partial^2}{\partial r^2} r - \frac{L^2}{r^2}, \tag{2-41}$$

with L^2 as the spherical part of the Laplace operator in spherical coordinates, and the eigenvalue equation

$$L^2 Y_{\ell m} = \ell(\ell + 1) Y_{\ell m}, \tag{2-42}$$

we obtain a set of independent radial equations for the functions $U_{\ell m}$:

$$\frac{\partial^2}{\partial r^2} U_{\ell m} - \frac{l(l+1)}{r^2} U_{\ell m} = -4\pi r \rho_{\ell m}. \tag{2-43}$$

The above equations for $U_{\ell m}$ are solved by a finite-difference or finite-elements method in a evenly space mesh. Since Gauss-Chebyshev quadrature is not evenly spaced, the radial grid points have to be mapped into a uniform grid in the space of a new variable z on the interval $0 < z < 1$, defined by

$$x = \cos(\pi z), \tag{2-44}$$

$$z_i = \frac{i}{N+1}, \tag{2-45}$$

where (πz) corresponds to the angular part of the Gauss-Chebyshev quadrature formula for N radial points:

$$x_i = \cos\left(\frac{\pi i}{N+1}\right). \tag{2-46}$$

Combining equations (2-29) and (2-44) and solving for z, we obtain:

$$z = \frac{\arccos\left(\frac{r-r_m}{r+r_m}\right)}{\pi}. \tag{2-47}$$

Using the chain rule we can convert equation (2-43) from the r variable to the z variable, as

$$\frac{\partial^2}{\partial z^2}U_{\ell m}\left(\frac{\partial z}{\partial r}\right)^2 + \frac{\partial}{\partial z}U_{\ell m}\frac{\partial^2 z}{\partial r^2} - \frac{l(l+1)}{r^2}U_{\ell m} = -4\pi r\rho_{\ell m}, \tag{2-48}$$

with r equal to

$$r = r_m\frac{1+\cos(\pi z)}{1-\cos(\pi z)}. \tag{2-49}$$

On the other hand, the boundary conditions are defined in the following way: At $r = \infty$ ($z = 0$) all $U_{\ell m}$ has the value of zero except for U_{00} in which case

$$U_{00}(r \to \infty) = \sqrt{4\pi}q_n, \tag{2-50}$$

where q_n is the total charge of the single-center source density, calculated as:

$$q_n = \int \rho_n(\mathbf{r})d\mathbf{r}, \tag{2-51}$$

and at $r = 0$ ($z = 1$) all $U_{\ell m}$ functions are zero without exception.

Once potential $V^{(n)}$ has been calculated for the grid at center n, it is necessary to calculate the values of $V^{(n)}$ on the grids $m \neq n$. This calculation is done by using cubic spline interpolation. Finally, after solving equation (2-43) for $U_{\ell m}$ equations, the potential $V(\mathbf{r})$ can be reconstructed using equation (2-40).

Results

In order to test our Poisson solver implementation, we have performed the calculation of two-electron Coulomb integrals on H_2 molecule with a minimal STO–3G [50] Gaussian basis set. Our results (presented in table **2-2**) have been compared with analytical results obtained with LIBINT library.[51]

As shown in this table, our results are accurate within to 1×10^{-5} Hartree, for small grids. As in the case of the $\rho(\mathbf{r})$ integrand, the accuracy can be improved by increasing the number of grid points.

Mesh[a]	Coulomb Integral (a.u.)
40 × 50	0.775 61
60 × 110	0.775 06
100 × 146	0.774 77
180 × 170	0.774 65
280 × 194	0.774 62
Exact[b]	0.774 61

[a] Radial × angular points per atom.
[b] Calculated with LIBINT.[51]

Table **2-2**.: Two-electron Coulomb integration over STO–3G basis-set for H_2 molecule.

2.2.3. Grid-based HF solver

The numerical solution of the Schrödinger equation for polyatomic molecules at Hartree-Fock (HF) level of theory was first proposed by Becke *et al.* by combining the already explained multicenter molecular integration strategy and the Poisson equation solver. In such contribution, the exchange operator was not included due to the simplification of the Fock operator for the specific case of the reported H_3^+ molecule. The exchange operator was included in a further contribution as an extension of Becke's methodology under the name of Grid-Based Numerical HF (GBHF).[52] In the present section, we summarize such GBHF methodology.

The one-electron HF equation is given by,

$$\hat{F}(\mathbf{r})\phi_i(\mathbf{r}) = \epsilon_i\phi_i(\mathbf{r}), \tag{2-52}$$

where $\phi_i(\mathbf{r})$ are a set of one-electron wave functions known as HF molecular orbitals. The grid representation of the one-electron Fock operator, $\hat{F}(\mathbf{r})$, is defined as

$$\hat{F}(\mathbf{r}) = \hat{H}^{core}(\mathbf{r}) + \hat{J}(\mathbf{r}) - \hat{K}(\mathbf{r}), \tag{2-53}$$

with one-electron core Hamiltonian $\hat{H}^{core}(\mathbf{r})$

$$-\frac{1}{2}\nabla^2 - \sum_n \frac{Z_n}{|\mathbf{r}-\mathbf{R}_n|}, \tag{2-54}$$

Coulomb operator $\hat{J}$ and finally, exchange operator $\hat{K}$. The solution of equation (2-52) is calculated iteratively by calculating the residual $r_i(\mathbf{r})$

$$r_i(\mathbf{r}) = (\hat{F} - \tilde{e}_i)\tilde{\psi}_i(\mathbf{r}), \tag{2-55}$$

where $\tilde{e}_i$ and $\tilde{\psi}_i(\mathbf{r})$ are approximate orbital energy and orbital wave function. Moreover, the orbital $\tilde{\psi}_i(\mathbf{r})$ is expressed as a linear combination of trial functions $\varphi_i(\mathbf{r})$

$$\tilde{\psi}_i(\mathbf{r}) = \sum_k C_k \varphi_k(\mathbf{r}). \tag{2-56}$$

With each iteration, the linear combination of equation (2-56) increases due to the generation of new trial functions $\varphi_i(\mathbf{r})$, that are calculated in the following manner:

$$\varphi_i^{'}(\mathbf{r}) = \sum_n^{atoms} \left(\hat{F}_{sph}^n - \tilde{e}_i\right)^{-1} w_n(\mathbf{r}) r_i(\mathbf{r}), \tag{2-57}$$

where w_n are the relative weights of the multicenter molecular integration, and $\hat{F}_{sph}^n$, are the spherically averaged single-center contributions of the Fock operator:

$$\hat{F}_{sph}^n = \hat{T} + \hat{V}_{sph}^n + \frac{1}{2}\hat{J}_{sph}^n, \tag{2-58}$$

here $\hat{V}_{sph}^n$ and $\hat{J}_{sph}^n$ are also spherically averaged single-center contributions of the corresponding operators. The inversion of $(\hat{F}_{sph}^n - \tilde{e}_i)$ is straightforward since different angular components do not couple with one another by virtue of the spherical averaging.

It can be readily verified that the trial functions $\varphi_i^{'}(\mathbf{r})$, will tend to zero as the residual decreases. Therefore, convergence is achieved when $|r_i|^2 \leq 10^{-6}$ and the self-consistency is satisfied.

Finally, it is important to point out that the algorithmic details of GBHF methodology, beyond References [1, 33] and [52] have not been reported. As a consequence, the computational implementation and the derivation of all the required equations to perform entirely numerical GBHF and GBHF-APMO calculations were conducted in the present work along the lines of the methodology explained above. These details can be found in chapters 3 and 4.

3. Theoretical development

This chapter addresses the main theoretical contribution of this work, including the extension of the Grid-Based Hartree-Fock (GBHF) methodology to the Any-Particle Molecular Orbital (APMO) formalism. Furthermore, due to the lack of algorithmic details beyond references [33, 49, 52] and [1], our contribution also includes a detailed description of an alternative procedure to perform the GBHF methodology.

In the following, we describe the APMO-GBHF formalism, as well as the formulas required to calculate the Fock operator in grid representation. Additionally, we show the alternative procedure to optimize numerically molecular orbitals within a Numerical Self-Consistent Field (NSCF) scheme.

3.1. Extension of the GBHF formulation for APMO

Let us define the functionals V and W as

$$V[\rho](\mathbf{r}) = \int \frac{1}{|\mathbf{r}-\mathbf{r}'|}\rho(\mathbf{r}')d\mathbf{r}', \tag{3-1}$$

$$\begin{aligned} W[f,g] &= \int f(\mathbf{r})\frac{1}{|\mathbf{r}-\mathbf{r}'|}g(\mathbf{r}')d\mathbf{r}d\mathbf{r}' \\ &= \int f(\mathbf{r})V[g](\mathbf{r})d\mathbf{r}. \end{aligned} \tag{3-2}$$

The functional V is the potential stemming from a density distribution ρ. The total energy at APMO-HF level of theory, equation (2-4), can be written in terms of the functionals V and W as:

$$E_0 = \sum_{\alpha}^{N^Q} E_\alpha + \sum_{I,I>J}^{N^C} \frac{q_I q_J}{|\mathbf{r}_I - \mathbf{r}_J|} \tag{3-3}$$

$$\begin{aligned} E_\alpha = \sum_i \langle \psi_i^\alpha | T^\alpha + V_C^\alpha | \psi_i^\alpha \rangle + \sum_{ij} \left(W\left[(\psi_i^\alpha)^2, (\psi_j^\alpha)^2\right] - \frac{1}{2} W[\psi_i^\alpha \psi_j^\alpha, \psi_i^\alpha \psi_j^\alpha] \right) \\ + \sum_{\beta\neq\alpha}^{N^Q} \sum_{ij} W\left[(\psi_i^\alpha)^2, (\psi_j^\beta)^2\right]. \end{aligned} \tag{3-4}$$

where T^α and V_C^α are the kinetic and point-charges potential energy operators, respectively, and indexes i and j represent occupied orbitals. The HF equations for quantum species α are given by

$$F^\alpha \psi_i^\alpha(\mathbf{r}) = \varepsilon_i^\alpha \psi_i^\alpha(\mathbf{r}), \qquad \forall i \in \alpha. \tag{3-5}$$

Equation (3-5) has been derived by minimizing the energy E_α of the species α with respect to orbital $\psi_i^\alpha(\mathbf{r})$ so that

$$F^\alpha \psi_i^\alpha(\mathbf{r}) = \frac{\partial E_\alpha}{\partial \psi_i^\alpha(\mathbf{r})}. \tag{3-6}$$

The GBHF operator, F^α, operating on an orbital $f(\mathbf{r})$ is defined by

$$\left[F^\alpha f\right](\mathbf{r}) = \left[T^\alpha + V_C^\alpha(\mathbf{r})\right] f(\mathbf{r}) + V_H^\alpha(\mathbf{r}) f(\mathbf{r}) - \left[K^\alpha f\right](\mathbf{r}) + \sum_{\beta \neq \alpha}^{N^Q} V_H^\beta(\mathbf{r}) f(\mathbf{r}), \tag{3-7}$$

where

$$V_H^\gamma(\mathbf{r}) = \sum_i^{\gamma_{occ}} V\left[(\psi_i^\gamma)^2\right](\mathbf{r}), \qquad \text{for } \gamma = \alpha, \beta, \tag{3-8}$$

and the exchange

$$\left[K^\alpha f\right](\mathbf{r}) = \sum_i^{\alpha_{occ}} \psi_i^\alpha(\mathbf{r}) V\left[\psi_i^\alpha f\right](\mathbf{r}). \tag{3-9}$$

The calculation of equation (3-7) will be detailed in the next section. Now, let us suppose that an approximate solution $\phi_i^\alpha(\mathbf{r})$ and an approximate energy e_i^α are available, and that the orbital correction

$$\Delta\phi_i^\alpha(\mathbf{r}) = \psi_i^\alpha(\mathbf{r}) + \phi_i^\alpha(\mathbf{r}), \tag{3-10}$$

for species α, is to be computed instead. The orbital correction $\Delta\phi_i^\alpha(\mathbf{r})$ satisfies the following one-particle *inhomogeneous* Fock-like equations:

$$\left(T^\alpha + V_{APMO}^\alpha(\mathbf{r}) - e_i^\alpha - \Delta e_i^\alpha\right) \Delta\phi_i^\alpha(\mathbf{r}) = \Delta e_i^\alpha \phi_i^\alpha(\mathbf{r}) - R_i^\alpha(\mathbf{r}), \tag{3-11}$$

where $V_{APMO}^\alpha(\mathbf{r})$ is defined as,

$$V_{APMO}^\alpha(\mathbf{r}) = V_C^\alpha(\mathbf{r}) + V_H^\alpha(\mathbf{r}) - K^\alpha(\mathbf{r}) + \sum_{\beta \neq \alpha} V_H^\beta(\mathbf{r}). \tag{3-12}$$

The energy correction, Δe_i^α, is given by

$$\Delta e_i^\alpha = \varepsilon_i^\alpha + e_i^\alpha, \tag{3-13}$$

and the residual $R_i^\alpha(\mathbf{r})$, that measures the quality of the approximate orbital $\phi_i^\alpha(\mathbf{r})$, is defined as

$$R_i^\alpha(\mathbf{r}) = (T^\alpha + V_{APMO}^\alpha(\mathbf{r}) - e_i^\alpha)\,\phi_i^\alpha(\mathbf{r}). \tag{3-14}$$

An approximate solution of equation (3-11) is achieved by generating approximate $\Delta\phi_i^\alpha(\mathbf{r})$ in the following manner: First, we consider Δe_i^α with the first order approximation

$$\Delta e_i^\alpha = \int R_i^\alpha(\mathbf{r})\phi_i^\alpha(\mathbf{r})d\mathbf{r}, \tag{3-15}$$

obtained from equation (3-11) upon multiplication by $\phi_i^\alpha(\mathbf{r})$, integration, and neglect of second-order terms. Then, equation (3-11) is approximately decomposed in single-centered terms in the way of section 2.2.1

$$\Delta\phi_i^\alpha(\mathbf{r}) = \sum_n (\Delta\phi_i^\alpha)^{(n)}(\mathbf{r}). \tag{3-16}$$

leading to single-centered equations ($V_{sph}^{(n)}(\mathbf{r}) \equiv (V_{APMO}^\alpha)_{sph}^{(n)}(\mathbf{r})$):

$$\left(T^\alpha + V_{sph}^{(n)}(\mathbf{r}) - e_i^\alpha - \Delta e_i^\alpha\right)(\Delta\phi_i^\alpha)^{(n)}(\mathbf{r}) = w_n(\mathbf{r})\left(\Delta e_i^\alpha\phi_i^\alpha(\mathbf{r}) - R_i^\alpha(\mathbf{r})\right), \tag{3-17}$$

where $V_{sph}^{(n)}(\mathbf{r})$ is the spherical averaged contribution of the potential energy operator.

$$V_{sph}^{(n)}(\mathbf{r}) = V_C^\alpha(\mathbf{r}) + (V_H^\alpha)_{sph}^{(n)}(\mathbf{r}) + \sum_{\beta\neq\alpha}(V_H^\beta)_{sph}^{(n)}(\mathbf{r}) \tag{3-18}$$

The solution of equation (3-17) is carried out as an extension of the strategy used to solve Poisson's equation. This methodology will be addressed in the next section.

Finally, a new orbital $\psi_i^\alpha(\mathbf{r})$ is calculated as

$$\psi_i^\alpha(\mathbf{r}) = a\phi_i^\alpha(\mathbf{r}) + b\Delta\phi_i^\alpha(\mathbf{r}) \tag{3-19}$$

with variationally optimized coefficients a and b. The calculation of these coefficients will be explained in the last part of the next section. The procedure to perform an overall APMO-GBHF calculation is then illustrated in figure **3-1**.

The red cycle in figure **3-1**, corresponds to the Numerical Self-Consistent Field (NSCF) procedure for a multispecies system. In the following sections, we describe the details on the calculation of the GBHF operator. In addition, we provide some details on the variational minimization of the coefficients a and b in equation (3-19).

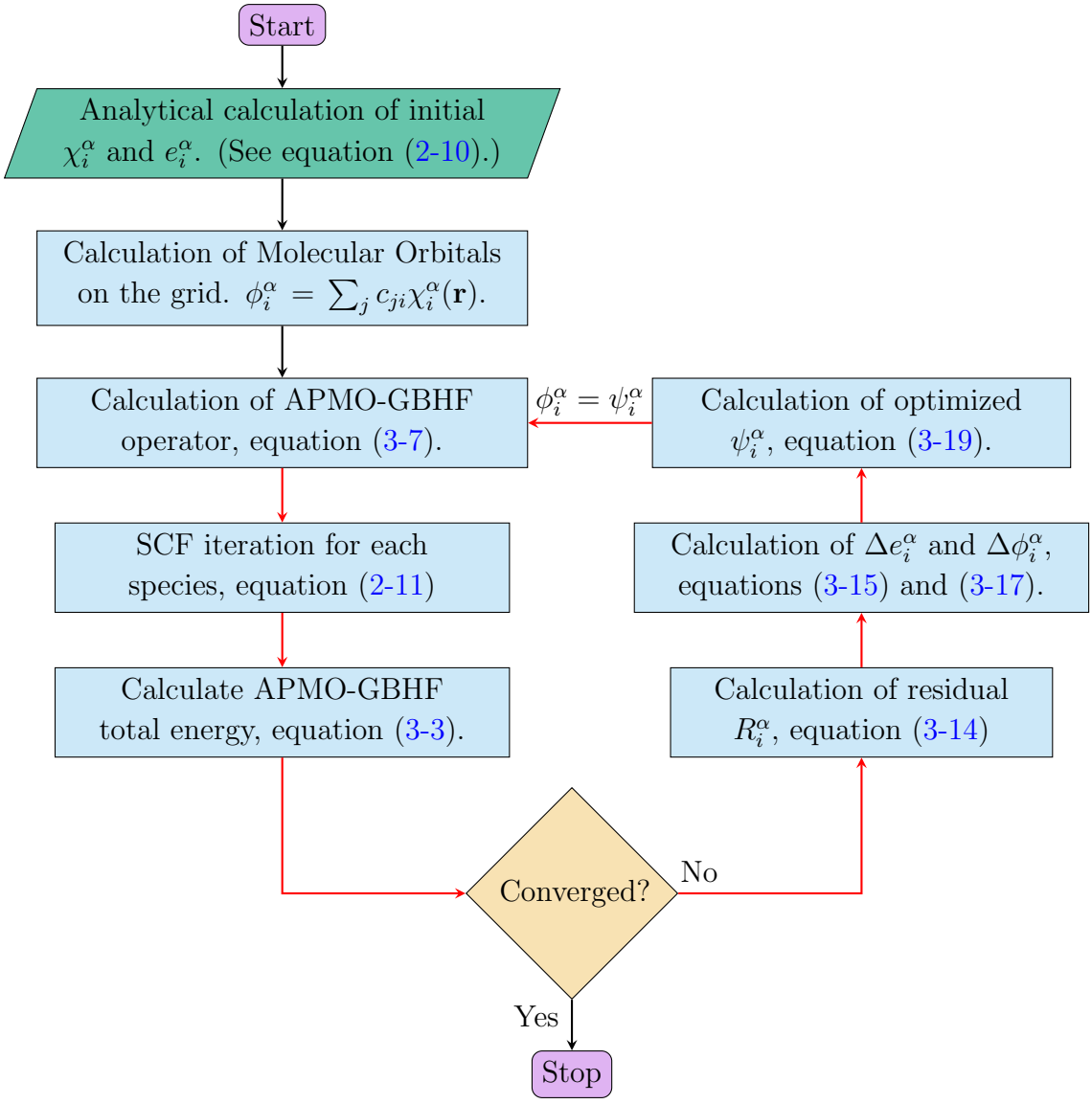

Figure **3-1**.: APMO-GBHF Algorithm.

3.2. Numerical calculation of APMO-GBHF operator

3.2.1. One-particle operator

The one-particle operator h^α (equation (2-5)) is given by

$$h^\alpha = T^\alpha + V_C^\alpha(\mathbf{r}), \tag{3-20}$$

with kinetic energy operator T^α:

$$T^\alpha = \frac{1}{2M_\alpha}\nabla^2, \tag{3-21}$$

and point-charges potential operator $V_C(\mathbf{r})$;

$$V_C^\alpha(\mathbf{r}) = \sum_i^{N^C} \frac{q_\alpha q_i}{|\mathbf{r} - \mathbf{R}_i|}. \tag{3-22}$$

Point charge potential operator

The calculation of the expectation value of $V_C^\alpha(\mathbf{r})$ is straightforward by using the already explained numerical multicenter integration section 2.2.1 in the following way: First, evaluate $V_C^\alpha(\mathbf{r}_i)$ and $\psi_i^\alpha(\mathbf{r}_i)$ at all grid points $\mathbf{r}_i$ to construct a set of $F(\mathbf{r}_i)$ values,

$$F(\mathbf{r}_i) = \psi_i^\alpha(\mathbf{r}_i) V_C^\alpha(\mathbf{r}_i) \psi_i^\alpha(\mathbf{r}_i), \tag{3-23}$$

then, perform numerical integration over the single-center components of $F(\mathbf{r}_i)$,

$$\begin{aligned} F_n(\mathbf{r}_i) &= F(\mathbf{r}_i) w_n(\mathbf{r}_i) \\ \langle \psi_i^\alpha | V_C^\alpha | \psi_i^\alpha \rangle_n &= \sum_i^{npoints} A_i F_n(\mathbf{r}_i) \end{aligned} \tag{3-24}$$

where A_i correspond to the integration weights. Finally, calculate the total integral by summing all single-center contributions as

$$\langle \psi_i^\alpha | V_C^\alpha | \psi_i^\alpha \rangle = \sum_n \langle \psi_i^\alpha | V_C^\alpha | \psi_i^\alpha \rangle_n \tag{3-25}$$

Kinetic energy operator

The expectation value of kinetic energy is calculated from integrals of the form

$$T_{\mu\nu}^\alpha = \int \phi_\mu^\alpha(\mathbf{r}) \left[-\frac{1}{2M_\alpha}\nabla^2 \right] \phi_\nu^\alpha(\mathbf{r}) d\mathbf{r}. \tag{3-26}$$

These integrals are calculated by letting the Laplace operator (∇^2) act on function $\phi_\nu(\mathbf{r})$

$$U(\mathbf{r}) = \nabla^2 \phi_\nu^\alpha(\mathbf{r}) \tag{3-27}$$

so that the integral in equation (3-26) can be calculated as

$$T_{\mu\nu}^\alpha = \int \phi_\mu^\alpha(\mathbf{r}) \left[-\frac{1}{2M_\alpha} U(\mathbf{r}) \right] d\mathbf{r}. \tag{3-28}$$

In order to solve equation (3-27), single-center contributions to function $\phi_\mu^\alpha(\mathbf{r})$ have to be expressed as a multipolar expansion of the form ($\phi_\mu^\alpha(\mathbf{r}) \equiv \phi(\mathbf{r})$)

$$\phi(\mathbf{r}) = \sum_n \phi^{(n)}, (\mathbf{r})$$

$$\phi^{(n)}(r,\theta,\varphi) = \sum_{\ell m}^{\ell_{\max}} \phi_{\ell m}(r) Y_{\ell m}(\theta,\varphi). \tag{3-29}$$

The limit of the expansion $\ell_{\max}$ was already discussed in section 2.2.2. Expanding the $U(\mathbf{r})$ term spherically and using the identities in equations (2-41) and (2-42), we obtain a set of equations that depend solely on the radial coordinate: vx‘

$$U_{\ell m}(r) = \frac{1}{r} \frac{\partial^2}{\partial r^2} r \phi_{\ell m}(r) - \frac{\ell(\ell+1)}{r^2} \phi_{\ell m}(r). \tag{3-30}$$

The second-order derivative in equation (3-30) can be calculated numerically by using any numerical differentiation method. In this work, we have used cubic spline interpolation to map the radial points to an evenly spaced grid, followed by a finite-differences differentiation.

The total $U(\mathbf{r})$ can be constructed from the $U_{\ell m}(r)$ functions as,

$$U(\mathbf{r}) = \sum_{\ell m}^{\ell_{\max}} U_{\ell m}(r) Y_{\ell m}(\theta,\phi) \tag{3-31}$$

where $Y_{\ell m}(\theta,\phi)$ are the spherical harmonics up to $\ell_{\max}$ order, equation (2-39). Finally, the total integral, equation (3-28), can be calculated in the same way of equations (3-24) and (3-25).

3.2.2. Two-particle operators

In APMO-HF approach, there are three different types of two-body integrals; Coulomb, exchange and inter-species or coupling integrals. In this section we will focus on the calculation of exchange and coupling integrals, as the calculation of Coulomb integrals was already explained and illustrated in section 2.2.2.

Exchange operator

The exchange operator, K^α, acting on orbital $\phi^\alpha(\mathbf{r})$ is defined by

$$\left[K^\alpha \phi^\alpha\right](\mathbf{r}) = \sum_i^{\alpha_{occ}} \psi_i^\alpha(\mathbf{r}) V\left[\psi_i^\alpha \phi^\alpha\right](\mathbf{r}), \tag{3-32}$$

using the functional V defined in equation (3-1). Solution of functional $V\left[\psi_i^\alpha \phi^\alpha\right]$ is equivalent to the solution of Poisson's equation for the pseudo pair-density $(\psi_i^\alpha \phi^\alpha)$

$$\nabla^2 V_{i\phi} = -4\pi \psi_i^\alpha(\mathbf{r}) \phi^\alpha(\mathbf{r}). \tag{3-33}$$

The procedure to solve equation (3-33) is explained in section 2.2.2. Matrix elements $K_{\mu\nu}$ of the exchange operator, are then calculated as

$$K_{\mu\nu}^\alpha = \int \phi_\mu^\alpha(\mathbf{r}) \left[K^\alpha \phi_\nu^\alpha\right](\mathbf{r}) \tag{3-34}$$

Coupling operator

The coupling operator $\jmath^\alpha(\mathbf{r})$, for quantum species α, acting on an orbital ϕ^α is defined by

$$\left[\jmath^\alpha \phi^\alpha\right](\mathbf{r}) = \sum_{\beta \neq \alpha}^{N^Q} \phi^\alpha(\mathbf{r}) \sum_i^{\beta_{occ}} V\left[\left(\psi_i^\beta\right)^2\right](\mathbf{r}). \tag{3-35}$$

The functional V for each species $\beta \neq \alpha$ has to be calculated in the points of its own grid, $\mathbf{r}_i^\beta$. The calculation of this functional is done by using the aforementioned solution of Poisson's equation, section 2.2.2, for the pair density $(\psi_i^\beta \psi_i^\beta)$.

As in the previous case, the total integral of the expectation value of coupling operator is calculated as

$$\jmath_{\mu\nu}^\alpha = \int \phi_\mu^\alpha(\mathbf{r}) \left[\jmath^\alpha \phi_\nu^\alpha\right](\mathbf{r}), \tag{3-36}$$

as explained in section 3.2.1.

3.2.3. Grid refinement

As mentioned in section 2.2.1, the radial grid used in the multicenter numerical integration method is the Gauss-Chebyshev quadrature of the second kind. Moreover, this grid is manipulated to map its interval $-1 < x < +1$, into the semi-infinite interval $0 < r < \infty$ through the coordinate transformation of equation (2-29) in which the r_m factor corresponds to the atomic radii.

The lack of an atomic radius for non-electronic species prevents the direct used of the mentioned Gauss-Chebyshev quadrature. However, the r_m factor in equation (2-29) can be calculated for each non-electronic species by minimizing the error in the integration with respect to analytical results. As a consequence, each non-electronic species on a molecular system requires its own integration grid with an optimized r_m factor.

Additionally, the number of the grid points for all species must be the same. The reason for this restriction is the calculation of the coupling operator J_j^β, Equation 2-9, for the Fock operator of species α with $\alpha \neq \beta$.

Furthermore, depending on the quantum nature of each species, the Gauss-Chebyshev quadrature may not be suitable for an accurate integration due to numerical instability. For instance, the μ^- wavefunction is a highly localized function which might generate undesirable oscillations in the edges of the Gauss-Chebyshev nodes. This behavior is known as Runge-Phenomenon.[53]

To overcome this Runge-Phenomenon, we have implemented the alternative radial quadrature:

$$x_i = r_{\text{min}} i^p, \qquad \text{with } i = 1, 2, \ldots, N, \tag{3-37}$$

where N is the total number of quadrature points, r_{min} has to be optimized for each species and $r_{\text{min}} > 0$. Additionally, the power p is calculated from r_{min} in the following manner:

$$p = \frac{\log r_{\text{max}} - \log r_{\text{min}}}{\log N}, \tag{3-38}$$

with parameter r_{max} which has to be provided and therefore optimized for each quantum species. Power p has to be greater than two to get an accurate integration.

Finally, it is important to stress that the parameters r_m, r_{max} and r_{min} will be reported in each result in which non-electronic quantum species are involved.

3.2.4. Results

In order to test our theoretical development to calculate the GBHF operator, we have performed GBHF calculations over electronic and exotic systems and compared the resulting kinetic and potential energies with the corresponding analytical results. The terms numerical and analytical refer to the type of the integration used. It is important to point out that the orbital optimization, presented in figure **3-1**, has not been included in these calculations.

Table **3-1** shows numerical (grid-based) and analytical HF energies for H^-, H_2, N_2 and CO_2. In these calculations, all nuclei were treated as point charges. As can be seen in

Molecule	Grid/Basis set	Energy	Analytic (a.u.)	Numeric (a.u.)	ΔE (a.u.)
H^-	100×110/ aug-cc-pVTZ	T	0.487 550	0.487 551	9.18×10^{-7}
		V_{HF}	−0.975 196	−0.975 192	4.36×10^{-6}
		V_{nuc}	−1.371 605	−1.371 605	1.14×10^{-9}
		V_{e^-}	0.396 409	0.396 413	4.36×10^{-6}
		Total	−0.487 646	−0.487 641	5.27×10^{-6}
H_2	150×590/ cc-pVTZ	T	1.130 418	1.130 418	2.16×10^{-7}
		V_{HF}	−2.263 430	−2.263 428	1.96×10^{-6}
		V_{nuc}	−3.645 217	−3.645 217	8.10×10^{-10}
		V_{e^-}	0.660 838	0.660 840	1.96×10^{-6}
		Total	−1.133 011	−1.133 010	1.74×10^{-6}
N_2	150×590/ cc-pVTZ	T	108.514 114	108.514 099	1.50×10^{-5}
		V_{HF}	−217.487 638	−217.487 571	6.70×10^{-5}
		V_{nuc}	−301.296 768	−301.296 779	1.13×10^{-5}
		V_{e^-}	60.943 448	60.943 526	7.83×10^{-5}
		Total	−108.973 524	−108.973 472	5.20×10^{-5}
CO_2	150×590/ cc-pVTZ	T	187.136 630	187.136 445	1.85×10^{-4}
		V_{HF}	−374.835 606	−374.835 419	1.87×10^{-4}
		V_{nuc}	−556.990 393	−556.990 416	2.35×10^{-5}
		V_{e^-}	125.139 061	125.139 272	2.11×10^{-4}
		Total	−187.698 976	−187.698 973	2.12×10^{-6}

Table **3-1**.: Kinetic (T), potential (V) and total numerical and analytical energies for several systems. (radial × angular) grid sizes.

the table, all total energies are within 10^{-5} Hartree. Moreover, as mentioned before, the accuracy is compromised when the system comprises more than one center as a result of the loss of spherical symmetry. For these multicenter systems we have used more grid points, especially in the angular grid, to increase accuracy.

Additionally, as observed in table **3-1**, the electronic potential energy (V_{e^-}) is the main source of error in the total potential energy (V_{HF}) due to the multicenter nature of the Coulomb operator (*i.e.* it is non-separable on single-center components). Finally, the accuracy of kinetic T energy is affected by the algorithm used to interpolate the orbital $\psi_i^\alpha(\mathbf{r})$ after the first derivative of the Laplace operator has been calculated.

On the other hand, APMO-GBHF calculations, without orbital optimization, have been performed on the exotic systems Heμ and PsH. Muonic Helium (Heμ) is created by using a

System	Grid/Basis	Energy	Analytic (a.u.)	Numeric (a.u.)	ΔE (a.u.)
Heμ	500×110^a/ e^-: aug-cc-pVTZ μ^-: HeMU [25]	T	413.614 015	413.614 015	7.51×10^{-8}
		V_{HF}	−827.543 050	−827.543 050	3.52×10^{-9}
		V_{nuc}	−828.542 526	−828.542 526	5.17×10^{-9}
		V_{coup}	0.999 476	0.999 476	1.66×10^{-9}
		Total	−413.929 035	−413.929 035	7.16×10^{-8}
PsH	100×110^b/ e^-: aug-cc-pVTZ e^+: 7S7P [32]	T	0.666 157	0.666 158	1.22×10^{-6}
		V_{HF}	−1.332 398	−1.332 399	1.21×10^{-6}
		V_{nuc}	−1.213 375	−1.213 375	6.60×10^{-10}
		V_{coup}	−0.585 923	−0.585 928	5.57×10^{-6}
		V_{e^-}	0.466 900	0.466 905	4.36×10^{-6}
		Total	−0.666 241	−0.666 241	1.63×10^{-8}

[a] Radial grid specs: $r_m = 0.585\,804\,700\,851$ for e^+.
[b] Radial grid specs: $r_{\min} = 3.307\,335\,002\,03 \times 10^{-8}$ and $r_{\max} = 16.276\,983\,371\,222$.

Table **3-2**.: Kinetic (T), potential (V) and total numerical and analytical energies for multi-species systems. (radial × angular) grid sizes.

negative muon (μ^-) to replace an electron in the He atom. While the positronium hydride (PsH), comprises one proton, two electrons, and a positron. In both systems, nuclei have been treated as point charges. Results are shown in table **3-2**.

Numerical energies reported in table **3-2** are in good agreement with analytical results. Nevertheless, in contrast to the PsH system, in which a small grid was enough to reach μhartree-order accuracy, the Heμ system has required a different and larger radial quadrature. These grid requirements are related to the nature of the quantum species, for instance, μ^- orbitals are highly localized functions, which might lead to a numerical instability when using Gauss-Chebyshev quadrature for numerical integration.

3.3. Variational optimization for numerical APMO-HF orbitals

In the previous section, we derived the equations and the algorithmic details to calculate the GBHF operator. Additionally, we have shown some results to assess the accuracy of our method. In this section, we show the procedure to optimize the calculated numerical orbitals, starting with the calculation of the orbital correction, followed by the variational minimization of equation (3-19). Finally, we show some results in electronic and multispecies systems.

3.3.1. Calculation of the orbital correction

This section addresses the calculation of orbital correction in equation (3-17). Let us rewrite equation (3-17) as (we omit α and i indexes for simplification):

$$\frac{1}{2M}\nabla^2\left[\Delta\phi^{(n)}\right] + \left(V_{sph}^{(n)} - e - \Delta e\right)\left[\Delta\phi^{(n)}\right] = M^{(n)}, \qquad M^{(n)} = w_n\left(\Delta e\phi - R\right). \tag{3-39}$$

Expanding the single-center orbitals $\Delta\phi^{(n)}$ and $M^{(n)}$ in spherical harmonics basis

$$\Delta\phi^{(n)}(r,\theta,\varphi) = \sum_{\ell m}^{\ell_{\max}} \Delta\phi_{\ell m}^{(n)}(r) Y_{\ell m}(\theta,\varphi), \tag{3-40}$$

$$M^{(n)}(r,\theta,\varphi) = \sum_{\ell m}^{\ell_{\max}} M_{\ell m}^{(n)}(r) Y_{\ell m}(\theta,\varphi), \tag{3-41}$$

where $\ell_{\max}$ is defined in equation (2-39), and using the identities:

$$\nabla^2 = \frac{1}{r}\frac{\partial^2}{\partial r^2}r - \frac{L^2}{r^2}, \tag{3-42}$$

$$L^2 Y_{\ell m} = \ell(\ell+1) Y_{\ell m}, \tag{3-43}$$

already explained in section 2.2.2, we obtain the following set of uncoupled radial equations:

$$\frac{\partial^2}{\partial r^2}\Delta\phi_{\ell m}^{(n)} + \frac{2}{r}\frac{\partial}{\partial r}\Delta\phi_{\ell m}^{(n)} + \left[V_{sph}^{(n)} - e - \Delta e - 2\frac{\ell\left(\ell+1\right)}{2r^2}\right]\Delta\phi_{\ell m}^{(n)} = -2M_{\ell m}^{(n)}. \tag{3-44}$$

The second-order partial differential equation (3-44) is calculated with finite differences and orthogonality of the spherical harmonic functions in equations (3-40) and (3-41) yields to the following expressions for $\Delta\phi_{\ell m}^{(n)}$ and $M_{\ell m}^{(n)}$:

$$\Delta\phi_{\ell m}^{(n)}(r) = \int_\Omega \Delta\phi^{(n)}(r,\theta,\varphi) Y_{\ell m}(\theta,\varphi) d\Omega, \tag{3-45}$$

$$M_{\ell m}^{(n)}(r) = \int_\Omega M^{(n)}(r,\theta,\varphi) Y_{\ell m}(\theta,\varphi) d\Omega. \tag{3-46}$$

Finally, summation of the orbital correction

$$\Delta\phi = \sum_n \Delta\phi^{(n)} \tag{3-47}$$

is preceded by a cubic spline interpolation for the values $\Delta\phi^{(n)}$ in the mesh $m \neq n$.

3.3.2. Calculation of new orbitals

As mentioned before, at each step of the Numerical Self-Consistent Field (NSCF) (see figure **3-1**), a new orbital (ψ_i^α) is calculated by combining the orbital correction $\Delta\phi_i^\alpha$, explained in the previous section, and the orbitals ϕ_i^α in the manner of equation (3-19), that is:

$$\psi_i^\alpha(\mathbf{r}) = a\phi_i^\alpha(\mathbf{r}) + b\Delta\phi_i^\alpha(\mathbf{r}) \tag{3-48}$$

with variationally optimized coefficients a and b. In this section, we explain the strategy employed to optimize such coefficients.

Let us suppose that the coefficients a and b exist and provide the lowest total energy. Consequently, the problem of finding these coefficients can be reduced to the minimization of the energy E_α for species α with respect to the orbitals $\psi_i^\alpha(\mathbf{r})$, that is:

$$\frac{\partial E_\alpha}{\partial \psi_i^\alpha(\mathbf{r})}. \tag{3-49}$$

In order to assure orthogonality in the resulting orbitals $\psi_i^\alpha(\mathbf{r})$, the minimization procedure in equation (3-49) can be performed in the way of equation (3-6) which leads to the HF equations:

$$F^\alpha\psi_i^\alpha(\mathbf{r}) = e_i\psi_i^\alpha(\mathbf{r}), \qquad \text{with } \psi_i^\alpha(\mathbf{r}) = a\phi_i^\alpha(\mathbf{r}) + b\Delta\phi_i^\alpha(\mathbf{r}), \tag{3-50}$$

which can be solved by trivial extension of the SCF procedure, with $[F^\alpha\psi_i^\alpha(\mathbf{r})]$ calculated in the way of section 3.2 and considering equation (3-48) as a linear combination in which a and b are the coefficients to be optimized:

$$\psi_i^\alpha(\mathbf{r}) = a\phi_i^\alpha(\mathbf{r}) + b\Delta\phi_i^\alpha(\mathbf{r}) = \sum_k^2 c_k\phi_{ik}^\alpha(\mathbf{r}). \tag{3-51}$$

3.3.3. Results

In order to assess the proposed methodology to optimize numerical orbitals, we performed GBHF and APMO-GBHF calculations for several electronic and multispecies systems. Additionally, we compared the resulting total energies with the corresponding HF-limit. Furthermore, we illustrated the effect of the orbital optimization by comparing numerical and analytical densities for some these systems.

Atomic systems

Unlike Becke *et al.*[1] and Hirata *et al.*[52], the initial density in our calculations is taken from an analytical calculation with a minimal Gaussian-type orbital (GTO) basis set. (*i.e.* STO-3G). Moreover, in the case of ions, an augmented basis set is used by adding a Pople-style diffuse.[54]

Atoms	HF limit (a.u)	GBHF (a.u.)	Δ E
H	$-0.500\,00^{a}$	$-0.499\,90$	9.96×10^{-5}
H^-	$-0.487\,98^{b}$	$-0.487\,83$	1.67×10^{-4}
He	$-2.861\,68$[55]	$-2.860\,93$	7.47×10^{-4}

[a] Exact value.
[b] Complete basis set (CBS) extrapolation.

Table **3-3**.: HF limit and grid-based HF (GBHF) energies (in atomic units). Grid-based HF calculations employed a 100 × 110 (radial × angular) grid.

System	Grid (radial × angular)	Energy (a.u.)
H^-	50 × 110	$-0.471\,643$
	100 × 110	$-0.487\,831$
	150 × 194	$-0.487\,915$
	200 × 194	$-0.487\,921$
	300 × 434	$-0.487\,926$
	500 × 590	$-0.487\,929$
	HF-limit	$-0.487\,980^{a}$

[a] Complete basis set (CBS) extrapolation.

Table **3-4**.: Grid based HF energies for H^- employing different grid sizes.

As shown in table **3-3**, all our energies (GBHF) for the initial tests, are in agreement within 1.0×10^{-4} Hartree to the corresponding HF-limit energy. All the tests were performed using a grid with 100 radial and 110 angular points.

Improved accuracy is expected upon enlargement of the initial analytical basis set calculation or by increasing the number of grid points. For instance, table **3-4** shows how accuracy of numerical HF energies for H^- is improved with different grid sizes.

As a result of the orbital optimization, it is expected a better description of the atomic orbitals, that is, a better description of the nuclear cusp. This improvement on the cusp can be seen in figure **3-2** where both analytical and numerical electronic density for the He atom have been plotted.

polyatomic test

As mentioned before, spherical symmetry is no longer available in molecular orbitals of polyatomic systems. Therefore, larger grids become necessary to calculate energies within 10^{-5}

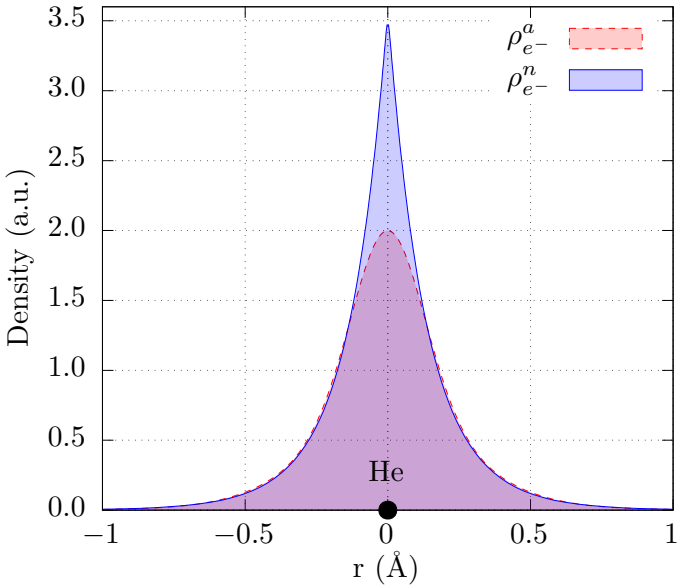

Figure **3-2**.: Numerical ($\rho^n_{e^-}$) and analytical ($\rho^a_{e^-}$) electron densities in He atom. A STO-3G basis was employed in the analytical calculation. The numerical calculation employed a 100×110 (radial $\times$ angular) grid.

Hartree with respect to the HF limit. However, in order to compare the precision of our methodology with the atomic tests, we have used the same number of grid points and the same basis set for the initial guess.

For this case, we have chosen the H_2 and $H_3{}^+$ molecules, table **3-5** shows the numerical HF (GBHF) energies compared with the HF limit. As expected, ΔE increases with the number of centers in the molecule. Desired precision can be reached by increasing the number of grid points. For instance, the total energy for the $H_3{}^+$ molecule calculated with a grid of 100×590 (radial $\times$ angular) is within 10^{-4} Hartree with respect to the HF limit, as can be seen in table **3-5**).

Similar to the atomic case, the optimization of the orbitals leads to a better description of the nuclear cusp. Figure **3-3** shows the density charge distribution for the H_2 molecule.

Multispecies test

The first multispecies test was performed on the Heμ system (see section 3.2.4). Several theoretical [25, 57–59] and experimental [57] studies has been performed for this system. For instance, it has been shown that Heμ behaves as a heavy isotope of hydrogen because the muon screens almost perfectly one positive charge in the He nucleus. However, besides this

Molecule	GBHF (a.u.)	HF limit(a.u.)	ΔE
H_2	$-1.133\,51^a$	$-1.133\,63$[56]	1.21×10^{-4}
$H_3{}^+$	$-1.295\,14^a$	$-1.300\,41$[1]	5.27×10^{-3}
$H_3{}^+$	$-1.300\,23^b$		1.72×10^{-4}

[a] 100×110 (radial × angular) grid points.
[b] 100×590 (radial × angular) grid points.

Table **3-5**.: Numerical HF (GBHF) and HF limit energies for H_2 and $H_3{}^+$. Energies is a.u.

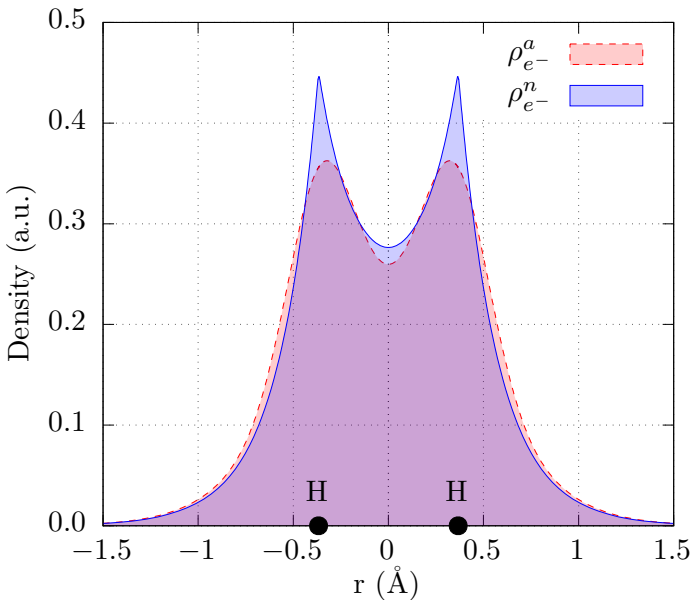

Figure **3-3**.: Numerical ($\rho^n_{e^-}$) and analytical ($\rho^a_{e^-}$) electron densities for H_2 molecule. A STO-3G basis was employed in the analytical calculation. The numerical calculation employed a 100×110 (radial × angular) grid.

System	Basis set[a]	Energy (a.u.)
Heμ	aug-cc-pVDZ:13s	−413.926 32
	aug-cc-pVTZ:13s	−413.929 04
	aug-cc-pVQZ:13s	−413.929 39
	aug-cc-pV5Z:13s	−413.929 45
	This work	−414.034 76
	Frolov [57]	−414.036 54

[a] Electronic:muonic basis set.[58]

Table **3-6**.: APMO-HF, APMO-GBHF (this work) and ground state (Frolov) energies for the Heμ system. APMO-GBHF energy calculated with a 500 × 110 (radial × angular) grid. Basis-set for the initial density in APMO-GBHF calculation: aug-cc-pVTZ:13s (e^-:μ) . Radial grid parameters: $r_{\min} = 3.307\,335\,002\,03 \times 10^{-8}$ and $r_{\max} = 16.276\,983\,371\,222$

mass effect, a small, but significant quantum muon effect has been quantified using APMO theory [58] (see Appendix C).

The ground state energy of the Heμ was reported by Frolov *et al.*[57] using high-precision variational calculations which can be considered as the HF limit since the μ-e$^-$ correlation is negligible [58]. The energy obtained with our methodology, agrees within 10×10^{-3} Hartree with Frolov's result (table **3-6**). In addition, it can be seen that our APMO-GBHF performs better than any other considered electronic basis set.

With the aim of testing applicability of our methodology with different quantum species, we have also performed APMO-GBHF calculations on positronium hydride (PsH). For this system, we have used as guess the electronic aug-cc-pVDZ, and the positronic 7s7p [31, 32] basis sets. Results of our calculations are compiled in table **3-7**.

Similarly to the Heμ system, our methodology performs better than the analytical basis sets and is in agreement within four digits with the complete basis set extrapolation (CBS). Additionally, since the positron has the same mass of an electron but with opposite charge, we expect an inverted nuclear cusp. Figure **3-4** shows the expected behavior in the numerical positron density and the difference with the analytical result.

System	Basis set	Energy (a.u.)
PsH	aug-cc-pVDZ:7s7p	−0.664 953
	aug-cc-pVTZ:7s7p	−0.666 484
	aug-cc-pVQZ:7s7p	−0.666 821
	aug-cc-pV5Z:7s7p	−0.666 924
	This work	−0.666 935
	APMO-HF$_{CBS}$	−0.667 085

Table **3-7**.: APMO-HF, APMO-GBHF (this work) and APMO-HF complete basis-set extrapolation (APMO-HF$_{CBS}$) energies for PsH system. APMO-GBHF calculated with a 100×110 (radial × angular) grid. Basis-set for the initial density in APMO-GBHF calculation: aug-cc-pVDZ:7s7p (e^-:e^+). Radial grid parameters: $r_m = 0.585\,815\,101\,516$.

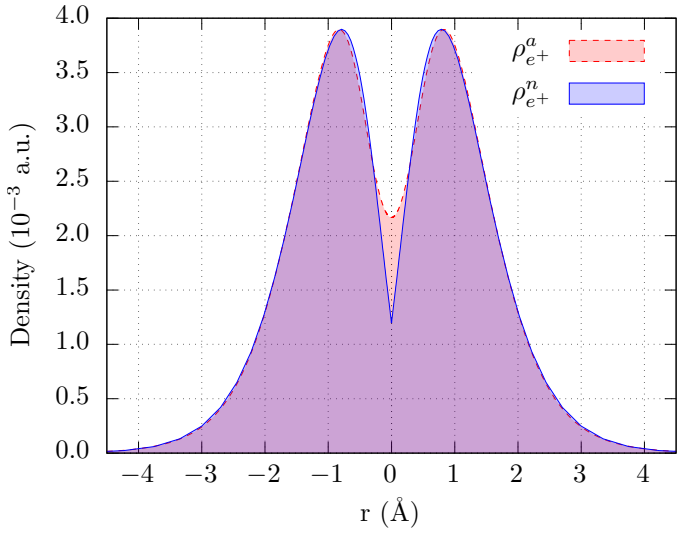

Figure **3-4**.: Numerical ($\rho^n_{e^+}$) and analytical ($\rho^a_{e^+}$) positron (e^+) densities in PsH. An aug-cc-pVDZ:7s7p (electronic:positronic) basis-set was used in the analytical calculation. The numerical calculation employed a 100×110 (radial × angular) grid.

4. Computational implementation

The computational implementation of the theoretical development explained in chapter 3 is called Nu-APMO (numerical Any Particle Molecular Orbital). In the present chapter, we describe the technical details behind Nu-APMO.

The source code of Nu-APMO was written in Python and C/C++ languages. The use of Python permits faster development as well as offering different tools for the visualization of the results and code customization. In contrast to compiled languages, pure Python code has poor performance for numerical calculations. As a consequence, the numerical part of the program has been coded in C/C++. An additional advantage of using C/C++ over Python for numerical programming is the possibility of employing practically any parallelization framework.

The overall code was written from scratch. The lastest version of Nu-APMO contains more than 19.000 lines of code. The following is the outcome of the Linux command *cloc*:

```
github.com/AlDanial/cloc v 1.72
-------------------------------------------
Language      files  blank  comment    code
-------------------------------------------
C++              23   1569     1541    9276
JSON              4      0        0    5354
Python           55   1775     2301    3398
C/C++ Header     26    564      718    1286
CUDA              4     83       58     288
make              6     56       39     199
YAML              1      0        2      58
-------------------------------------------
SUM:            119   4047     4659   19859
-------------------------------------------
```

The code can be compiled using the standard *make* command in three different ways; SERIAL, OMP (OpenMP), and CUDA. Table 4-1 summarizes the prerequisites to compile and run Nu-APMO.

Requisites	SERIAL	OMP	CUDA
C/C++ compiler (GCC, INTEL)	√	√	√
SciPy	√	√	√
libGSL	√	√	√
libCBLAS	√	√	√
OpenMP		√	√
CUDA ToolKit			√

Table **4-1**.: Requisites to compile and run Nu-APMO

The parallelized versions of the code (OMP and CUDA) are generated automatically in compilation-time. The use of this versions is entirely transparent from the user perspective (*i.e.* no additional requirements are needed). Now, we will discuss the structure of the program.

4.1. Program structure

The program is divided into two main parts; the C library called *libnapmo* and the Python interface *napmo*. Figure 4-1 shows the file-system structure of the package.

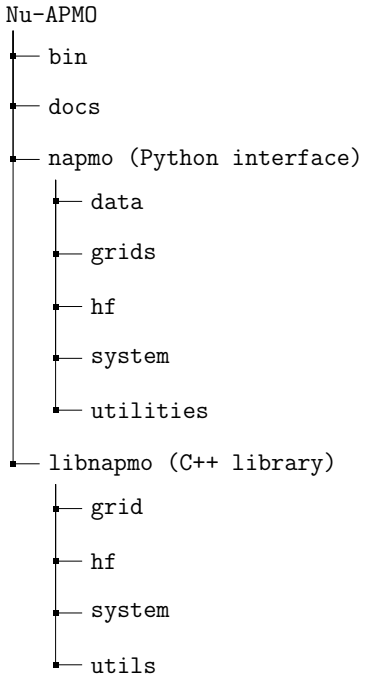

Figure **4-1**.: Structure of Nu-APMO package

4.1.1. Python interface

Python interface consists of five modules, *system*, *grids*, *hf*, *data* and *utilities*. The *system* module manages the molecular system interface. For instance, the code inlisting **4-1** creates a `MolecularSystem` object for the H_2 molecule.

```
from napmo.system.molecular_system import MolecularSystem

molecule = MolecularSystem ()
molecule.add_atom ('H', [0.0, 0.0,0.371])
molecule.add_atom ('H', [0.0, 0.0,0.371])

==================================================
Object: MolecularSystem
--------------------------------------------------
AtomicElement:  atoms  number of e-:  2
Symbol  Z     origin (Bohr)              Basis set
H       1     [ 0.    0.    0.69919862]    --
H       1     [ 0.    0.   -0.69919862]    --
--------------------------------------------------
```

Listing **4-1**: Use of the `MolecularSystem` class from `system` module.

The *data* module handles all the information related to atomic elements constants, elementary particles, and fundamental constants. It also contains some basis sets. Additional basis sets and supplementary information can be added using *json* format.

The module *grids* contains the implementation of Gauss-Chebyshev and Lebedev quadrature. Moreover, this module includes different levels of abstraction for grids such as '`atomic`' for the case of atomic grids and '`becke`' for molecules. Also, the *grids* module contains the Poisson's solver, which is used to calculate Coulomb potentials. As an example, the code in listing **4-2** is used to create the grid represented in figure **2-1**. Once created, the *grid* object contains all the data required to perform numerical integration or to solve Poisson's equation for a given function.

Finally, the *hf* module contains the classes and methods required to perform numerical and analytical calculations at HF level of theory, for either regular or multispecies molecular systems. For instance, *hf* module contains the one-body and two-body integrals, the calculation of the Fock operator in matrix and grid representation, and the implementation of the Self-Consistent Field (SCF) algorithm.

```
from napmo.grids.becke import BeckeGrid

angularPoints = 590
radialPoints = 2
grid = BeckeGrid(molecule.get('e-'), radialPoints, angularPoints)
```

Listing **4-2**: Use of the `BeckeGrid` class from `grids` module to create a grid object.

4.1.2. C++ library

As previously mentioned, C++ language has been chosen to implement numerical routines due to its performance compared with Python language, and because C++ is supported by almost any parallelization framework. The interface between Python and C++ have been done by using the `ctypes` library. Here we provide some details on this interface.

```
import napmo

class AtomicGrid(object):
    ...
    def __init__(self, nrad, nang, origin, atomic_symbol...):
        super(AtomicGrid, self).__init__()
        ...
        self._this = napmo.cext.AtomicGrid_new(
            self.angular_grid._this, self.radial_grid._this, origin)

    def integrate(self, *args, **kwargs):
        ...
        ptr = napmo.cext.AtomicGrid_integrate(
            self._this, nfunc, nseg, sseg, f)
        ...
```

Listing **4-3**: Example from external file

Since ctypes library does not provide a standard support for C++ objects, the interface is mainly based on pointer management. For instance, when a C++ object is created in Python, its corresponding pointer is stored as a `c_void_p` variable inside of a class. In this way, the C++ pointer can be used within the class by any other method.

For instance, in listing **4-3** the function `napmo.cext.AtomicGrid_new` in the `__init__` method of the class `AtomicGrid`, creates a C++ object and store its pointer in the `self._this`

variable. Since the variable `_this` is a member of the class `AtomicGrid`, the pointer can be used in any other method, for example, in the method `integrate` when the function `napmo.cext.AtomicGrid_integrate` is invoked. Note that C++ objects are not used directly, but passed as arguments to a C function where the required methods are called.

On the other hand, the memory allocation is done using the standard procedure for C++ language. When it is needed, the data stored on the C++ memory can be accessed from Python by combining the Python decorator `@property` and the libraries ctypes and *numpy*.[60] An example of this can be found in listing **4-4**.

```
import napmo

class RadialGrid(object):
    ...
    @property
    def points(self):
        ptr = napmo.cext.RadialGrid_get_points(self._this)
        return np.ctypeslib.as_array(ptr, shape=(self.size,))
```

Listing **4-4**: Use of C++ allocated memory in Python

The strategy of memory allocation mentioned above allows for accessing the data as numpy arrays, this is fundamental for taking advantage of the *SciPy* library [61] or visualization tools such as *Matplotlib*.[62]

```
from napmo.system.cext import napmo_library as cext

# Python Function prototype:
cext.RadialGrid_integrate.restype = c_double
cext.RadialGrid_integrate.argtypes = [c_void_p, c_int, a1df]
```

Listing **4-5**: Import of libnapmo library and propotype of C++ functions in Python interface.

Finally, new functions can be added to the C++ library and are available on Python interface by adding a Python function prototype for each new C++ function in the manner of listing **4-5** for the case of the C++ function of listing **4-6**.

Additional details on the application programming interface (API) can be found in reference.[63]

```
// C++ Prototype:
double RadialGrid_integrate(RadialGrid *grid, int segments, double *f);
```

Listing **4-6**: Loading libnapmo functions on Python.

4.2. Performance and parallelization

So far, we have discussed the theory behind Nu-APMO, and the philosophy used to implement the code. In this section, we will discuss the strategy adopted to achieve an optimal parallelization with OpenMP (OMP) and CUDA.

Let us first describe the configuration used to perform all the calculations and benchmarks.

4.2.1. Testing configuration and environment

All test were performed in the Ulysses-SISSA Cluster (Intel Xeon E5−2680 V2 2.80 GHz Ivy Bridge processor 10 Cores 20 Threads) from the International Centre for Theoretical Physics (ICTP) and the International School for Advanced Studies (SISSA) in Trieste, Italy. The CUDA benchmarks were carried out on a NVIDIA GeForce GTX 860M Maxwell card with compute capability 5.0 (5 Multiprocessors, 128 CUDA Cores/MP), and on a NVIDIA Tesla K20m card with compute capability 3.5 (13 Multiprocessors, 192 CUDA Cores/MP).

The C++ library can be compiled with any C++ compiler, GNU GCC compilers from version 4.4.7 to 6.0 and Intel compiler version 16.0.1 were tested. Moreover, the results reported in this work correspond to the binary compiled with GCC 4.4.7 compiler with the following flags:

- `--O2` level of optimization.
- `--fPIC` to produce position-independent code.
- `--ffast-math`.
- `--fompenmp` for OpenMP support..
- `--shared` for the linking process to generate the shared library.

On the other hand, the CUDA version of the libnapmo library was compiled with NVCC compiler version 7.5 with the same flags used with GCC compiler and the following additional flags:

- `-arch=sm_50` for Maxwell card
- `-arch=sm_35` for Tesla card

4.2.2. Multicenter integrator

In this section, we will analyze the performance of the multi-center numerical integrator and its subsequent parallelization with OpenMP and CUDA. To start this analysis, let us first describe the general algorithm adopted to perform the multicenter integration illustrated in figure **4-2**.

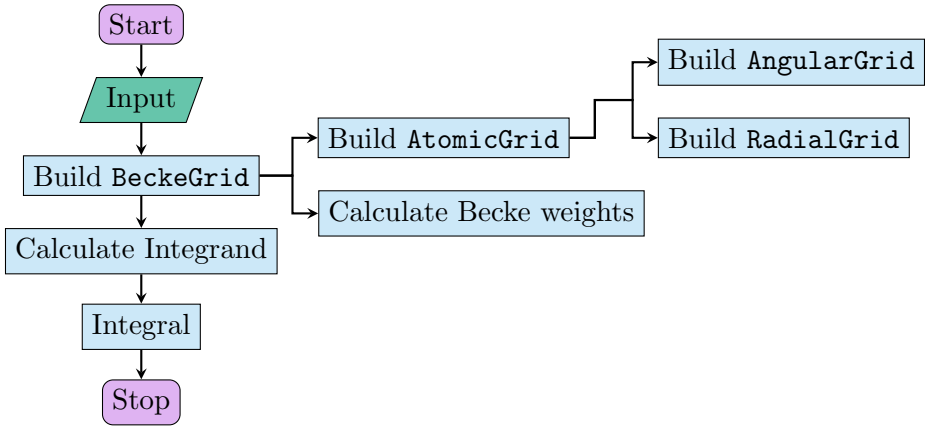

Figure **4-2**.: Algorithm to perform multi-center numerical integration

In principle, the integration process is composed of three main steps; construction of the molecular grid (`BeckeGrid`), calculation of the function $F(\mathbf{r})$ at all points of the grid, and finally, calculation of the integral. To identify suitable spots for parallelization in this algorithm, let us start with the analysis of the serial version of the code.

Serial performance

For this analysis, we have chosen the integration of $\rho(\mathbf{r})$ for the diatomic molecule H_2 with a 6–31+G** basis set. The size of the grid is 1202 angular $\times$ 1000 radial points. The profiling of this integration:

```
85036 function calls (82212 primitive calls) in 2.575 sec

Ordered by: internal time
ncalls  tottime  cumtime  filename:lineno(function)
    1    1.986    1.987   density.py:31(density_full_...)
    1    0.155    0.155   becke.py:85(_becke_weights)
    1    0.124    0.356   becke.py:41(__init__)
    2    0.074    0.078   atomic.py:29(__init__)
    2    0.057    0.119   atomic.py:89(integrate)
```

where `tottime` is the time spent by a function excluding the time spent by its sub-functions (*i.e.* functions called by the function) and `cumtime` is the cumulative time spent by a

function including the time spent in sub-functions overall the program execution. As can be seen in the profiling, the most time-consuming step is the calculation of the integrand in all points of the grid, which for this test is `density.py`, followed by the calculation of Becke weights in the construction of the molecular grids. Consequently, the most obvious target for parallelization is the calculation of the integrand $\rho(\mathbf{r})$, besides the construction of the grids and the calculation of Becke weights.

OpenMP implementation

Once delimited the scope of the parallelization, here we give some details on the implementation of the OpenMP parallelization and its results.

Grids construction As observed in figure 4-2, the algorithm used to construct molecular grids, includes the construction of `AngularGrid` and `RadialGrid` objects to create the `AtomicGrid` instance. The pseudo code to build an `AtomicGrid` object can be found in listing 4-7.

```
loop from i = 0 to AngularGrid.npoints
    loop from j = 0 to RadialGrid.npoints
        // each grid coordinate is:
        AngularGrid.point[i]  * RadialGrid.point[j] + atomic origin
        // each grid point weight is:
        AngularGrid.weight[i] * RadialGrid.weight[j]
```

Listing **4-7**: Pseudo code of the algorithm used in `AtomicGrid` construction.

Therefore, the OpenMP directive `#pragma omp parallel for` can be added to the outer loop corresponding to the number of angular points, which is typically greater than the number of radial points in most of the cases. The addition of the OpenMP directive is illustrated in listing 4-8.

The calculation of Gauss-Chebyshev points (`RadialGrid`) has been parallelized in a similar way, over the number of radial points, as well as the Lebedev grid (`AngularGrid`) over the number of angular points.

Becke weights The calculation of Becke weights is expensive since all centers in the system must be taken into account for each grid point. Figure 4-3 offers a graphical description of the geometry used to calculate the weights. In this figure A and B are centers (*i.e.* atoms) and i corresponds to the ith grid point. Moreover, r_{iA} and r_{iB} are the distances from i to the centers A and B and r_{AB} is the inter-nuclear distance.

```
#pragma omp parallel for default(shared) private(i, j, ...)
loop from i = 0 to AngularGrid.npoints
    loop from j = 0 to RadialGrid.npoints
        // each grid coordinate is:
        AngularGrid.point[i]  * RadialGrid.point[j] + atomic origin
        // each grid point weight is:
        AngularGrid.weight[i] * RadialGrid.weight[j]
```

Listing **4-8**: Parallelized `AtomicGrid` construction (pseudo code).

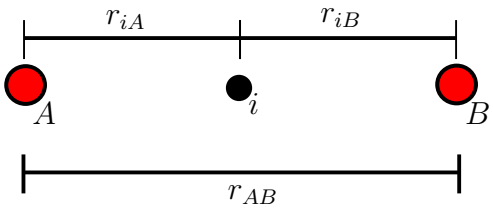

Figure **4-3**.: Geometrical description for Becke-weight calculation of point i in a system with centers A and B

The quantities r_{iA}, r_{iB} and r_{AB} are used to calculate the coordinate μ_{AB} (see section 2.2.1) in the following manner:

$$\mu_{AB} = \frac{r_{iA} - r_{iB}}{r_{AB}} \tag{4-1}$$

This coordinate is then passed to the `step function`, figure **2-2**. More detailed description of the form of the `step function` can be found in chapter 2. The algorithm used to calculate these μ_{AB} coordinates, and in consequence the Becke weights, is shown in listing **4-9**.

As can be seen in the pseudo code, listing **4-9**, three of the four loops in the calculation of Becke weights are over the number of centers (atoms) in the system, while the remaining loop is placed over the number of grid points. Regardless of system size (*i.e.* the number of centers in the molecular system), the number of grid points is always greater than the number of centers. Thus, the OpenMP parallelization is done along the number of grid points as shown in listing **4-10**.

Calculation of the Integrand In principle, the parallelization strategy for the integral calculation should be independent of the integrand. For this reason, the problem has been reduced to the calculation of an arbitrary function in the grid points. Such as in the previous

```
// Calculate internuclear distances
for i = 0 to number of atoms
    for j = 0 to i - 1
        R_ij[counter] = atomic origin[i] - atomic origin[j]

// Calculate the Becke weights
for atom = 0 to number of atoms
    for point = 0 to number of grid points (npoints)
        for i = 0 to number of atoms
            for j = 0 to number of atoms
                if i == j: continue
                r_i = distance point - i
                r_j = distance point - j
                calculate mu_ij
                calculate s = s(mu_ij) //step function
                cell_function *= s
            sum += cell_function
            if iatom == atom: P = cell_function
        weight[atom * npoints + point] = P / sum
```

Listing **4-9**: Becke weights calculation (pseudo code).

case of Becke weights calculation, the parallelization is done along the number of grid points.

It is important to point out that to calculate integrals efficiently with this implementation any new integrand must be implemented and parallelized. Details on the implementation of new functions inside the Nu-APMO package can be found in section 4.1.

OpenMP performance

Here, we show the performance of the OpenMP parallelization described above. For this analysis, we have chosen the integrand $\rho(\mathbf{r})$ for the diatomic molecule of O_2. To explore the scaling among different grid sizes four different grids have been chosen, figure **4-4** shows the calculations time and speedup against the number of threads.

According to figure **4-4**, the biggest grid scales linearly up to 20 threads. In contrast, the remaining grids scale linearly up to 8 threads and four threads for the case of the smallest one. The reason for this behavior is related to the ratio between the serial and parallel code and its dependence on the grid size. Table **4-2** shows the OpenMP analysis performed with Intel VTune amplifier [64] for different grid sizes. As can be seen in the table, the serial part

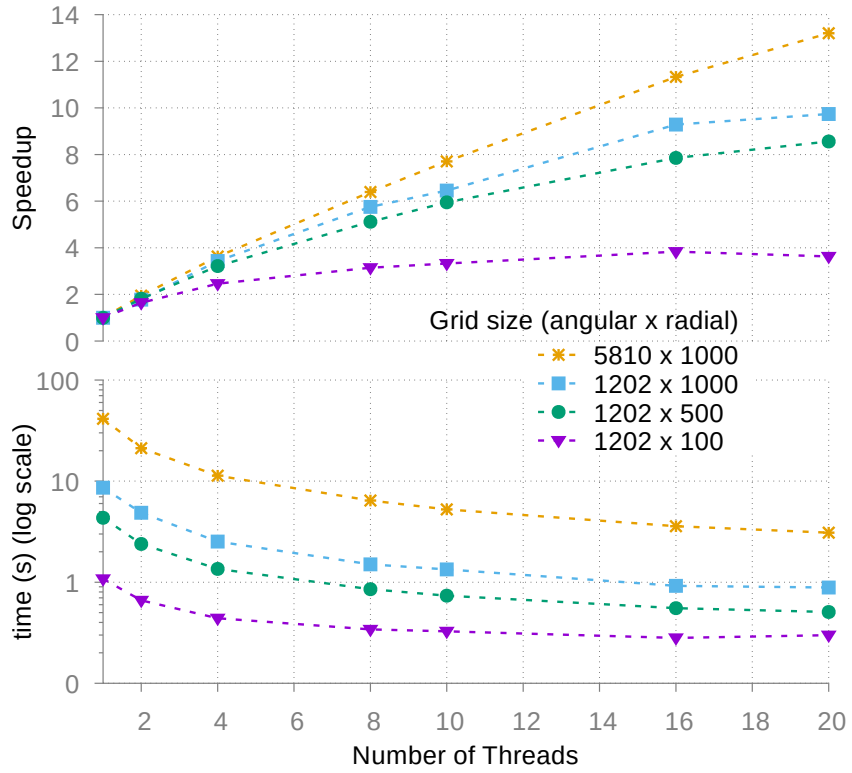

Figure **4-4**.: Time and speedup versus number of threads for the integration of $\rho(\mathbf{r})$ for the O_2 molecule using different grid sizes. Basis set used 6–31+G**.

of the code becomes more relevant for small grid sizes, affecting the expected speedup. The theoretical speedup S has been calculated using the Amdahl's Law [65]

$$S = \frac{1}{r_s + \frac{r_p}{n}} \tag{4-2}$$

where $r_s + r_p = 1$ and r_s and r_p represents the ratio of the serial and parallel portion in one program executed over n threads.

```
...
// Calculate the Becke weights
for atom = 0 to number of atoms
    #pragma omp parallel for default(shared)                \
    firstprivate(atom, npoints, idx) private(point, i, j, \
    r_i, r_j, mu_ij, s, cell_function, sum, P)
    for point = 0 to number of grid points (npoints)
       ...
```

Listing **4-10**: Becke weights calculation parallelized with OpenMP (pseudo code).

In the case of grids a and b the speedup is affected by caching effects, clearly explaining why the actual speedup is higher than the theoretical one.

	Grid Size			
OpenMP analysis	a	b	c	d
Serial Time (%)	69.2	35.9	23.5	13.0
Parallel Region Time (%)	30.8	64.1	76.5	87.0
Theoretical speedup	1.37	2.28	3.02	4.19
Achieved speedup	1.77	2.66	2.90	3.47

Table **4-2**.: Intel VTune amplifier OpenMP (8 threads) analysis for the integration of $\rho(\mathbf{r})$ molecule O_2. 6−31+G** basis set. Grid sizes (angular × radial points): a. 1202×100, b. 1202×500, c. 1202×1000 and d. 5810×1000.

CUDA implementation

Following the profiling of the serial code (see section 4.2.3), the parallelization with CUDA has been implemented over the calculation of Becke weights, the calculation of the integrand and the multicenter integration.

Since memory management is critical in CUDA programming model,[66] the required data structure to get the maximum performance has to be different to the C/OpenMP version of the code. The first consideration for this is that the global memory in CUDA device is accessed via 32–, 64–, or 128–byte memory transactions, thus the appropriate data types, should meet these alignment conditions (*i.e.* must be multiple of these transaction sizes) to avoid memory transfer overhead.

```
struct __align__(16) {
    double x;
    double y;
};
```

Listing **4-11**: `double2` structure

The CUDA toolkit provides a set of data structures that meet the requirements mentioned above. One of these data structure is `double2`, which is illustrated on listing **4-11**. These built-in data structures can improve the efficiency of memory access since they require fewer

memory transactions to move the same amount of data. Along `double2`, another built-in data types are available such as `int2`, `float4`, among others. The proposed data structure for `BeckeGrid` using built-in CUDA data types is shown in listing **4-12**.

```
struct _becke_cuda {
    int2 gridDim;   // Dimensions of the grid (radial, angular)
    double2 *xy;    // coordinate x and y.
    double2 *zw;    // coordinate z and weights.
};
```

Listing **4-12**: `BeckeGrid` structure for CUDA implementation

Additional considerations in memory management were taken into account such as the use of shared memory. For instance, in the case of reductions, the performance is improved dramatically when the reduction is performed with the aid of a temporal array allocated in the shared memory, an example of this strategy is illustrated in listing **4-13**.

```
const unsigned int i = __umul24(blockIdx.x, blockDim.x) + threadIdx.x;

__shared__ double temp[THREADS_PER_BLOCK];
__shared__ double sum_block;

temp[threadIdx.x] = 0.0;
sum_block = 0.0;

if (i < size) {
temp[threadIdx.x] += work[i] * weights[i];
}
__syncthreads();
atomicAdd(&sum_block, temp[threadIdx.x]);

__syncthreads();
if (threadIdx.x == 0) {
atomicAdd(integral, sum_block);
}
```

Listing **4-13**: Two-step reduction using the shared memory of the CUDA device.

Furthermore, the shared memory was also used to reduce the global-memory-load opera-

tions when, for instance, the data allocated in the global memory is required for all threads simultaneously. For example, in listing **4-14** the shared memory is used as a buffer to store the data required by all the threads.

```
__shared__ double buffer[THREADS_PER_BLOCK];

function_value = 0.0;
for (int i = 0; i < n_cont; ++i) {
    for} (int j = threadIdx.x; j < n_cont; j+=THREADS_PER_BLOCK) {
    buffer[j] = dens[i * n_cont + j];
}
__syncthreads();
temp_val = 0.0;
for (int j = 0; j < n_cont; ++j) {
    temp_val += basis_val[j] * buffer[j];
}
```

Listing **4-14**: Example of buffering in CUDA shared memory.

Finally, the parallelized code was split into smaller kernels to reduce the number of registers needed for each kernel. This strategy allows a better occupancy on the device (*i.e.* more blocks running simultaneously).

CUDA performance

In this apart, we show the metrics and the performance of CUDA implementation for the case of multicenter numerical integration.

The test case used in this analysis is the integration of $\rho(\mathbf{r})$ for the diatomic molecules H_2 and O_2 in different grid sizes. Three global kernels are our main focus here, `becke_weights_kernel`, `atomic_grid_integrate_kernel` and `density_gto_kernel` which correspond to Becke weights calculation, integration and calculation of the integrand.

Prior to analyzing the timing and speedup results, we will show some detailed information about the performance of the CUDA kernels. table **4-3** contains several performance metrics for all kernels.

In CUDA programming, the *occupancy* is referred to the utilization of the device regarding the number of concurrent blocks that are being executed by each multiprocessor. In this sense, the optimization of the occupancy will impact the performance since more occupancy

means more utilization of the computing capacity of the CUDA device. In principle, an occupancy greater than 50% is considered to be acceptable. From table **4-3** it is clear that all our implemented kernels have a high occupancy level.

Additionally, the efficiency of the load/store process from global memory is perhaps the most important metric to be optimized due to the high latency of the global memory in CUDA devices. In practice, any optimization on the memory throughput will improve the global performance of a given kernel dramatically. In our implementation, table **4-3**, the lowest memory load efficiency was evidenced in the `becke_weights_kernel` as a consequence of the non-coalesced arrangement of several precomputed data. In the remaining kernels, the memory efficiency was higher, meaning that the kernels are providing a performance near to the actual device limit.

Figure **4-5** shows the time and speedup reached by our implementation for several grid sizes and two different systems. It can be seen that the speedup depends on the problem size, that is, the smaller grid size, the smaller speedup. In the case of medium (1202×500) to big grid sizes (5810×1000–2000) it can be reported a speedup of about $30\times$.

Compared to OpenMP, figure **4-6** shows that CUDA speed up is greater than OpenMP's for medium to large grid sizes. For small grids (not in the plot) such as 194×50 grid, the performance is better in OpenMP than in CUDA because of the overhead of data transfer which can not be compensated by the computational speedup provided by the CUDA device.

4.2.3. Two-electronic Coulomb integration

In this section, we will discuss the performance of the calculation of two-electron Coulomb integrals. As explained in chapter 2, the calculation of this particular integral includes the solution of Poisson's equation for the potential of a given charge distribution. The algorithm to calculate the two-electron Coulomb integrals is shown in figure **4-7**.

	Kernel		
Metric	Weights	Integrate	Density
Multiprocessor Activity	99.99	99.97	99.99
Achieved Occupancy	73.01	61.77	95.20
Global Memory Load Efficiency	70.00	97.73	84.87
Global Memory Store Efficiency	100.00	100.00	100.00

Table **4-3**.: NVIDIA profiler metrics for integration of $\rho(\mathbf{r})$ for O_2 molecule. $6-31{+}G^{**}$ basis set used. Grid size: 5810 angular $\times$ 1000 radial points.

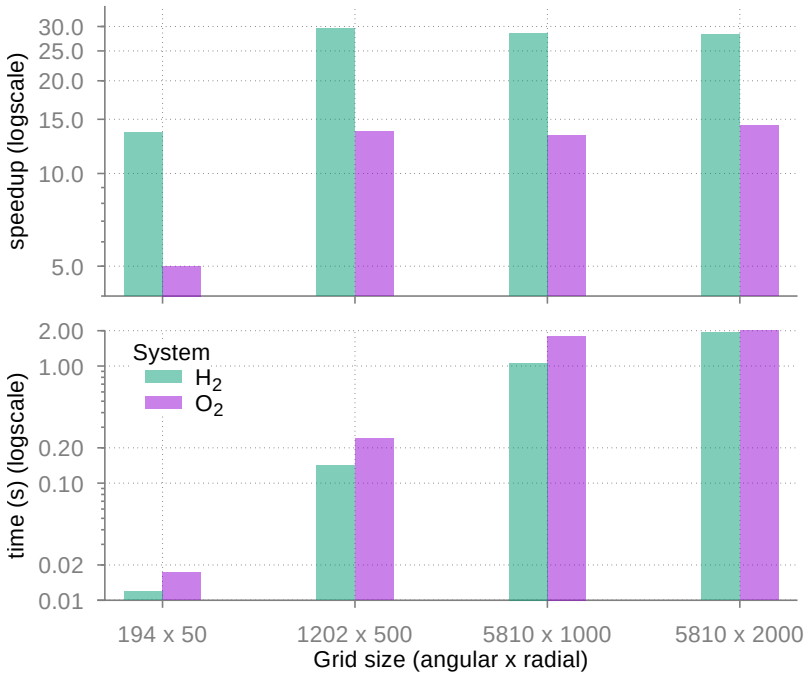

Figure **4-5**.: Time and speedup vs Grid size for the integration of $\rho(\mathbf{r})$ for H_2 and O_2 on CUDA device. Basis set used 6–31+G**. Grid size, angular $\times$ radial points.

As can be seen in figure **4-7**, the two-electron Coulomb integration follows the same procedure of multicenter numerical integration. In other words, the procedure called *calculate the integrand* in figure **4-2** is in this case the calculation of $V_{\alpha\beta}$ plus the calculation of $\rho_{\gamma\nu}(\mathbf{r})$.

It is important to point out that the solution of equation (2-48) for $U_{\ell m}(\mathbf{r})$ functions is done by using the finite elements (FE) method. The FE method involves the solution of a linear system $Ax = b$ for x values $(U_{\ell m}(\mathbf{r}))$ using a tridiagonal matrix A of coefficients. Since the matrix, A is sparse, direct or iterative sparse solvers have been used to improve the performance.

Serial performance

We now focus our attention on the two-electron Coulomb integral

$$I_{\alpha\beta,\gamma\nu} = \iint \frac{\phi_\alpha(1)\phi_\beta(1)\phi_\gamma(2)\phi_\nu(2)}{r_{12}} d^3r_1 d^3r_2, \tag{4-3}$$

of the H_2 molecule. In equation (4-3), ϕ_μ correspond to the μ–th basis function of the linear

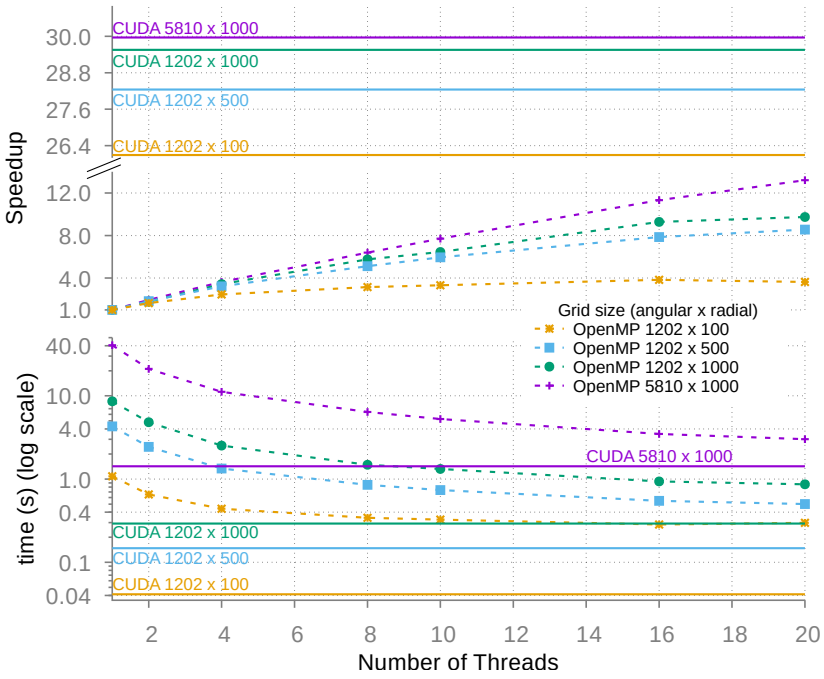

Figure **4-6**.: Time and speedup vs number of threads for the integration of $\rho(\mathbf{r})$ for H_2 molecule using different grid sizes. The dashed line corresponds to OpenMP and solid to CUDA. Basis set used 6–31G**.

combination for the atomic orbital χ_i with coefficients $C_{\mu i}$.

$$\chi_i = \sum_{\mu=1}^{k} C_{\mu i}\phi_\mu. \tag{4-4}$$

The calculations for this test were performed with the STO–3G basis set and with different grid sizes. The following is the profiling using a grid of 194 angular $\times$ 500 radial points:

```
328557 function calls (322104 primitive calls) in 0.500 sec

Ordered by: internal time
ncalls  tottime cumtime filename:lineno(function)
66/56    0.056   0.062  {built-in method _imp.create_dynamic}
  360    0.037   0.037  {built-in method marshal.loads}
  144    0.034   0.034  {built-in method scipy.sparse.linalg}
    1    0.028   0.028  atomic.py:52(spherical_expansion)
    6    0.023   0.024  primitive_gaussian.py:71(compute)
```

The `scipy.sparse.linalg` Function refers to the sparse solver from the SciPy library. We highlight that both integration procedure and the construction of the grids have been already

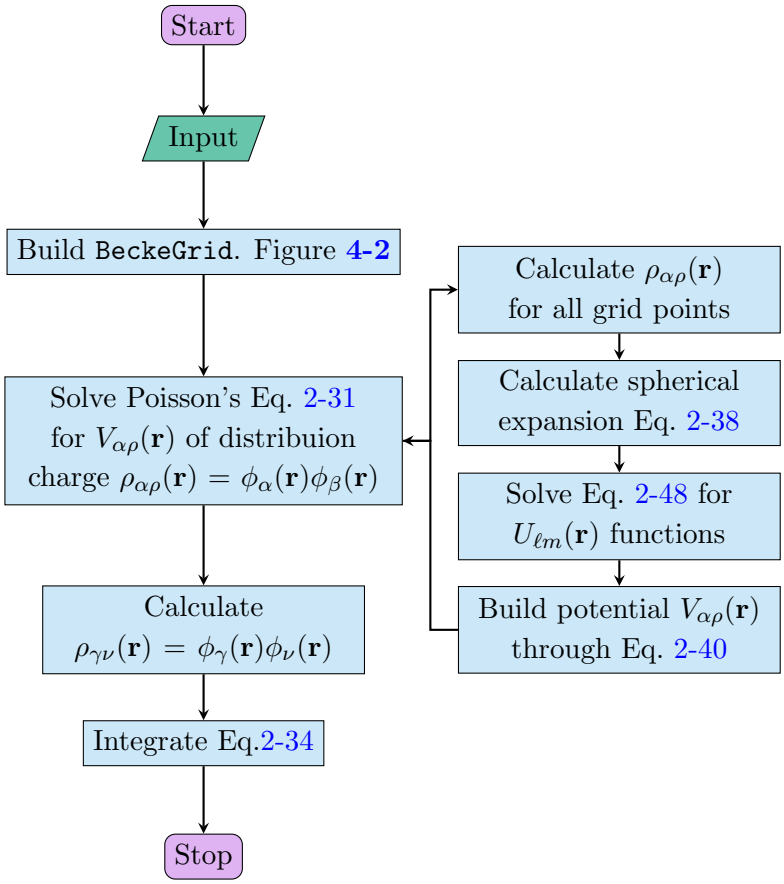

Figure **4-7**.: Algorithm to perform two-electron Coulomb numerical integration.

parallelized. From the previous profiling results, it can be seen that there is not any advisable bottleneck. However, let us try again with a bigger grid (1202 × 500).

```
548071 function calls (540106 primitive calls) in 3.948 sec

Ordered by: internal time
ncalls  tottime cumtime filename:lineno(function)
    1    1.595   1.595  atomic.py:71(evaluate_expansion)
    1    1.002   1.002  atomic.py:52(spherical_expansion)
  900    0.177   0.177  {built-in method scipy.sparse.linalg}
    6    0.143   0.143  primitive_gaussian.py:71(compute)
66/56    0.056   0.062  {built-in method _imp.create_dynamic}
```

In this case, there are two advisable hotspots suitable for parallelization; `evaluate_expansion` which corresponds to the construction of the potential through equation (2-40), and the `spherical_expansion` (harmonic or multipolar expansion equation (2-38)).

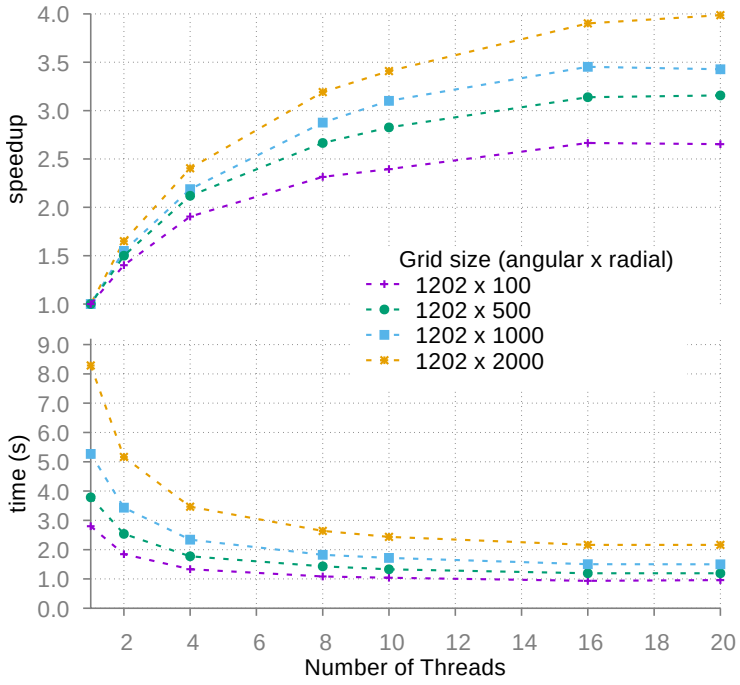

Figure **4-8**.: Time and speedup vs number of threads for two-coulomb integration of H_2 STO−3G basis set at different grid sizes.

OpenMP performance

According to the profiling results, OpenMP parallelization was performed over the routines; `evaluate_expansion` and `spherical_expansion`. Figure **4-8** shows the achieved improvements on the performance.

The OpenMP implementation reports scalability up to 16 cores, where the serial part of the code becomes more relevant see equation (4-2). Moreover, a speedup from 2.5 to 4.0x is achieved depending on the grid size. Further optimizations, such as the utilization of an external sparse solver with OpenMP and CUDA support can improve the performance reported here.

5. Results

Here we summarize the contributions made during the execution of this work.

5.1. Summary of the papers

Paper I (see Appendix A)

The any-particle molecular orbital (APMO) theory was initially implemented by González *et al.* in the computational package named *APMO*.[6] In this implementation, the code was limited to the integration of Gaussian-type orbitals (GTO) with angular momenta no greater than *(d)*. Moreover, APMO only implemented the restricted Hartree-Fock (RHF) and Møller-Plesset perturbation to second order (MP2) levels of theory. In a subsequent contribution,[67] the code was extended to perform integration of GTO with any angular momenta as well as to perform unrestricted Hartree-Fock (UHF) calculations.

More recently, APMO was merged with PARAKATA software [68] in a new version of APMO called LOWDIN. This new version of the code allowed the description of quantum particles using either Density Functional Theory (DFT) or auxiliary perturbation theory (ADPT), as well as the calculations with the electron propagator theory (EPT).[28].

As an initial approach to the understanding of APMO theory, Posada E. implemented a new framework to merge the mentioned codes including OpenMP parallelization for the RHF, UHF and self-consistent field codes. Furthermore, Posada E. wrote the first draft of the manuscript in which a basic introduction to LOWDIN's key computational details and capabilities were review.

Paper II (see Appendix B)

The initial study of nuclear quantum effects (NQE) by using post-HF methods within the APMO framework, besides the already implemented MP2 theory, was performed through the inclusion of the coupling operator into high correlated electronic structure calculations. This integration was carried out by interfacing the APMO code with the MOLPRO package in the so-called APMO-MOLPRO interface.

One of the conclusions of this contribution suggested that before the multi-component (MC) implementations can be used to represent the molecular energy levels accurately beyond the Born-Oppenheimer approximation (BOA), it is critical to address a series of conceptual issues. These theoretical problems are associated with the non-separation of the center-of-mass, the insufficient flexibility of the nuclear basis sets and, the non-inclusion of the electron-nuclear correlation.

As a consequence of these conceptual issues when using MC methodologies for non-BOA calculations, we redirected our investigation to the study of exotic systems only. In these systems, the nuclei are treated as point charges allowing us to focus our studies on the basis set problem only.

In this contribution, Posada E. implemented and tested the aforementioned APMO-MOLPRO interface, and performed some of the reported calculations.

Paper III (see Appendix C)

Motivated by experimental results on the collisional reaction of $He\mu^+ H_2 \longrightarrow He\mu H + H$,[69] and based on the previous contribution of Moncada *et al.*, we started our studies in exotic systems by analyzing the quantum effect of the muon in such reaction. The experimental results reported that the $He\mu$ behaves like a heavy isotope of Hydrogen because the negative muon almost perfectly screens one proton charge in the He atom due to its mass. However, in this contribution, besides to this mass effect, a small, but significant quantum muon effect has been quantified using APMO theory.[58]

Also, we found that the correlation muon-electron is small, making this system a perfect choice for the analysis of basis set related issues. Furthermore, this study reveals that the differences in the ionization potentials of isoelectronic muonic atoms and regular atoms are of the order of millielectronvolts. For the valence ionizations of muonic helium and muonic lithium, the nuclear mass effects are more important. On the other hand, for 1s ionizations of muonic atoms heavier than beryllium, the quantum muon effects are more important.

Posada E. performed the calculation of ionization potentials for all regular atoms and the analysis of the $He\mu^+ H_2$ reaction. Additionally, he wrote the first draft of this contribution.

Paper IV (see Appendix D)

In this contribution, we have shown complete theoretical details on the development of the APMO grid-based HF (APMO-GBHF) approach. Also, we have performed calculations for electronic and multispecies systems. In these calculations, it was observed that the orbital

optimization improves not only the total energy, which is comparable to the HF-limit but also the description of the nuclear cusp.

Along the lines of our research interests, we have studied the exotic system Heμ. We have found that an accurate integration of the muonic orbitals, requires a different radial quadrature due to severe oscillations in the Gauss-Chebyshev nodes. As a consequence, we have proposed a different quadrature reaching an accuracy of 10^{-4} Hartree.

Posada E. has made all the theoretical development, as well as the computational implementation, the calculations and the first version of the manuscript. This contribution is the first of a series of papers related to the application of the APMO-GBHF approach to exotic systems, as well as to nuclear quantum effects. The prior application has to face the aforementioned conceptual issues of non-BOA MC methodologies by including explicitly correlated functions, or further extensions to second-quantized versions of the proposed grid-based approach.

6. Conclusions and perspectives

We have presented the any-particle molecular orbital grid-based Hartree-Fock (APMO-GBHF) method inspired by the grid-based HF approach proposed by Hirata *et al.* This method has allowed us to calculate, at APMO-HF level of theory, systems containing exotic particles such as negative muons μ^-, positrons, and others. The APMO-GBHF method uses a minimal basis set calculation as an initial guess and reports energies and densities near to the HF basis-set limit after an exhaustive orbital optimization.

Additionally, we have implemented the APMO-GBHF methodology in a computational package named Nu-APMO (numerical any particle molecular orbital). This code has been developed in C++/Python and parallelized with OpenMP and CUDA. The overall computational cost of an APMO-GBHF calculation scales $O(n_{species} n_{occ} {n^2}_{atom} n_{rad} {n^2}_{ang})$ and since each grid point can be calculated separately it scales linearly with the number of processors.

Our proposed method offers a solution to the problem of basis set choice for exotic particles in a multicomponent (MC) framework. Additionally, it could be used for basis set refinements in the electronic case. Furthermore, the method reduces the nuclear cusp problem for electronic or positronic species in MC calculations.

It is important to point out that the method developed in this work is the first of its kind, and can be widely exploited by extending this HF version to second-quantized methodologies, as well as to explicitly correlated methods. For the case of inter-species correlation, first-quantized equations with no explicit reference to virtual orbitals should be employed due to our methodology yields only to occupied orbitals.

Moreover, the method can be extended to perform hybrid calculations. For instance, in a system containing electrons and non-electronic quantum species, the electrons could be calculated analytically, while the other species could be calculated numerically. This extension will allow us to calculate larger systems and overtake the problem of the basis set for the non-electronic species. This extension will be reported in future publications.

Appendices

A. Paper I

International Journal of QUANTUM CHEMISTRY

LOWDIN: The Any Particle Molecular Orbital Code

Roberto Flores-Moreno,*[a] Edwin Posada,[b] Félix Moncada,[b] Jonathan Romero,[b] Jorge Charry,[b] Manuel Díaz-Tinoco,[a] Sergio A. González,[b] Néstor F. Aguirre,[c] and Andrés Reyes*[b]

LOWDIN is a computational program that implements the Any Particle Molecular Orbital (APMO) method. The current version of the code encompasses Hartree–Fock, second-order Møller–Plesset, configuration interaction, density functional, and generalized propagator theories. LOWDIN input file offers a unique flexibility, allowing users to exploit all the programs' capabilities to study systems containing any type and number of quantum species. This review provides a basic introduction to LOWDIN's key computational details and capabilities. © 2013 Wiley Periodicals, Inc.

DOI: 10.1002/qua.24500

Introduction

Over the years, quantum chemistry (QC) methods have become essential tools for understanding and predicting a wide variety of molecular phenomena.[1] The growing popularity and success of QC in molecular sciences is mainly due to continuous advances in QC theories and software and the gradual increase in speed and power of the computational hardware.[1–3] The impact of QC on molecular science research is such that nowadays it is common practice in experimental papers to include QC calculations to complement and support their findings and conclusions.[4] Despite the growing popularity of QC, there are still molecular phenomena that cannot be analyzed with current QC programs due to limitations on either the theoretical methodologies or the availability of their computational implementations.

In these cases, molecular scientists are forced to either (a) write their own codes or scripts to process and manipulate the data obtained by using available QC codes, (b) modify the existing computational codes to implement their new theories, or in the worst case scenario (c) write from scratch their own computational codes to implement their new theories.

The two groups currently involved in the LOWDIN project faced all the aforementioned problems. As a result, each group decided separately to create their own computational codes from scratch to use them as platforms for the efficient implementation of new theoretical methods. Andrés Reyes' group developed the Any Particle Molecular Orbital code known as APMO[5,6] and Roberto Flores-Moreno led the development of the electronic structure package named PARAKATA[7] (Butterfly in Purepecha, a native language of central-west Mexico).

At the time of the creation of APMO, GAMESS-NEO was the only freely available computational code capable of performing Nuclear Molecular Orbital (NMO) calculations of electrons and nuclei.[8] Despite all the computational possibilities offered by GAMESS-NEO, the code was only capable of handling two types of quantum species simultaneously (e.g., electrons and protons). APMO emerged as alternative to GAMESS-NEO, with the aim of extending electronic structure methods to any type and number of quantum particles such as nuclei, muons, positrons and pseudo-particles. The last existing version of APMO before it was merged into LOWDIN is capable of performing Hartree–Fock (HF) and MP2 calculations for systems containing any type and number of quantum species.[9–11]

On the other hand, PARAKATA implements Auxiliary Density Functional Theory (ADFT),[12,13] Auxiliary Density Perturbation Theory (ADPT)[14,15] and electron propagator theory (EPT) for electronic structure.[16–22] ADPT capabilities include calculation of electronic contribution to static and dynamic dipole polarizabilities,[14] hyper-polarizabilities,[23] electronic and nuclear Fukui function,[24,25] and other related fields such us the Shannon's entropy response to molecular ionization.[26] As it is inherent to, extensive use is made of auxiliary functions. Similarly to the deMon2k program,[27] auxiliary functions are generated automatically.[28,29] In contrast, PARAKATA uses Cartesian auxiliary functions.[30] In addition, auxiliary functions can also be used in Hartree–Fock and post-Hartree–Fock calculations, such as in electron propagator calculations. In the latter, it has been proven that only minor deviations are caused by using auxiliary functions and the gain in efficiency is considerable.[31]

With the aim of extending the electronic structure methods implemented in PARAKATA to study systems containing other

[a] *R. Flores-Moreno and M. Díaz-Tinoco*
Department of Chemistry, University of Guadalajara, Blvd. Marcelino García Barragán 1421, Guadalajara Jal., C.P. 44430, Mexico

[b] *E. Posada, F. Moncada, J. Romero, J. Charry, S. A. González and A. Reyes*
Department of Chemistry, Universidad Nacional de Colombia, Av. Cra. 30 45-03, Bogotá, Colombia

[c] *N. F. Aguirre*
Instituto de Física Fundamental (C.S.I.C.), Serrano 123, E-28006 Madrid, Spain

E-mail: areyesv@unal.edu.co, roberto.floresm@red.cucei.udg.mx

Contract grant sponsor: Universidad Nacional; contract grant numbers: DIB-201010018545 and DIB-201010016739 (to AR).
Contract grant sponsor: SEP-CONACYT (México); contract grant number: 127362 (to RFM).
Contract grant sponsor: CONACYT; contract grant number: 257420 (to MAD).

© 2013 Wiley Periodicals, Inc.

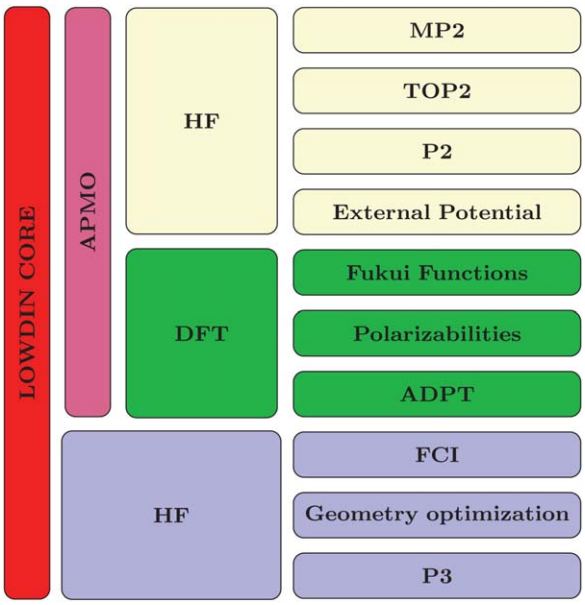

Figure 1. Global structure of the program.

types of quantum species, it was decided to merge PARAKATA and APMO in 2010. This merging process is about to culminate. The resulting code has been named LOWDIN as a tribute to Per Olov Löwdin.

This review article is organized as follows: the section on technical details presents the computational aspects of LOWDIN. The section on capabilities presents the features implemented in LOWDIN and summarizes some of the studies carried out with the code. The section on perspectives talks about the current research and points out theoretical and computational challenges of the APMO theory and the LOWDIN code and strategies for the future.

Technical Details

LOWDIN has been designed to address two challenges:

- It must be capable of performing calculations for systems containing any type and number of quantum species.
- It must have a clear programming standard to simplify the implementation of new extensions.

In this context, LOWDIN has been fully coded in the FORTRAN 2003 standard, with some C/C++ bindings to external libraries. Although FORTRAN 2003 is not a full Object Oriented Programming (OOP) language, most OOP capabilities can be easily emulated, such as class definitions, some polymorphism, and inheritance.[32]

As observed in Figure 1, LOWDIN structure is based on a *CORE* program with small programs around it. These programs are completely encapsulated and independent from one another.

The CORE program

CORE is the main program of LOWDIN. It implements a set of tools to load the input file, generate the molecular system, and run all the requested tasks. This program also includes the *INTEGRALS* and *SCF* programs.

Figure 2 presents an example of an input file. The minimum required blocks to run a calculation are GEOMETRY, TASKS, and CONTROL.

The GEOMETRY block provides the information needed to build the molecular system. The first column declares the type

```
SYSTEM_DESCRIPTION='Muonic water molecule'

GEOMETRY
e-(O)   6-31G           0.0000  0.0000  0.1173   multiplicity=2 addParticles=-1
e-(H)   6-31G           0.0000  0.7572  -0.4692
e-(H)   6-31G           0.0000  -0.7572 -0.4692
u-      13s.ET.O.u.TF   0.0000  0.0000  0.1173
O_16    dirac           0.0000  0.0000  0.1173
H_1     DZSPDN          0.0000  0.7572  -0.4692
H_2     DZSPDN          0.0000  -0.7572 -0.4692
END GEOMETRY

TASKS
        method = "UHF"
        propagatorTheoryCorrection=2
END TASKS

CONTROL
        iterationScheme=3
        convergenceMethod=1
        readCoefficients=F
        hartreeProductGuess=T
END CONTROL
```

Figure 2. Basic input file.

of the quantum species. As shown in Figure 2, e-(H) and e-(O) define the electrons of a Hydrogen and an Oxygen atom, respectively; u- defines a negative muon, O_16, H_1, and H_2 define ^{16}O, ^{1}H, and ^{2}H nuclei, respectively.

The second column declares the basis sets. When the "**dirac**" basis is chosen, the particle is treated as a classical point charge. The third, fourth, and fifth columns declare the *x*,*y*,*z* coordinates of the particle basis set center.

The sixth column provides additional information via keywords **addParticles** and **multiplicity**. These keywords are used to change the default values. **addParticles** is used to modify the number of particles of a quantum species. As shown in the provided example, one electron is removed from the system. **multiplicity** defines the multiplicity for open shell calculations. In the example, an electronic multiplicity of 2 was chosen.

LOWDIN contains a large library of electronic basis sets. Some of the nuclear basis sets developed by Nakai[33,34] and Hammes-Schiffer[8] groups are also available. Home-made basis sets for nuclei, positrons, and muons have been generated by employing the even-tempered basis set scheme[35].

Any type of quantum particles or basis sets can be loaded even if they are not present in the main library. Users can upload new basis sets and quantum species through the addition or modification of some plain text files matching the information provided in the input file.

The TASKS block defines the type of calculation to be performed by LOWDIN. All capabilities are listed in section capabilities. Finally, CONTROL block contains all parameters needed to control the behavior of the program, such as thresholds, maximum number of SCF cycles, etc.

Once the input file is loaded in LOWDIN, the *CORE* program manages the execution of the requested tasks. The communication between the *CORE* program and the other subprograms is carried out through text files.

The INTEGRALS program

This program evaluates the one- and two-particle integrals. One-particle integrals such as overlap, kinetic, and nuclear attraction energy have been implemented for Gaussian basis functions of any angular momentum following Obara and Saika[36] and Head-Gordon and Pople[37] recursive schemes.

Two-particle interaction integrals of the type $(pq|{r_{12}}^{-1}|rs)$ are calculated either with proprietary routines or with LIBINT library.[38] Integrals of the type $\left(pq|e^{-\gamma r_{12}^2}|rs\right)$ are calculated with the LIBINT library. Integrals can be stored on either memory or disk. Integrals stored on disk are collected in stacks containing a maximum of 30.000 of them. Several stacks are calculated simultaneously to exploit the computational power of the machine. Different schemes have been implemented to exploit the permutational symmetry of the integrals.

The SCF program

The SCF program has been designed to minimize the energy of a molecular system composed of multiple quantum species. In a multispecies calculation, LOWDIN creates Fock-like operators for every quantum species. Multiple-species SCF cycles can be performed using any of these three iteration schemes:

1. Full convergence for each quantum species until global convergence is reached, as shown in Figure 3

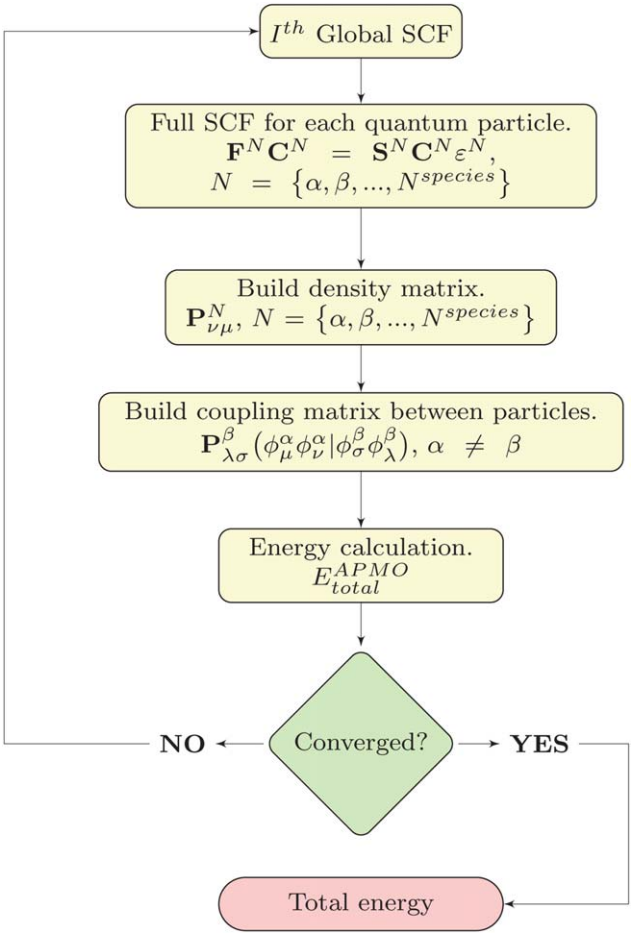

Figure 3. Simultaneous global SCF convergence algorithm.

2. Full convergence of electrons, if any, followed by one iteration for each nonelectronic species
3. One iteration for each quantum species until global convergence is achieved.

Convergence acceleration methods such as DIIS,[39] level shifting,[40] and optimal damping[41] have been implemented and are fully operational for any type of quantum species.

Capabilities

LOWDIN has been designed to be capable of handling different representations of the wavefunctions of fermionic and bosonic species. The current version of code supports Hartree-products, Slater determinants, and symmetric permutations of spin-orbitals. The SCF program can perform Hartree,[42] Hartree–Fock,[6] and DFT[43,44] calculations for any type of quantum species.

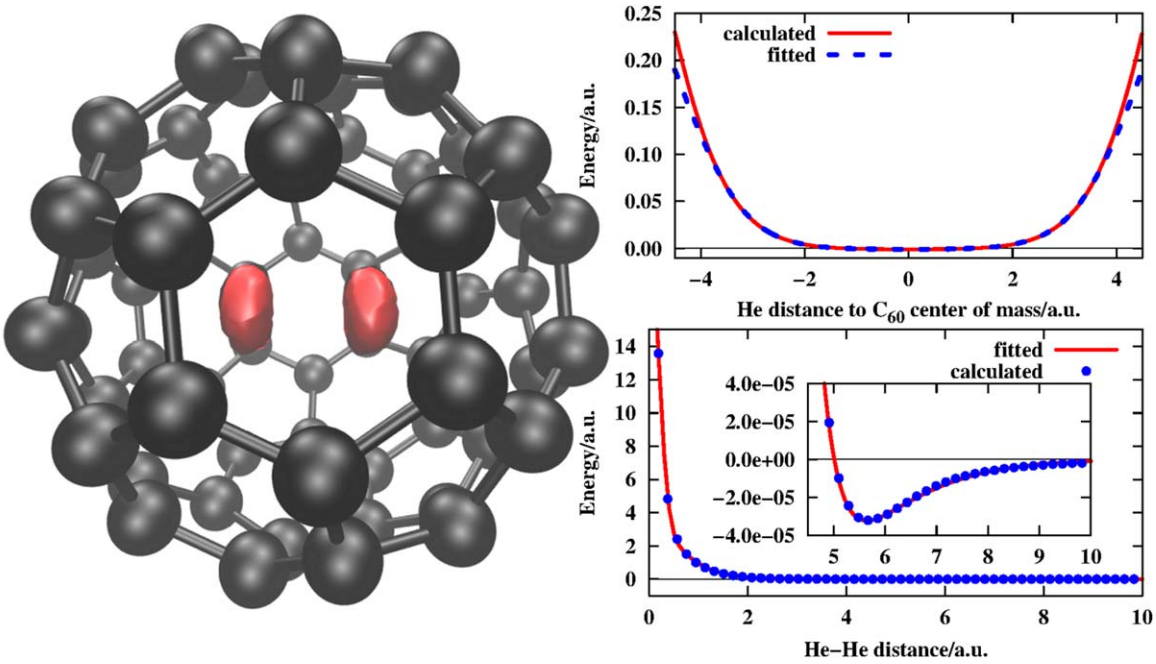

Figure 4. Left: Density contour (0.01 a.u.) of two Helium atoms confined in a fullerene. Right: He—He and He—C_{60} potentials employed in the calculation.

The DFT formalism implemented LOWDIN is an extension of the ADFT developed for electronic structure.[45] At present, the electronic Slater–Dirac exchange[46,47] and Vosko et al. correlation functionals.[48] Electronic BLYP, B3LYP, PBE, and PBE0 functionals are currently being implemented. Nakai's Colle-Salvetti-type nuclear-electron correlation functional[44,49] is also available. New interparticle correlation functionals for different combinations of quantum species are being developed.

LOWDIN contains a set of modules to perform post-Hartree–Fock calculations for systems comprised of any type and number of quantum species. Post-Hartree–Fock methods include second-order Møller–Plesset perturbation theory,[10,42] second-order propagator theory for the calculation of any particle binding energies,[50,51] and configuration interaction singles and doubles.[52] We are currently implementing coupled cluster and third-order propagator methods for any type of quantum species.

Full-CI (FCI) calculations for only one type of quantum species can be performed in LOWDIN. These calculations employ the FCI routine developed by Knowles et al. for electrons.[52,53] The FCI method can be used, for instance, to include electronic correlation using as reference the electronic wavefunction obtained from a APMO-HF calculation.[54] In a similar fashion, nuclear quantum effects (NQEs) on electronic polarizabilities and Fukui functions can be obtained by ADPT calculations, based on the electronic density of an APMO–ADFT calculation.[55] These methodologies will be extended to any type of quantum species in the near future.

APMO calculations for systems containing particles experiencing non-Coulombic interactions can be carried out in LOWDIN. To this aim, the interparticle interaction potentials are introduced as linear combinations of Gaussian functions. The resulting integrals are solved using the LIBINT library.[38] With this methodology the quantum nature of pseudo-particles, such as dressed nuclei and quantum, can be studied. For instance, Figure 4 shows the density of two helium atoms inside a fullerene, where the helium–helium and helium–fullerene interactions are described as a two-particles potential and a central potential, respectively. The study of the quantum behavior of confined species in fullerenes is in progress in our group. In addition, LOWDIN can perform APMO calculations on systems constrained to one or two dimensions. These capabilities will have direct application to study of quantum wires and wells.

Study of NQEs

Earlier applications of APMO and LOWDIN concentrated on the investigation of hydrogen isotope effects on covalent and noncovalent interactions. Similar studies have been carried out by other research groups employing NMO methodologies.[33,56–66]

In a first series of studies we examined, the H/D/T isotope substitution effects on the geometry and electronic structure of hydrogen molecule,[6] water,[6] hydrogen halide dimers,[5,67] and $[XO_3SOHOSO_3X]^-$ (X = H,K) complexes[68] at the APMO/HF level. These studies revealed that nuclear delocalization impacts the geometry and stability of hydrogen bonds, affecting macroscopic properties. Our APMO/HF results qualitatively agree with the experimental isotopic substitution trends.

With the APMO/MP2, we have studied NQEs on the geometries and energies of small protonated rare gas clusters (Rg_nX^+, Rg = He, Ne, Ar, X = H, D, T, and $n = 13$).[10,69]. We proposed an APMO/MP2 energy decomposition analysis scheme that revealed how NQEs impact the electrostatic, polarization,

charge transfer, and dispersion interactions contributing to the stabilization of the complexes.

A similar study was conducted for assessing the H/D secondary isotope effect on the binding energies of water–alkaline cation complexes, Alk^+ $(X_2O)_n$ (X = H, D; Alk = Li, Na, K; $n = 1$–4).[70] Our results revealed that deuteration reduces the magnitude of the electrostatic and polarization interactions between the cation and the water molecule via an inductive effect. This important result is the first in a series of studies aiming for understanding hydrogen isotope effects on hydration, an important topic for biomolecular sciences[71].

An APMO/MP2 study conducted for the $[CNHNC]^-$ complex[72] revealed the importance of including nuclear-electron correlation in APMO calculations. We discovered that while a NMO/HF calculation produced a minimal energy structure presenting an asymmetric hydrogen bond, the APMO/MP2 calculation produced a symmetric H-bond structure in agreement with available experimental data. This study confirmed the importance of including NQEs for an enhanced description of strong-low-barrier H-bonded systems.

We have proposed an extended propagator theory for electrons and other types of quantum particles.[50] In a first application of the method, we analyzed NQEs and isotope effects on electron ionization energies of molecular systems. An energy decomposition analysis of the total ionization energies revealed that the calculated electron ionization energies correspond to nearly vertical processes. Our results reveal that including NQEs improves the estimation of ionization energies for systems experiencing Jahn–Teller effects in the photo-electron spectra.

The APMO propagator theory has also been applied to study proton detachment processes.[51] We calculated the proton binding energies (PBEs) and proton affinities (PAs) for some inorganic and organic molecules, finding an excellent agreement between our predictions and the experimental values. We also combined our methodology with a systematic exploration of the energy surface of protonated water clusters, $(H_2O)_nH^+$ $(n = 1-7)$, to estimate the proton hydration free energy. Our prediction of -270.2 kcal/mol is in excellent agreement with other results reported in the literature. This work suggests that the second-order proton propagator method has the potential to become a powerful tool for predicting proton acid/base properties (Fig. 5). Currently, we are working on the implementation of higher-order approaches and the combination of the proton propagator with an implicit solvation model aiming for the accurate prediction of pK_as.

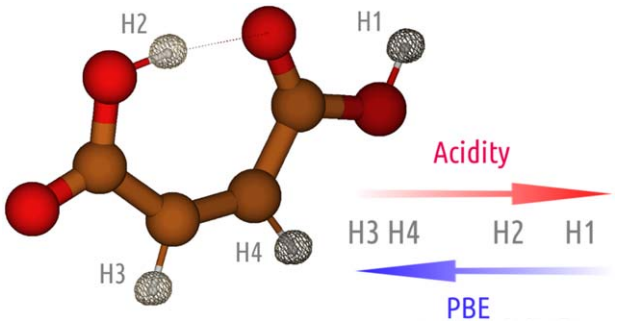

Figure 5. The proton propagator, implemented in LOWDIN program, is a promising tool for predicting proton acid/base properties. Here, an example of how the proton binding energies (PBE) describe differences in the acidity of the protons of maleic acid.

Chemistry of exotic particles

Negative Muons Chemistry. In a series of recent papers, Fleming and coworkers[73–75] reported the measurement of reaction rates for the $^4He(\mu) + H_2 \rightarrow {}^4He(\mu)H + H$ collisional process. Perhaps, the most surprising finding of their research is that $He(\mu)$ chemically behaves as a heavy isotope of hydrogen. Inspired by this finding, the chemical properties of muonic atoms and molecules have also been investigated with LOWDIN. A muon is a particle with the same charge and spin of the electron but has a mass of 206.8 times larger. A comparison between the electronic and muonic radial distributions in atoms revealed that muons are much more localized than electrons. As a result, the muonic cloud screens almost one positive charge of the nucleus. Our results for electronic densities and ionization potentials revealed that by replacing an electron in an atom by a muon there is a transmutation of the electronic properties of that atom to those of the element with atomic number $Z - 1$.[35] In a more recent study of muonic systems, we found that the electronic properties of atoms containing two negative muons are very similar to those of all-electron atoms with atomic number $Z - 2$.[76] For diatomic molecules, these muonic effects are more diverse, ranging from the transmutation of atomic properties to drastic changes in equilibrium geometries and energies.[76] In Figure 6, we plot the muonic and electronic densities of a $He\mu H$ molecule. This figure clearly reveals that the muon is very close to the He nucleus, and that from the electrons perspective, the $He\mu^+$ moiety behaves as a H nucleus.

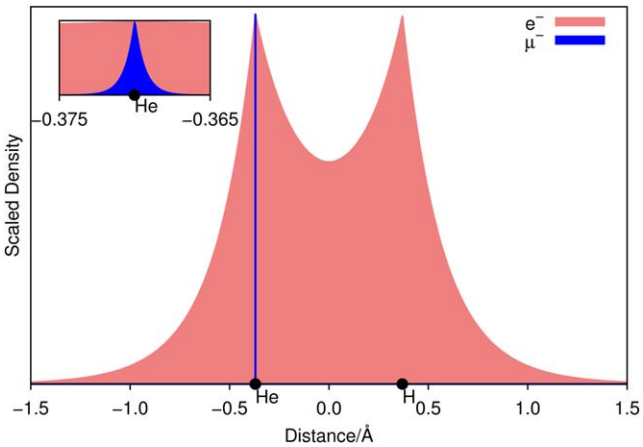

Figure 6. APMO/HF electronic and muonic densities of a $He\mu H$ molecule. Densities were scaled to share the same maximum. The muon density is zoomed at the upper left corner box.

In our latest study, we have compared the electronic ionization potentials of isoelectronic muonic and all-electron atoms

at the full-CI level.[52] We found that the differences in the ionization potentials are only of the order of meV. Furthermore, we found that the difference in nuclear masses and the incomplete screening of the muon account for the observed discrepancies. Therefore, from these calculations we conclude that muon–electron correlation as well as the muon relaxation energy is negligible upon the removal of an electron. In addition, we quantified the partial muonic screening effect for the $H_2 + {}^4He\mu$ reaction[52] by comparing our calculated energy barriers with those obtained considering infinite nuclear masses $H_2 + H$. We observed that the partial muonic screening reduces the energy barrier by 0.8 meV. Although this effect is very small for most chemical applications, it should be considered for precise calculations aiming for spectroscopic accuracy.

Positrons Chemistry. We have calculated the APMO/EP2 positron binding energies of the 20 standard amino acids considering three different molecular conformations: classical, H-bonded, and zwitterion (Charry et al., Chem. Phys. Lett. in preparation). Our results are in good qualitative agreement with those of Tachikawa and coworkers.[77] An analysis of these results reveals that positron binding energies and densities vary dramatically among the different conformers. Figure 7 depicts APMO/HF positronic (in red) and electronic (in blue) densities of a positronic glycine zwitterion. As observed in this figure, positron density is very delocalized throughout the molecule.

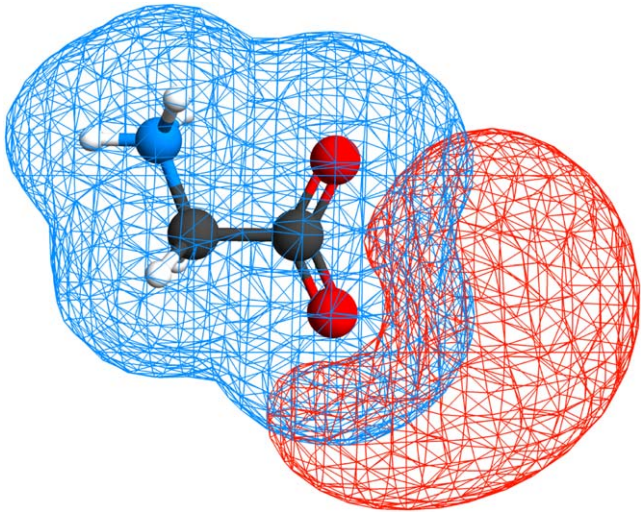

Figure 7. APMO/HF electronic (in blue) and positronic (in red) density plots for the positronic glycine zwitterion. A contour value of 0.001 was employed.

Perspective

LOWDIN code stands out as a versatile platform for the efficient computational implementation of new theories and for the quantum calculation of properties of regular and exotic molecular systems. At the programming level, electronic structure modules are generalized to an APMO framework using the OOP capabilities. From the theoretical and computational perspectives, these extensions entail new challenges.

One is the poor description of translations and rotations by Gaussian-type functions basis functions in the NMO method, which leads to the appearance of spurious terms in the multispecies Hamiltonian. We are currently working on removing these contaminations by implementing the schemes developed by Nakai.[34,78,79] Closely related is the possibility to implement basis set free molecular orbital calculations.

A second challenge is the interspecies correlation, in particular, when charges of the particles under consideration have different signs. In those cases, multiconfigurational[64] or explicitly correlated schemes[80] should be employed for accurate calculations. Both schemes are currently explored in our groups.

The convergence of the multispecies SCF presents another challenge. While electronic calculations take about 20 to 50 SCF cycles, multispecies calculations usually take from 100 to 1000, regardless of the iteration scheme chosen. New convergence schemes need to be explored for such cases.

Of special interest is the inclusion of temperature and solvent effects. We are working on the implementation of a temperature dependent SCF and propagator methods aiming for the direct calculation of temperature corrected acid/base and redox chemistry properties.

In its current stage, the LOWDIN program can handle SCF calculations of more than 100 atoms.[43] With the aim of studying larger systems, we are porting LOWDIN to graphics processing units (GPUs). We hope that combining the above strategy with the implementation of fragments and quantum mechanics/molecular mechanics (QM/MM) techniques, the calculation of systems of biological interest will be possible.

Finally, LOWDIN binaries can be requested for academic use.

Keywords: nuclear quantum effects · isotope effects · APMO method · exotic molecules · propagator method

How to cite this article: R.Flores-Moreno, E.Posada, F.Moncada, J.Romero, J.Charry, M.Díaz-Tinoco, S. A.González, N. F.Aguirre, A.Reyes, *Int. J. Quantum Chem.* **2014**, *114*, 50–56. DOI: 10.1002/qua.24500

[1] T. D. Crawford, S. S. Wesolowski, E. F. Valeev, R. A. King, M. L. Leininger, H. F. Schaefer, III, The Past, Present, and Future of Quantum Chemistry in Chemistry for the 21st Century (eds E. Keinan and I. Schechter), Wiley-VCH Verlag GmbH: Weinheim, **2007**; pp. 219–246.
[2] R. A. Friesner, *PNAS* **2005**, *102*, 6648.
[3] I. Kassal, J. D. Whitfield, A. Perdomo-Ortiz, M.-H. Yung, A. Aspuru-Guzik, *Annu. Rev. Phys. Chem.* **2011**, *62*, 185.
[4] C. J. Barden, H. F. Schaefer, *Pure Appl. Chem.* **2000**, *72*, 1405.
[5] S. A. González, N. F. Aguirre, A. Reyes, *Rev. Colom. Quim.* **2008**, *37*, 93.
[6] S. A. González, N. F. Aguirre, A. Reyes, *Int. J. Quantum Chem. 108*, **2008**, 1742.
[7] R. Flores-Moreno, J. M. del Campo, T. Ida, *Parakata*, **2008**. Available at: https://sites.google.com/site/gdlquantumchemistrygroup/home/software/parakata. Last accessed 2013/06/21.
[8] S. Webb, T. Iordanov, S. Hammes-Schiffer, *J. Chem. Phys.* **2002**, *117*, 4106.
[9] S. A. González, A. Reyes, *Rev. Colom. Quim.* **2009**, *38*, 117.
[10] S. A. González, A. Reyes, *Int. J. Quantum Chem.* **2010**, *110*, 689.
[11] E. Posada, F. Moncada, A. Reyes, *Rev. Colom. Quim.* **2011**, *40*, 35.

[12] A. M. Köster, J. U. Reveles, J. M. del Campo, *J. Chem. Phys.* **2004**, *121*, 3417.
[13] P. Calaminici, V. D. Domínguez-Soria, G. U. Flores-Moreno, R. Gamboa-Martínez, G. Geudtner, A. Goursot, D. R. Salahub, A. M. Köster, In Handbook of Computational Chemistry, J. Leszczynski, Eds.; Springer: Netherlands, **2012**, pp. 573–610.
[14] R. Flores-Moreno, A. M. Köster, *J. Chem. Phys.* **2008**, *128*, 134105.
[15] J. Carmona-Espíndola, R. Flores-Moreno, A. M. Köster, *J. Chem. Phys.* **2010**, *133*, 084102.
[16] J. Linderberg, Y. Öhrn, Propagators in Quantum Chemistry, 2nd ed., Wiley Interscience: Hoboken, NJ, **2004**.
[17] W. von Niessen, J. Schirmer, L. S. Cederbaum, *Comput. Phys. Rep.* **1984**, *1*, 57.
[18] J. V. Ortiz, *Adv. Quantum Chem.* **1999**, *33*, 35.
[19] J. Simons, *Theor. Chem. Adv. Perspect.* **1978**, *3*, 1.
[20] M. F. Herman, K. F. Freed, D. L. Yeager, *Adv. Chem. Phys.* **1981**, *48*, 1.
[21] Y. Öhrn, G. Born, In Advances in Quantum Chemistry, Vol. *13*; P.-O. Löwdin, Eds.; Academic Press: New York, **1981**; pp. 1–88.
[22] J. V. Ortiz, *WIREs Comput. Mol. Sci.* **2013**, *03*, 123.
[23] J. Carmona-Espíndola, R. Flores-Moreno, A. M. Köster, *Int. J. Quantum Chem.* **2012**, *112*, 3461.
[24] R. Flores-Moreno, J. Melin, J. V. Ortiz, G. Merino, *J. Chem. Phys.* **2008**, *129*, 224105.
[25] R. Flores-Moreno, *J. Chem. Theory Comput.* **2010**, *6*, 48.
[26] K. Pineda-Urbina, R. D. Guerrero, A. Reyes, Z. Gómez-Sandoval, R. Flores-Moreno, *J. Mol. Mod.* **2013**, *19*, 1677.
[27] A. M. Köster, G. Geudtner, P. Calaminici, M.E. Casida, V.D. Dominguez, R. Flores-Moreno, G.U. Gamboa, A. Goursot, T. Heine, A. Ipatov, F. Janetzko, J. M. del Campo, J. U. Reveles, A. Vela, B. Zuniga-Gutierrez, D.R. Salahub, demon2k, **2011**, Available at: http://www.demon-software.com. Last accessed 2013/06/21.
[28] J. Andzelm, E. Radzio, D. R. Salahub, *J. Comput. Chem.* **1985**, *6*, 520.
[29] J. Andzelm, N. Russo, D. R. Salahub, *J. Chem. Phys.* **1987**, *87*, 6562.
[30] A. M. Köster, *J. Chem. Phys.* **2003**, *118*, 9943.
[31] R. Flores-Moreno, J. V. Ortiz, *J. Chem. Phys.* **2009**, *131*, 124110.
[32] ISO/IEC 1539-1:2010, Information technology – Programming languages – Fortran – Part 1: Base language; International Organization for Standardization (ISO: Geneva), **2009**.
[33] H. Nakai, *Int. J. Quantum Chem.* **2002**, *86*, 511.
[34] H. Nakai, M. Hoshino, K. Miyamoto, S. Hyodo, *J. Chem. Phys.* **2005**, *122*, 164101.
[35] F. Moncada, D. Cruz, A. Reyes, *Chem. Phys. Lett.* **2012**, *539–540*, 209.
[36] S. Obara, A. Saika, *J. Chem. Phys.* **1986**, *84*, 3963.
[37] M. Head-Gordon, J. A. Pople, *J. Chem. Phys.* **1988**, *89*, 5777.
[38] J. T. Fermann, E. F. Valeev, Libint: Machine-generated library for efficient evaluation of molecular integrals over Gaussians, **2003**, Available at: http://sourceforge.net/p/libint. Last accessed 2013/06/21.
[39] P. Pulay, *J. Comput. Chem.* **1982**, *3*, 556.
[40] V. R. Saunders, I. H. Hillier, *Int. J. Quantum Chem.* **1973**, *7*, 699.
[41] E. Cancès, C. Le Bris, *Int. J. Quantum Chem.* **2000**, *79*, 82.
[42] F. Moncada, S. González, R. Flores-Moreno, A. Reyes, *Mol. Phys. (submitted).*
[43] F. Moncada, E. Posada, R. Flores-Moreno, A. Reyes, *Chem. Phys.* **2012**, *400*, 103.
[44] J. Charry, F. Moncada, E. Posada, R. Flores-Moreno, A. Reyes, *Chem. Phys. (submitted).*
[45] A. M. Köster, J. U. Reveles, J. M. del Campo, *J. Chem. Phys.* **2004**, *121*, 3417.
[46] P. Dirac, *Proc. R. Soc. London, Ser. A* **1929**, *123*, 714.
[47] J. C. Slater, *Phys. Rev.* **1951**, *81*, 385.
[48] S. Vosko, L. Wilk, M. Nusair, *Can. J. Phys.* **1980**, *58*, 1200.
[49] Y. Imamura, H. Kiryu, H. Nakai, *J. Comp. Chem.* **2008**, *29*, 735.
[50] J. Romero, E. Posada, R. Flores-Moreno, A. Reyes, *J. Chem. Phys.* **2012**, *137*, 074105.
[51] M. Díaz-Tinoco, J. Romero, J. V. Ortiz, A. Reyes, R. Flores-Moreno, *J. Chem. Phys.* **2013**, *138*, 194108.
[52] E. Posada, F. Moncada, A. Reyes, *J. Phys. Chem. A (submitted).*
[53] P. J. Knowles, N. C. Handy, *Comp. Phys. Comm.* **1989**, *54*, 75.
[54] N. F. Aguirre, P. Villarreal, G. Delgado-Barrio, E. Posada, A. Reyes, M. Biczysko, A. O. Mitrushchenkov, M. P. de Lara-Castells, *J. Chem. Phys.* **2013**, *138*, 184113.
[55] R. Flores-Moreno, A. M. Koster, *J. Chem. Phys.* **2008**, *128*, 134105.
[56] M. Tachikawa, K. Mori, H. Nakai, K. Iguchi, *Chem. Phys. Lett.* **1998**, *290*, 437.
[57] M. Tachikawa, *Chem. Phys. Lett.* **2002**, *360*, 494.
[58] M. Tachikawa, *Mol. Phys.* **2002**, *100*, 881.
[59] T. Udagawa, T. Ishimoto, H. Tokiwa, M. Tachikawa, U. Nagashima, *Chem. Phys. Lett.* **2004**, *389*, 236.
[60] A. Reyes, M. Pak, S. Hammes-Schiffer, *J. Chem. Phys.* **2005**, *123*, 064104.
[61] M. F. Shibl, M. Tachikawa, O. Kuhn, *Phys. Chem. Chem. Phys.* **2005**, *7*, 1368.
[62] H. Nakai, Y. Ikabata, Y. Tsukamoto, Y. Imamura, K. Miyamoto, M. Hoshino, *Mol. Phys.* **2007**, *105*, 2649.
[63] H. Nakai, *Int. J. Quantum Chem.* **2007**, *107*, 2849.
[64] T. Ishimoto, M. Tachikawa, U. Nagashima, *J. Chem. Phys.* **2008**, *128*, 164118.
[65] T. Ishimoto, M. Tachikawa, U. Nagashima, *Int. J. Quantum. Chem.* **2009**, *109*, 2677.
[66] Y. Ikabata, Y. Imamura, H. Nakai, *J. Phys. Chem. A* **2011**, *115*, 1433.
[67] I. Ortiz-Verano, S. A. González, A. Reyes, *Rev. Colom. Quim.* **2009**, *38*, 143.
[68] F. Moncada, S. A. González, A. Reyes, *Mol. Phys.* **2010**, *108*, 1545.
[69] F. Moncada, L. S. Uribe, J. Romero, A. Reyes, *Int. J. Quantum Chem.* **2013**, *113*, 1556.
[70] J. Romero, A. Restrepo, A. Reyes, *Mol. Phys*. (submitted).
[71] A. Ben-Naim, *Biopolymers* **1990**, *29*, 567.
[72] D. V. Moreno, S. A. González, A. Reyes, *J. Chem. Phys.* **2011**, *134*, 024115.
[73] D. J. Arseneau, D. G. Fleming, O. Sukhorukov, J. H. Brewer, B. C. Garrett, D. G. Truhlar, *Physica B* **2009**, *404*, 946.
[74] D. Fleming, D. Arseneau, O. Sukhorukov, J. Brewer, S. Mielke, G. Schatz, B. Garrett, K. Peterson, D. Truhlar, *Science* **2011**, *331*, 448.
[75] D. G. Fleming, D. J. Arseneau, O. Sukhorukov, J. H. Brewer, S. L. Mielke, D. G. Truhlar, G. C. Schatz, B. C. Garrett, K. A. Peterson, *J. Chem. Phys.* **2011**, *135*, 184310.
[76] F. Moncada, D. Cruz, A. Reyes, *Chem. Phys. Lett.* **2013**, *570*, 16.
[77] K. Koyanagi, Y. Kita, M. Tachikawa, *Eur. Phys. J.* **2012**, *D 66*, 1.
[78] M. Hoshino, H. Nakai, *J. Chem. Phys.* **2006**, *124*, 194110.
[79] K. Miyamoto, M. Hoshino, H. Nakai, *J. Chem. Theory Comput.* **2006**, *2*, 1544.
[80] M. Hoshino, H. Nishizawa, H. Nakai, *J. Chem. Phys.* **2011**, *135*, 024111.

Received: 26 April 2013
Revised: 31 May 2013
Accepted: 5 June 2013
Published online on 1 July 2013

B. Paper II

Including nuclear quantum effects into highly correlated electronic structure calculations of weakly bound systems

Néstor F. Aguirre,[1] Pablo Villarreal,[1] Gerardo Delgado-Barrio,[1] Edwin Posada,[2] Andrés Reyes,[2] Malgorzata Biczysko,[3] Alexander O. Mitrushchenkov,[4] and María Pilar de Lara-Castells[1,a)]

[1]*Instituto de Física Fundamental (C.S.I.C.), Serrano 123, E-28006 Madrid, Spain*
[2]*Departamento de Química, Universidad Nacional de Colombia, Av. Cra. #45-03 Bogotá, Colombia*
[3]*Center for Nanotechnology Innovation @NEST, Istituto Italiano di Tecnologia, Piazza San Silvestro 12, I-56127 Pisa, Italy and Scuola Normale Superiore, Piazza dei Cavalieri 7, I-56126 Pisa, Italy*
[4]*Université Paris-Est, Laboratoire Modélisation et Simulation Multi Echelle, MSME UMR 8208 CNRS, 5 bd Descartes, 77454 Marne-la-Vallée, France*

(Received 23 February 2013; accepted 17 April 2013; published online 14 May 2013)

An interface between the APMO code and the electronic structure package MOLPRO is presented. The any particle molecular orbital APMO code [González *et al.*, Int. J. Quantum Chem. **108**, 1742 (2008)] implements the model where electrons and light nuclei are treated simultaneously at Hartree-Fock or second-order Möller-Plesset levels of theory. The APMO-MOLPRO interface allows to include high-level electronic correlation as implemented in the MOLPRO package and to describe nuclear quantum effects at Hartree-Fock level of theory with the APMO code. Different model systems illustrate the implementation: $^4He_2$ dimer as a protype of a weakly bound van der Waals system; isotopomers of $[He–H–He]^+$ molecule as an example of a hydrogen bonded system; and molecular hydrogen to compare with very accurate non-Born-Oppenheimer calculations. The possible improvements and future developments are outlined. © *2013 AIP Publishing LLC*. [http://dx.doi.org/10.1063/1.4803546]

I. INTRODUCTION

It is well known that nuclear quantum effects play a significant role in a wide variety of relevant systems implying light nuclei such as hydrogen-bonded systems and helium droplets. In fact, spectroscopic probes of molecular impurities in helium droplets have shown that while ^{4}He clusters result in superfluid behavior with free-rotor-like molecular spectra, ^{3}He atoms behave as a normal fluid and the impurity spectra are of hindered-rotor type.[1] Since ^{4}He atoms are composite spinless bosons and ^{3}He atoms are fermionic particles with a nuclear spin equal to 1/2, one fundamental question has concerned the influence of the spin and the antisymmetry of the fermionic ^{3}He wave-functions in providing such different response to the molecular rotation. Quantum-Chemistry (QC)-like Nuclear-Orbital (NO) approaches, first introduced by Jungwirth and Krylov,[2] map the problem onto an electronic structure-like problem by considering the helium atoms as *pseudo-electrons* and the dopant molecule as a structured pseudo-nucleus, replacing Coulomb interactions by van der Waals He–He and He-dopant pair potentials. This way, the dopant molecule is considered as fixed, assuming the Born-Oppenheimer (BO) separation between the nuclear motions of the helium atoms and the dopant, and an expansion over Gaussian-type functions (GTFs) centered on the dopant can be employed.[2] Later, this QC-like NO approach was reformulated in internal coordinates by separating the center-of-mass operator from the Hamiltonian and employing radial basis functions centered on the dopant-He internuclear distance, in contrast with standard electronic structure problems. Within this framework, multi-orbital Hartree and Hartree-Fock (HF) implementations were developed.[3,4] Hereafter, the Full-Configuration-Interaction (FCI) NO approach was designed to deal with ^{3}He atoms[5,6] and extended to bosonic ^{4}He atoms and *para*-H_2 molecules.[7] The essential merit of these QC-like approaches consists in using nuclear orbitals to describe one-particle helium states so that bosonic/fermionic symmetry can be easily included[3,5–8] on an equal footing, allowing a natural extension of theoretical concepts that have served molecular structure theory. These approaches rely on the BO approximation so that the nuclear quantum effects (NQE) are introduced after performing the standard clamped-nuclei electronic structure calculations that provide the potential energy surface on which the nuclear motion occurs.

A number of theoretical approaches for NQE that have been developed, are mainly aimed to describe systems involving hydrogen-bonding, hydrogen transfer processes, and small hydrogen-containing molecules beyond the BO approximation. Some of these methods use a one-particle molecular orbital picture for both electrons and the lightest nuclei (e.g., proton, deuteron, etc.), achieving a simultaneous instead of sequential quantum-mechanical description of these particles. The underlying idea was put forward in the late 1960s by Thomas and collaborators[9–12] and applied to methane, ammonia, and water, using Slater orbitals for the protons (SNO). A few years later, Bishop and collaborators[13,14] studied H_2^+ and isotopologues with an accurate non-adiabatic variational approach. It also worths mentioning the molecular coupled-

a)Author to whom correspondence should be addressed. Electronic mail: Pilar.deLara.Castells@csic.es

 © 2013 AIP Publishing LLC

This article is copyrighted as indicated in the article. Reuse of AIP content is subject to the terms at: http://scitation.aip.org/termsconditions. Downloaded to IP: 147.122.21.18 On: Fri, 21 Nov 2014 17:47:01

cluster (MCC) method formulated by Monkhorst in the late 1980s,[15] in which the electrons and nuclei are described simultaneously with the coupled-cluster (CC) approach.

Over the last years, a renewed interest in nuclear-electron orbital approaches has been raised in order to analyze, for instance, isotope effects and hydrogen tunneling. One of their attractive features is the capability of incorporating finite nuclear mass/isotope and spin statistic effects directly into the electronic wave-function, in a contrast with BO treatments where these finite-mass effects are usually incorporated as corrections, either adiabatic or non-adiabatic, to the electronic energies only (see, e.g., Ref. 16). In fact, approaches going beyond the BO approximation and enabling a simultaneous description of electrons and nuclei are very useful when the nuclear de-localization has a marked influence onto the electronic wave-function itself (e.g., proton-coupled electron transfer processes). The most rigorous non-BO methods are aimed to solve the all-particle Schrödinger equation of small atomic and molecular systems as accurately as possible, taking into account the translational and rotational invariance of the molecular Hamiltonian. Within this framework, the methodological contributions from Adamowicz and collaborators[17–19] have the longest history (for a very recent review, see Ref. 19). Starting with the separation of the center-of-mass operator from the molecular Hamiltonian, one key characteristic of these methodological developments is the employment of explicitly correlated Gaussian (ECG) basis functions depending on the inter-particle quantum modes.[17,19] The total wavefunction is then obtained by minimizing the energy functional through the variational principle. Following these ideas, Mátyus and Reiher have very recently developed a new numerical approach,[20] obtaining rotational-vibrational-electronic energy levels with spectroscopic accuracy.

Another branch of non-BO methodologies employs the same strategies and basis-type functions as in standard electronic structure calculations, for the lightest nuclei, fixing the positions of heavier nuclei which are then treated via the BO approximation. An overview of these methodologies has been provided by Sherrill and collaborators[21] and, very recently, by Goli and Shahbazian.[22] They are known by different acronyms, such as multi-component molecular orbital (MCMO), nuclear orbital plus molecular orbital (NOMO), nuclear-electronic orbital (NEO), and *any-particle* molecular orbital (APMO), as described below. A scheme considering the most popular approaches and illustrating their evolution over the time is shown in Figure 1. All of them employ GTFs to expand the one-particle orbitals of electrons and quantum nuclei, as in standard molecular orbital calculations, constructing Slater determinants and permanents for fermionic and bosonic quantum particles, respectively. The zeroth-order electronic-nuclear wavefunction is then written as the product of these determinants and permanents. In what follows, adopting the same terms as used by Sherrill and collaborators,[21] these approaches will be referred to as electronic and nuclear molecular orbital (ENMO) approaches.

To our knowledge, the NOMO method, introduced by Nakai and collaborators in the late 1990s,[23] represents the earliest ENMO-type contribution (see, for example, Ref. 24 for a revision). There, self-consistent mean-field equations

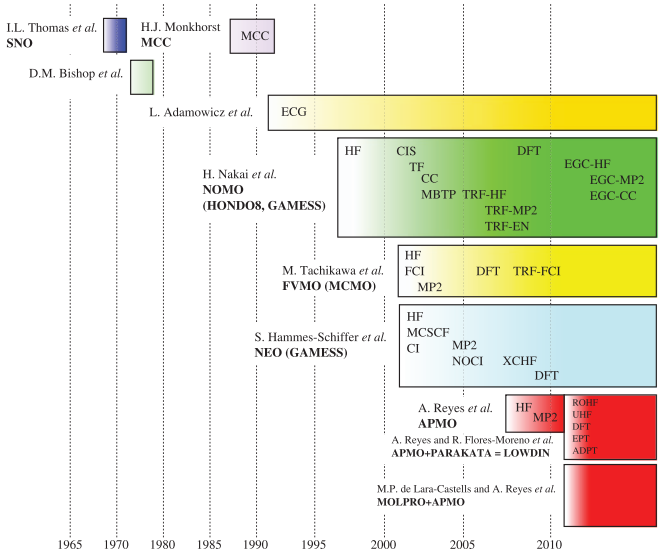

FIG. 1. Scheme illustrating the evolution over the time of methodological and computational ENMO implementations.

for electrons and nuclei were derived in the usual QC notation, and applied using variationally optimized GTFs. Already at the earliest stages of its development, however, the NOMO approach was extended to treat electronic and excited vibrational states with the single configuration interaction (CIS) method,[25] and re-formulated to rigorously remove the center-of-mass motion[26] from the total Hamiltonian (i.e., the translation-free (TF) NOMO version). Moreover, correlation effects were also incorporated by adopting many-body perturbation theory (MBPT) and the CC approach,[27] clarifying the major role of the electron-nucleus correlation. Further developments[24,28–30] allowed to approximately substrate the rotational contribution[29,31] also (i.e., the translation- and rotation-free (TRF) NOMO version[28]). The TRF-NOMO implementation was also extended to incorporate many-body correlation effects with second-order Möller-Plesset (MP2) and Epstein-Nesbet (EN) perturbation theory.[30] More recently, Nakai's group has conducted important progresses towards an accurate description of the electron-nucleus correlation through the incorporation of ECG-type functions (i.e., the ECG-NOMO approach[32–34]). The basic difference between NOMO/HF and ECG-NOMO/HF implementations consists in replacing electronic GTFs with the origin on the nuclear orbital centers by explicit correlated GTF between the electronic and nuclear coordinates.[32] This way, short-range electron-nucleus correlation effects are effectively accounted for. Since the ECG-NOMO/HF method involves the self-consistent resolution of HF-type equations for electrons and nuclei, the conceptual simplicity of the original NOMO/HF implementation is preserved. The latest ECG-NOMO implementation[34] incorporates electronic correlation effects with the MP2 and CC approaches, revealing that the ECG-NOMO method outperforms its TRF-NOMO counterpart.[34]

Another major ENMO-type contribution is the so-called MCMO method (for recent revisions see Refs. 35 and 36). Actually, the origin of this method dates back to the (above mentioned) work by Nakai and collaborators.[23]

This article is copyrighted as indicated in the article. Reuse of AIP content is subject to the terms at: http://scitation.aip.org/termsconditions. Downloaded to IP: 147.122.21.18 On: Fri, 21 Nov 2014 17:47:01

Later, Tachikawa and Osamura applied it (then termed the dynamical extended MO method) to hydrogen and lithium hydride molecules.[37] One common characteristic of these contributions is the application of the *fully variational* (FV) treatment to optimize both exponents and center positions of the GTFs (and thus termed the FVMO approach[23,38,39]). Next, Tachikawa was independently involved in further applications[40] and developments[41] of the MCMO method (see Figure 1). This way, the MCMO method approach was extended to incorporate many-body correlation effects with the FCI[41] and MP2 approaches.[42] The highest accurate MCMO method, however, was developed by adopting the TRF formalism from Nakai *et al.*[28] (see above) with the many-body correlation described at FCI level.[43] Hereafter, this approach will be referred to as the FCI *fully variational* MO method.

Parallel computational and methodological developments have been carried out by Hammes-Schiffer's group over the last ten years,[44] with their ENMO-type method termed the NEO approach, which is implemented in the GAMESS suite of programs.[45] Starting with the HF approximation for both electrons and nuclei,[44,46,47] their current implementation allows to include the electron-nuclear correlation either with explicitly correlated Gaussians (the NEO-XCHF and NEO-XCHF2 versions[48,49]) or using variational and perturbative post-HF methods such as non-orthogonal CI (NOCI),[50] multi-configurational self-consistent field (MCSCF), and MP2 approaches.[51] Aimed to describe large molecular aggregates, multi-component density functional theory (DFT), first proposed by Parr *et al.*[52] in the earlier 1980s and later by Shigeta *et al.*[53] and Kreibich and Gross,[54] has been recently included in NOMO,[55,56] NEO,[57] and MCMO[58] implementations. In particular, the Colle-Salvetti functional,[59] originally designed to account for the short-range correlation between the electrons, was extended by Nakai's group[55,56] to describe electron-nucleus correlation effects.

More recently, the any particle molecular orbital APMO code[60–64] was developed. Restricted HF (RHF) equations were implemented in the original code[60] which was further extended to include inter-particle correlations at MP2 level,[61] and to remove the translational contamination at HF level.[65] The main novelty of the APMO implementation lies in its capability of describing systems containing any combination of quantum species (e.g., different isotopes), allowing to deal with exotic species such as positronic and muonic molecules and atoms.[65] Further extensions with the PARAKATA code[66] (the LOWDIN package[67]) allow to describe the quantum particles with the unrestricted-HF approximation and using either DFT or auxiliary perturbation theory (ADPT), and to carry out calculations with electron propagator theory (EPT).[68]

In this paper, we present the first applications of the APMO-MOLPRO interface. Our main goal is to include NQE into standard highly correlated electronic structure calculations using the general-purpose MOLPRO package of programs.[69] The MOLPRO code has a rich tool-box of methodologies to accurately describe both multi-reference or open-shell cases and systems where dynamic correlation effects play an important role. The APMO-MOLPRO implementation enables to perform regular calculations with MOLPRO considering the lightest nuclei as quantum particles, described at RHF level of theory through the APMO code. This implementation is applied to three types of systems: the $^4He_2$ dimer, $[He–H–He]^+$, $[He–D–He]^+$, and $[He–T–He]^+$ isotopomers, and molecular hydrogen along with its isotopomers.

The $^4He_2$ dimer has been chosen as a prototype dispersion-dominated weakly bound system with a van der Waals interaction. We wish to stress that our aim is not to question the validity of the BO approximation in these systems neither the spectroscopic accuracy reached in BO-based studies but to explore whether the incorporation of nuclear quantum effects directly in the electronic structure calculations may speed up the convergence with respect to the level of theory. This issue is worth considering because the accurate description of weakly bound systems at *ab initio* level with post-HF methods (e.g., the coupled-cluster approach) faces the problem of the slow convergence with both the one-electron basis set size and the level of the many-body electron correlation treatment. When applied to dimers of noble gases (see, e.g., Ref. 70 for an extensive analysis), explicitly correlated coupled-cluster methods certainly accelerates the convergence but the improvement is more moderate than that found in other systems. On the other hand, not only the calculation of the potential energy surfaces is challenging but also that of the molecular energy levels and, then, the spectra. We can number the following reasons: (1) the Fermi-Dirac (Bose-Einstein) statistics of the lightest nuclei; (2) their wide (highly anharmonic) amplitude motions; and (3) both the weakly attractive (long-range) and the strongly repulsive (short-range) interaction. The FCI-NO approach was designed to deal with these three problems, showing that the hard-core wall present in the potential energy curves amplifies the short-range nuclear dynamic correlation effects and, therefore, very large nuclear basis sets are necessary to get accurate rotational-vibrational energy levels. Hence, the central question is whether numerical implementations that describes the lightest nuclei and electrons simultaneously could be more efficient, with respect to the level of approximation, in computational spectroscopy of weakly bound systems. Although it is not possible to answer this question in general terms, it is worthwhile to carry out numerical tests, as we will show below.

A second application considers $[He–H–He]^+$ and its isotopomers as weakly bound hydrogen-bonded model systems where the strength of the interaction is intermediate between that of van der Waals and hydrogen bonding. First, we investigate the nuclear basis set convergence of total energies. We have found an important correlation between isotope mass and nuclear density localization. Third, a connection between ENMO- and BO-based pictures is shown by correlating the different density profiles of H, D, and T nuclei with the isotope-mass influence into zero point energies. Finally, the ENMO implementation is applied to molecular hydrogen and its isotopomers with the main objective of comparing with previous results on the same system.

The paper is structured as follows. Section II outlines the methodological approach with the emphasis on the strategy adopted to design the computational APMO-MOLPRO

This article is copyrighted as indicated in the article. Reuse of AIP content is subject to the terms at: http://scitation.aip.org/termsconditions. Downloaded to IP: 147.122.21.18 On: Fri, 21 Nov 2014 17:47:01

implementation. Section III presents its application to the above mentioned systems. Section IV closes with a summary and points out possible directions for future applications and extensions.

II. METHODOLOGICAL BACKGROUND

To unify the notations, we first outline the expressions used in a conventional electronic structure calculation at HF level of theory. Considering the particular case of a closed-shell molecule with $\mathcal{N}$ nuclei and N electrons (denoted as e), the RHF wave-function is expressed using Fock space (occupation-number) representation as

$$|\Phi^e\rangle = |n_1 \cdots n_i \cdots n_M\rangle, \tag{1}$$

where M is the total number of spin-orbitals and the occupation number n_i is 1 for N spin orbitals and zero otherwise. The (double occupied) spatial molecular orbitals are constrained to be orthonormal to each other, and can be written as a linear combination of N_{bf} (non-orthonormal) GTFs,

$$\psi_i(\mathbf{r}^e) = \sum_{\mu=1}^{N_{\text{bf}}} C_{\mu i}\chi_\mu(\mathbf{r}^e) \tag{2}$$

with $\mathbf{r}^e$ collectively designating the spatial coordinates of the electrons. The GTFs can be expressed as

$$\begin{aligned}\chi_\mu(\mathbf{r}^e) \propto (x^e - X^\mu)^{l_\mu}(y^e - Y^\mu)^{m_\mu}(z^e - Z^\mu)^{n_\mu} \\ \times \{\exp(-\alpha_\mu(r^e - R^\mu)^2)\},\end{aligned} \tag{3}$$

where $\mathbf{R}^\mu = \{X^\mu, Y^\mu, Z^\mu\}$ specify the coordinates at which the GTFs are centered (the fixed nuclear positions in conventional electronic structure calculations). Since only Cartesian GTFs are implemented within the APMO code, we used also Cartesian GTFs in the MOLPRO electronic structure calculations.

The HF equations can be written in matrix form as

$$\mathbf{FC} = \mathbf{SC}\epsilon \quad \therefore \quad \mathbf{F} = \mathbf{K} + \mathbf{I} + \frac{1}{2}\mathbf{G}, \tag{4}$$

where $\mathbf{K}$, $\mathbf{I}$, and $\mathbf{G}$ are the matrix representations of the electronic kinetic energy, the electron-nuclear attraction, and the electron-electron repulsion, respectively. Explicitly,

$$\begin{aligned}K_{\mu\nu} &= \int \chi_\mu^*(\mathbf{r}^e)\left[-\frac{1}{2}\nabla^2(\mathbf{r}^e)\right]\chi_\nu(\mathbf{r}^e)\,d\mathbf{r}^e, \\ I_{\mu\nu} &= \sum_{\gamma\in\mathcal{N}}\int \chi_\mu^*(\mathbf{r}^e)\left[\frac{Z_\gamma}{|\mathbf{r}^e - \mathbf{r}^\gamma|}\right]\chi_\nu(\mathbf{r}^e)\,d\mathbf{r}^e, \\ G_{\mu\nu} &= \sum_{\lambda,\sigma=1}^{N_{\text{bf}}} P_{\lambda\sigma}\left[(\chi_\mu\chi_\nu\,|\,\chi_\lambda\chi_\sigma) - \frac{1}{2}(\chi_\mu\chi_\sigma\,|\,\chi_\lambda\chi_\nu)\right],\end{aligned} \tag{5}$$

where $\mathbf{P}$ is the first-order reduced density matrix (1-RDM),

$$P_{\mu\nu} = 2\sum_{k=1}^{N/2} c_{\mu k}^* c_{\nu k}. \tag{6}$$

The electronic energy is then written as

$$E_e = tr\left[\mathbf{P}\left(\mathbf{K} + \mathbf{I} + \frac{1}{2}\mathbf{G}\right)\right] + \sum_{I,J\in\mathcal{N}}\frac{Z_I Z_J}{|\mathbf{r}_I - \mathbf{r}_J|}. \tag{7}$$

In a more general case, the molecular system can be divided into the set formed by quantum particles $\mathcal{Q}$ (i.e., the electrons and light nuclei) and the set composed by classical particles $\mathcal{C}$ (e.g., the heavy nuclei). Hereafter, the superscripts α and β will denote different quantum particles. The total wave-function associated with the set $\mathcal{Q}$ can be approximated as a product of the single configuration-state-functions associated with each quantum type,

$$\Psi(\{\mathbf{r}^\alpha\},\{\mathbf{r}^\beta\},\cdots) = \Phi^\alpha(\{\mathbf{r}^\alpha\})\cdot\Phi^\beta(\{\mathbf{r}^\beta\})\cdot\cdot\alpha,\beta\in\mathcal{Q}.$$

For quantum nuclei, we consider a single configuration-state-function where each quantum nucleus is constrained to occupy a different spatial orbital (it corresponds to the highest total spin configuration for nuclei with non-zero spin), using the occupation-number representation,

$$|\Phi^\alpha\rangle = \left|n_1^\alpha \cdots n_i^\alpha \cdots n_{M^\alpha}^\alpha\right\rangle, \tag{8}$$

where M^α is the number of (spin) orbitals defining the Hilbert space of the quantum particle with index α, and n_i^α is either 0 or 1 for quantum nuclei. It should be noticed that this condition is imposed because of the lack of nuclear correlation within the current implementation.

The molecular orbital of any quantum particle ψ^α is expressed as a linear combination of GTFs,

$$\psi_i^\alpha(\mathbf{r}^\alpha) = \sum_{\mu=1}^{N_{\text{bf}}^\alpha} C_{\mu i}^\alpha\chi_\mu^\alpha(\mathbf{r}^\alpha). \tag{9}$$

The matrix expression of the HF equation associated with each quantum particle α reads

$$\begin{aligned}\mathbf{F}^\alpha\mathbf{C}^\alpha &= \mathbf{S}^\alpha\mathbf{C}^\alpha\epsilon^\alpha \\ \mathbf{F}^\alpha &= \mathbf{K}^\alpha + \mathbf{I}^\alpha + \mathcal{J}^\alpha + \frac{1}{\eta^\alpha}\mathbf{G}^\alpha,\end{aligned} \tag{10}$$

where the average interaction between α and the other quantum species (β) is given by the term $\mathcal{J}^\alpha$. Explicitly, the matrix elements may be written as

$$\begin{aligned}K_{\mu\nu}^\alpha &= \int \chi_\mu^{\alpha*}(\mathbf{r}^\alpha)\left[-\frac{1}{2M_\alpha}\nabla^2(\mathbf{r}^\alpha)\right]\chi_\nu^\alpha(\mathbf{r}^\alpha)\,d\mathbf{r}^\alpha, \\ I_{\mu\nu}^\alpha &= \sum_{\gamma\in\mathcal{C}}\int \chi_\mu^{\alpha*}(\mathbf{r}^\alpha)\left[\frac{Z_\alpha Z_\gamma}{|\mathbf{r}^\alpha - \mathbf{r}^\gamma|}\right]\chi_\nu^\alpha(\mathbf{r}^\alpha)\,d\mathbf{r}^\alpha, \\ \mathcal{J}_{\mu\nu}^\alpha &= \sum_{\alpha\neq\beta}\sum_{\lambda,\sigma=1}^{N_{\text{bf}}^\beta} P_{\lambda\sigma}^\beta\left(\chi_\mu^\alpha\chi_\nu^\alpha\middle|\chi_\lambda^\beta\chi_\sigma^\beta\right), \\ G_{\mu\nu}^\alpha &= \sum_{\lambda,\sigma=1}^{N_{\text{bf}}^\alpha} P_{\lambda\sigma}^\alpha\left[\left(\chi_\mu^\alpha\chi_\nu^\alpha\middle|\chi_\lambda^\alpha\chi_\sigma^\alpha\right) \pm \frac{1}{\eta^\alpha}(\chi_\mu^\alpha\chi_\sigma^\alpha|\chi_\lambda^\alpha\chi_\nu^\alpha)\right].\end{aligned} \tag{11}$$

This article is copyrighted as indicated in the article. Reuse of AIP content is subject to the terms at: http://scitation.aip.org/termsconditions. Downloaded to IP: 147.122.21.18 On: Fri, 21 Nov 2014 17:47:01

Here, M_α denotes the mass of the quantum particle with index α and the sign $\pm$ corresponds to the bosonic/fermionic nature of this particle. η_α defines the occupation number of a given spatial orbital (i.e., $\eta_\alpha = 1$ for the quantum nuclei considered here) so that the 1-RDM takes the form

$$P^\alpha_{\mu\nu} = \eta^\alpha \sum_{k=1}^{N_{\rm occ}} c^{\alpha *}_{\mu k} c^\alpha_{\nu k}. \tag{12}$$

In the following, we consider molecular systems composed by only one class of quantum nuclei (denoted as n) with charge $+Z_n e$ and mass M_n; then N_n refers to the number of quantum nuclei. A practical calculation starts with the solution of Eq. (4) for the electrons considering both classical and quantum nuclei as fixed point charges within the BO approximation. Next, the electronic 1-RDM, $\mathbf{P}^e$, is employed to calculate the term that couples electronic and nuclear densities $\mathcal{J}^n$, see Eq. (11). Equation (10) is then solved for the quantum nuclei, and the whole process is iterated until convergence. The total energy of the *pseudo*-system composed by quantum particles, that further serves as an effective potential for the classical nuclei, can be written as

$$E = \sum_{\alpha\in\mathcal{Q}} \mathrm{tr}[\mathbf{P}^\alpha \mathbf{F}^\alpha] + \sum_{\gamma,\rho\in\mathcal{C}} \frac{Z_\gamma Z_\rho}{|\mathbf{r}^\gamma - \mathbf{r}^\rho|}, \tag{13}$$

and the electronic energy is conveniently defined as

$$E_e = \mathrm{tr}\left[\mathbf{P}^e\left(\mathbf{K}^e + \mathbf{I}^e + \mathcal{J}^e + \frac{1}{2}\mathbf{G}^e\right)\right] \tag{14a}$$

$$+\mathrm{tr}\left[\mathbf{P}^n\left(\mathbf{I}^n + \frac{1}{\eta^n}\mathbf{G}^n\right)\right] \tag{14b}$$

$$+\frac{1}{2}\left[\mathrm{tr}(\mathbf{P}^n\mathcal{J}^n) - \mathrm{tr}(\mathbf{P}^e\mathcal{J}^e)\right] \tag{14c}$$

$$+\sum_{\gamma,\rho\in\mathcal{C}} \frac{Z_\gamma Z_\rho}{|\mathbf{r}^\gamma - \mathbf{r}^\rho|}, \tag{14d}$$

where the term (14c) is included to avoid the double-counting of the nuclear-electron interaction energy. Also, we notice that the nuclear kinetic energy term ($\mathrm{tr}[\mathbf{P}^n\mathbf{K}^n]$) is separated from the expression of the electronic energy. In the infinite-nuclear-mass limit, the terms $\mathbf{P}^\alpha\mathbf{I}^\alpha$ and $\frac{1}{2}\mathbf{P}^\alpha\mathbf{G}^\alpha$, become the Coulomb repulsion between classical nuclei

$$\begin{aligned}
\mathrm{tr}\left(\mathbf{P}^n\mathbf{I}^n\right) &\xrightarrow[M_n\to\infty]{} \sum_{I=1}^{\mathrm{N}_n}\sum_{\gamma\in\mathcal{C}} \frac{Z_n Z_\gamma}{|\mathbf{r}^n_I - \mathbf{r}_\gamma|}, \\
\frac{1}{\eta^n}\mathrm{tr}\left(\mathbf{P}^n\mathbf{G}^n\right) &\xrightarrow[M_n\to\infty]{} \sum_{I=1}^{\mathrm{N}_n-1}\sum_{J=I}^{\mathrm{N}_n} \frac{Z_n Z_n}{|\mathbf{r}^n_I - \mathbf{r}^n_J|}.
\end{aligned} \tag{15}$$

Similarly, the expression for the electronic energy becomes identical to that in standard electronic structure calculations. It is important to realize that the electronic energy, as defined in Eq. (14), allows to get an effective *potential energy surface* (i.e., the electronic energy as a function of the relative positions between the nuclear GTFs centers). The electronic energy thus represents the expectation value of the full Hamiltonian minus the nuclear kinetic energy, as in standard BO calculations. Typically, an ENMO-type calculation starts with the centers of the nuclear GTFs at the fixed nuclear positions in preliminary BO calculations.

By comparing Eqs. (7) and (14), it is clear that we can make the following mappings:

$$\begin{aligned}
\mathbf{K} &\Leftarrow \mathbf{K}^e, \\
\mathbf{G} &\Leftarrow \mathbf{G}^e, \\
\mathbf{I} &\Leftarrow \mathbf{I}^e + \mathcal{J}^e, \\
\sum_{I,J\in\mathcal{N}} \frac{Z_I Z_J}{r_{IJ}} &\Leftarrow \mathrm{tr}\left[\mathbf{P}^n\left(\mathbf{I}^n + \frac{1}{\eta^n}\mathbf{G}^n\right)\right] \\
&\quad + \frac{1}{2}[\mathrm{tr}(\mathbf{P}^n\mathcal{J}^n) - \mathrm{tr}(\mathbf{P}^e\mathcal{J}^e)] \\
&\quad + \sum_{\gamma,\rho\in\mathcal{C}} \frac{Z_\gamma Z_\rho}{|\mathbf{r}^\gamma - \mathbf{r}^\rho|}.
\end{aligned} \tag{16}$$

From these mappings, it follows that the bare Coulomb interaction between the electrons and the quantum nuclei is replaced by a dressed Coulomb interaction between the electrons and the quantum nuclear charge density, as given by the term $\mathcal{J}^e$. This is schematically illustrated in Figure 2. The nuclei are represented by a distribution $\rho(\mathbf{r}^n - \mathbf{R}^n)$ centered in the clamped nuclear positions from standard BO calculations, $\mathbf{R}^n$. Once again, in the infinite-nuclear-mass limit, the nuclear distribution tends to a delta-type function $\delta(\mathbf{R}^n)$, with the electronic energy (see Eq. (14)) having the same expression as in the BO approximation (see Eq. (7)). From the mappings in Eq. (16), it is clear that the inclusion of electronic correlation into the HF equations for the quantum nuclei can be accomplished by substituting the HF electronic 1-RDM by its correlated counterpart, obtained using the MOLPRO code. Next, this correlated density matrix is introduced into the

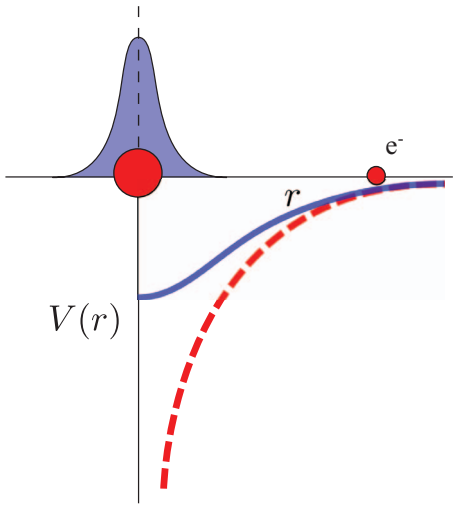

FIG. 2. Schematic illustration of the electrostatic interaction $V(r)$ among a reference electron (highlighted with a small circle) and a nucleus represented as either a fixed point charge within the BO approximation (highlighted with a large circle) or a Gaussian charge distribution with its center located at the position of the fixed nucleus in BO calculations.

This article is copyrighted as indicated in the article. Reuse of AIP content is subject to the terms at: http://scitation.aip.org/termsconditions. Downloaded to IP: 147.122.21.18 On: Fri, 21 Nov 2014 17:47:01

coupling term $\mathcal{J}^{\alpha}$ from Eq. (11). The APMO code is then run to solve the Fock equations associated with the quantum nuclei, obtaining a new nuclear charge density. Correlated electronic-structure-like calculations with MOLPRO and HF calculations with APMO are then iterated to achieve self-consistency. The full details of the computational APMO-MOLPRO implementation are available upon request to the authors.

III. APPLICATIONS

We first apply the APMO-MOLPRO implementation to the $^4He_2$ dimer which is a prototype of a weakly bound system. A second application deals with the $[He–H–He]^+$, $[He–D–He]^+$, and $[He–T–He]^+$ isotopomers as a model where the strength of the interaction is intermediate between that of van der Waals and hydrogen bonding systems. Finally, the molecular hydrogen and its isotopomers are considered.

A. A model of weakly interacting system: The $^4He_2$ dimer

Our calculations were performed using the singly augmented version of the correlation-consistent polarized aug-cc-pVQZ basis set (referred to as AVQZ) developed by Dunning and collaborators[71,72] for the electrons and a $2s2p$ basis set for the nuclei. The CC singles and doubles, and noniterative triples [CCSD(T)] method was applied with an integral threshold of 10^{-14} a.u. We followed the counterpoise (CP) procedure proposed by Boys and Bernardi[73] to account for the intramolecular basis set superposition error (BSSE) for both electrons and nuclei. For comparison, additional standard electronic structure CCSD(T) calculations with the double diffusely augmented d-aug-cc-pV6Z basis set (DAV6Z) were also performed. The nuclear basis set was calibrated through the gradual addition and optimization of exponent of s and p GTFs following the sequence $1s \rightarrow 2s \rightarrow 2s\ 1p \rightarrow 2s\ 2p$. Each exponent optimization step involved a simultaneous geometry optimization. The simplex algorithm was used for the exponents optimization with an accuracy threshold of 10^{-6} a.u. As a final step, a global re-optimization of all the exponents α and the geometry was performed. This procedure resulted in the following values for the optimized exponents: 171.9559 ($1s$), 216.0468 ($2s$), 238.0624 ($1p$), and 250.0442 ($2p$).

Fixing the He–He internuclear distance, we started with a standard CCSD(T) calculation with MOLPRO (i.e., clamping the He nuclei). Next, the electronic CCSD 1-RDM was used to calculate the nuclear-electronic coupling matrix $\mathcal{J}^{n}$ (see Eq. (11)) and the Fock equation associated with the nuclei and including the mean-field generated by the electronic charge density, was solved with the APMO code, with the centers of the nuclear GTFs kept fixed at the positions of the clamped nuclei in the preliminary BO calculations. This was followed by a CCSD(T) calculation for the electrons with MOLPRO including the NQE through the nuclear HF 1-RDM. CCSD(T) and HF calculations for the electrons and the nuclei were then run iteratively until self-consistency. This procedure is repeated for different distances between the nuclear GTFs centers. Figure 3 shows the resulting effective potential energy curve (PEC) (highlighted in red). For the sake of clarity, Table I summarizes the main results (well-depths and minimum energy positions).

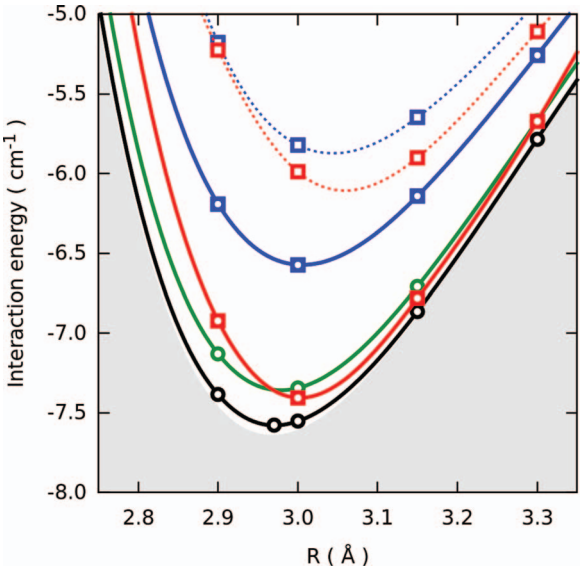

FIG. 3. $^4He_2$ dimer potential energy curves. APMO-MOLPRO CCSD(T){CCSD}/AVQZ:2s2p (red solid line); MOLPRO CCSD(T)/AVQZ (blue solid line); MOLPRO CCSD(T)/DAV6Z (green); MOLPRO FCI/DAV6Z (black) from Ref. 77. The reference potential energy curve from Ref. 74 is shown as a shaded area. The CCSD entry in APMO-MOLPRO CCSD(T){CCSD}/AVQZ indicates that only the CCSD correlated 1-RDM has been employed into the HF equations for the nuclei. APMO-MOLPRO CCSD(T){CCSD}/AVTZ:2s2p (red dashed line) and MOLPRO CCSD(T)/AVTZ (blue dashed line) results are also shown.

Naturally, a rigorous non-BO calculation would provide directly the energy D_0 and wave-function of the $^4He_2$ weakly bound state that have been experimentally observed (i.e., without relying on a PEC). Due to the highly delocalized nature of this state ($\langle R \rangle$ 47.1 ± 0.5 Å from Ref. 74), however, a much larger nuclear basis set would be necessary to carry out such calculations, along with the separation of the center-of-mass operator from the molecular Hamiltonian and the inclusion of the electron-nuclear correlation. Extremely accurate estimations of D_0 or $\langle R \rangle$ values have been very recently provided by Cencek *et al.* (see Ref. 74) by calculating the nuclear wave-function supported by the helium dimer potential. This PEC was obtained through very accurate BO calculations including post-BO adiabatic and relativistic corrections as well as quantum electrodynamic effects. Here, by computing an effective helium dimer potential, we adopt an approach

TABLE I. Well-depths (E^{int}_{min}) and minimum energy positions (R_{min}) of the $^4He_2$ dimer potential energy curves shown in Fig. 3.

	R_{min}(Å)	E^{int}_{min}(cm^{-1})
AVTZ: BO/ENMO	3.04/3.06	−5.8729/−6.1065
AVQZ: BO/ENMO	3.00/3.00	−6.5727/−7.4054
DAV6Z(BO):[a] CCSD(T)/FCI	2.98/2.97	−7.3580/−7.5785
Reference 74	2.97	−7.6429

[a]Reference 77.

This article is copyrighted as indicated in the article. Reuse of AIP content is subject to the terms at: http://scitation.aip.org/termsconditions. Downloaded to IP: 147.122.21.18 On: Fri, 21 Nov 2014 17:47:01

which is somewhat different from other applications within the ENMO framework. As already mentioned, our goal is to estimate if the inclusion of quantum nuclear effects would affect the level of theory required to correctly account for dynamic correlation in electronic structure calculations, and, more particularly, the flexibility of the orbital space for an adequate description of the dispersive interaction. Our interpretation follows the lines of BO method using floating Gaussian orbitals,[75,76] with the electrostatic attractive field generated by vibrating nuclei as the guiding function for the electronic orbitals, see also below.

In Figure 3, the APMO-MOLPRO CCSD(T) PEC (solid red line) is compared with standard CCSD(T) electronic structure calculations using the same (AVQZ) electronic basis set (solid blue line) or the much larger DAV6Z basis set (highlighted in green). The most accurate PEC from Ref. 74 is also shown as a shaded area. For comparison purposes, the FCI potential obtained using the DAV6Z basis set from Ref. 77 is also displayed (black line). This FCI potential provides a bound state for the ^{4}He dimer that disappears when its depth-well is reduced by a mere 0.02% (e.g., the FCI PEC with the AVQZ basis fails to provide a bound helium dimer state). Although this FCI potential is very close to the reference potential from Ref. 74, the associated D_0 value is about 0.5 mK above the best estimation at present ($D_0 = 1.62 \pm 0.03$ mK from Ref. 74).

Let us now compare our ENMO results to those obtained from standard electronic structure calculations. From Figure 3, it can be noticed that the APMO-MOLPRO CCSD(T) potential with the AVQZ basis set is very close to that obtained through standard CCSD(T) calculations using the much larger DAV6Z basis set (110 vs. 476 Cartesian GTFs). In contrast, the well-depth of the potential from conventional CCSD(T) calculation with the AVQZ basis set is 0.83 cm^{-1} higher (see Table I). This result demonstrates that the inclusion of NQE allows to effectively reduce the electronic basis set size. This can be understood by considering that the Kato's (electron-nuclear) cusp condition[78] becomes somehow smoothed out when a fixed point charge is replaced by a finite nuclear charge distribution (see Figure 2), taking away the divergence of the electron-nucleus Coulomb potential as $-Z/r$ when r goes to zero. On the other hand, when using Gaussian-type orbitals whose gradient is zero at the origin, the Kato's cusp condition is not satisfied.[79] Moreover, it seems clear that the nuclear charge distribution shown in Figure 2 is capable to push electronic density out into regions associated with the dispersive interaction, thus relaxing the strong requirements for the GTFs (intrinsically unable to properly describe the electron-electron cusp also) basis set size. In other words, as the He nuclei approach each other, their associated electronic clouds become more diffuse and interactive, increasing the dispersive effect. On the contrary, a fixed point charge attracts more electronic density to its position. The electronic orbitals become thus effectively more flexible in the scenario of a vibrating nucleus. These arguments are similar to those presented in Ref. 76 to explain the reasons why Diffusion Monte Carlo (DMC) calculations with floating spherical GTFs in the guiding function provide better results than their standard GTFs-type counterparts. On the other hand, ENMO calculations with the quantum nuclei described through relatively narrow amplitude GTFs could be phenomenologically identified with standard BO calculations using floating electronic orbitals.[76] Thus, the most important insight that can be extracted from the consideration of finite-mass effects in a model system for the dispersion interaction is that the requirements for the electronic structure calculations are less stringent than in the infinite-nuclear-mass limit.

TABLE II. Interaction energy differences $\Delta\mathcal{E}$ (in cm^{-1}) between APMO-MOLPRO CCSD(T){CCSD}/AVQZ:2s2p and MOLPRO CCSD(T)/AVQZ calculations (second column) as a function of the distance between GTFs nuclear centers R_{He-He}, in Å (first column). Third column: Diagonal adiabatic correction $V_{ad,int}^{corr}$ (in cm^{-1}) for $^4He_2$ as a function of the He–He inter-nuclear distance R_{He-He}, in Å.

R_{He-He} (Å)	$\Delta\mathcal{E}$ (cm^{-1})	$V_{ad,int}^{corr}$ (cm^{-1})[a]
1.85	56.2514	0.2962
2.15	15.4504	0.0614
2.40	4.0442	0.0086
3.00	− 0.8331	− 0.0061
3.80	− 0.0441	− 0.0020

[a]Reference 74.

We notice that the interaction energy difference between BO- and ENMO-type calculations (see Table II) should not be confused with the diagonal adiabatic correction to the BO energies. This is apparent from the definition of the latter as the expectation value of the nuclear kinetic energy operator,[80]

$$V_{ad}^{corr} = \left\langle \Phi_{BO}^{e} \middle| -\sum_{I} \frac{\nabla_I^2}{2M_I} \Phi_{BO}^{e} \right\rangle, \tag{17}$$

and taking into account that the kinetic nuclear energy is subtracted to obtain the interaction energy within the ENMO framework. By construction, the term V_{ad}^{corr} is a finite-mass adiabatic correction to the electronic energy only, while the ENMO approach includes the influence of these finite-mass effects onto the electronic wave-function itself. As reported by Cenket *et al.*,[74] the inter-nuclear dependence of the finite-mass correction $V_{ad,int}^{corr}$ can be calculated by subtracting the corresponding (mass-polarization) term from two isolated helium atoms. Interaction energy differences between BO- and ENMO-type calculations are compared with reference $V_{ad,int}^{corr}$ values from Ref. 74 for a selected set of inter-nuclear distances. As can be seen from Table II, the energy difference obtained by the inclusion of finite-mass effects with the ENMO approach is more than two orders of magnitude larger than the adiabatic correction around the minimum of the potential energy curve. Both energy differences are positive at very short inter-nuclear distance, change their sign close to the minimum, and approach zero at large distances. Thus, the inclusion of finite-mass effects tends to stabilize the ^{4}He dimer, as expected.

So far, our goal has been the analysis of NQE for highly correlated electronic energies. Let us now focus on the nuclear response to these electronic correlation effects. For this purpose, Table III lists the nuclear relaxation energies $\Delta\mathcal{E}_{rex}^{nuc}$ obtained by replacing the HF electronic 1-RDM by its correlated counterpart, calculated with the CCSD approach. As apparent

This article is copyrighted as indicated in the article. Reuse of AIP content is subject to the terms at: http://scitation.aip.org/termsconditions. Downloaded to IP: 147.122.21.18 On: Fri, 21 Nov 2014 17:47:01

TABLE III. Nuclear relaxation energies $\Delta\mathcal{E}_{rex}^{nuc}$ (in cm^{-1}) as a function of the distance between GTFs nuclear centers, R_{He-He}, in Å (first column). Second (third) column: APMO-MOLPRO CCSD(T){CCSD}/AVTZ:2s2p (CCSD(T){CCSD}/AVQZ:2s2p) results.

	$\Delta\mathcal{E}_{rex}^{nuc}$ (cm^{-1})	
R_{He-He} (Å)	AVTZ	AVQZ
2.30	−1.1522	−1.1105
2.70	−0.7638	−0.7001
3.40	−0.1141	−0.0768
3.80	−0.0680	−0.0088

from this table, the nuclear response to the electronic correlation becomes increasingly more pronounced as the distance between GTFs nuclear centers decreases. Then, at distances shorter than 2.4 Å, the nuclear relaxation energy reaches values larger than -1.0 cm^{-1}, lowers to about -0.5 cm^{-1} close to the minimum, and approaches zero at 3.8 Å. From Table III, it can be also seen that the electronic AVQZ and AVTZ basis sets provide very similar values with nuclear relaxation energy differences below 0.07 cm^{-1}. Contrarily, electronic interaction energies obtained using BO- and ENMO-type calculations with the AVTZ basis set are fairly inaccurate (see Fig. 3 and Table I). The inclusion of NQE certainly improves the well-depth value calculated with the AVTZ basis as compared to the reference one[74] and the same general trends upon augmentation of the basis set size are found in both BO- and ENMO-type calculations. The current APMO-MOLPRO interface is implemented for up to *g*-type Gaussian functions, that corresponds to the VQZ-type basis for main group elements. Work is in progress to implement *h*- and *i*-type functions that will allow to use up to V6Z basis sets. Upon increasing the nuclear basis sets size, including electron-nuclear correlation, and separating the center-of-mass motion, a second regime would be eventually reached in which the inter-nuclear quantum mode itself is correctly described. Concerning the inclusion of short-range nuclear correlation effects, it has been shown through BO-based studies[6] with the FCI-NO approach that their proper description in doped ^{3}He clusters is crucial in getting physically meaningful results, as the pairing found for ^{3}He and the quasi-degeneracy of different nuclear spin-states. In turn, this quasi-degeneration renders the spectra of probe molecules inside ^{3}He very congested[3,81] at temperature for which spinless ^{4}He droplets are superfluid and the guest molecule spectrum displays sharp rotational lines. As already mentioned, very large one-particle basis sets and special diagonalization techniques are necessary to describe these short-range correlation effects with FCI-NO (BO-based) calculations[6] due to the sharply repulsive He–He potential at short distances that raises much more steeply compared to the Coulomb potential. As follows from present results, however, the requirements for the one-particle basis set and the many-particle correlation treatment are less demanding when nuclei and electrons are treated simultaneously. In any case, the inclusion of the nuclear correlation is necessary to relax the maximum spin condition for the nuclear (^{3}He) wave-function.

Summarizing, it is necessary to develop nuclear basis sets better tailored to describe the inter-nuclear motion in conjunction with the separation of the center-of-mass motion, and practical approaches to include the electron-nuclear correlation. For a diatomics like $^4He_2$, if the position of one nucleus is frozen (infinite-nuclear-mass limit), the mass of the second nucleus is fixed to the reduced mass, and the center of the second nucleus GTFs is also optimized, it would be possible to obtain an estimation of the zero point energy D_0, since the separation of the center-of-mass motion is already accounted for. In our case, this procedure leads to the lowering of the nuclear kinetic energy by about 0.03 a.u. Still, it is important to realize that one-centered GTFs are unable to account for the highly delocalized nature of the $^4He_2$ wave-function. For this purpose, it would be suitable to use multi-centered Gaussian functions adding nuclear *ghost* GTFs. This strategy is somehow reminiscent to the addition of midbond GTFs in the electronic basis sets to saturate the dispersion interaction. It also resembles the "distributed Gaussian functions" (DGF) method of Hamilton and Light[82] for solving multi-dimensional vibrational problems, as applied[83] to $^4He_2$ and $^4He_3$. Since the APMO implementation already enables the use of nuclear *ghost* GTFs, the problem would translate in designing efficient algorithms to distribute the GTFs centers. We notice that the DGF method was proposed to deal also with excited vibrational states.[82] Concerning the inclusion of the inter-particle correlation, the transcorrelated Hamiltonian approach[84] seems to be quite attractive. By using a single determinant (permanent) Jastrow *ansatz*, HF-like equations are obtained and, therefore, this approach seems to be well-suited to interfaces with standard electronic structure codes.

B. $[He–H–He]^+$ and its isotopomers

As a second application, we studied the $[He–H–He]^+$, $[He–D–He]^+$, and $[He–T–He]^+$ isotopomers. These are model systems in which the interaction strength is remarkably influenced by the nuclear delocalization of the central nucleus (i.e., H, D, or T). As in previous works within either the BO[85,86] or the ENMO frameworks,[49,61] a symmetric linear structure for the $[He–H–He]^+$ system was considered. The two lateral He nuclei were treated classically and the central nucleus was considered as a quantum particle. Specifically, the quantum nucleus was described with a 5*spd* basis set of GTFs, while the CCSD(T) method and the AVQZ basis set were employed for the electrons. The nuclear GTFs were located at the midpoint between the two He nuclei. Taking into account the small difference between the masses of hydrogen and helium nuclei, a rigorous non-BO calculation should treat both nuclei equivalently. However, we have chosen this approach as it allows for a direct comparison with results obtained earlier using similar methods.[49,61]

The exponents of the nuclear GTFs were obtained using an even-tempered set.[69] The same set of basis functions was employed for all isotopes. Following the strategy proposed by Nakai,[26] the exponents of nuclear GTFs with non-zero orbital angular momentum quantum numbers were set to the same values as for the *s*-type GTFs. Figure 4 shows the convergence

This article is copyrighted as indicated in the article. Reuse of AIP content is subject to the terms at: http://scitation.aip.org/termsconditions. Downloaded to IP: 147.122.21.18 On: Fri, 21 Nov 2014 17:47:01

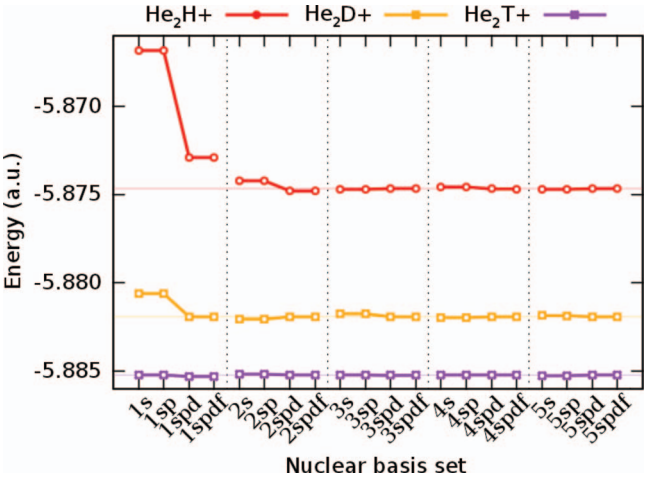

FIG. 4. Convergence of the total energy upon addition of nuclear GTFs for the $[He–H–He]^+$ system and its isotopomers.

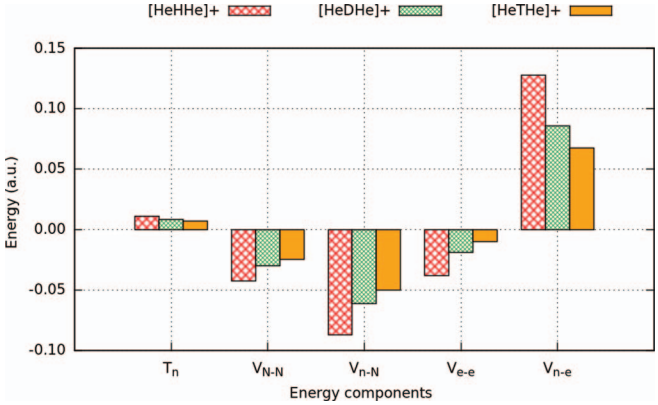

FIG. 5. Decomposition analysis of the energy terms associated with the $[He–H–He]^+$, $[He–D–He]^+$, and $[He–T–He]^+$ systems (see text).

of the total energies as a function of the number of primitive GTFs. These energies were obtained by fixing the He–He internuclear distance at the optimized value in standard CCSD(T) calculations. As a first step, the exponent of a single 1*s* GTF was optimized variationally for each isotope. The average exponents of the 1*spdf* GTFs in the even-tempered sets were set to these optimized values. When only one *s*-type function is employed, the three systems share the same nuclear density distributions. Therefore, the pronounced isotope mass dependence of the total energy (see Figure 4) comes directly from the $1/M_n$ term in the kinetic energy matrix (see Eq. (11)). The further addition of nuclear GTFs enables a differential localization of the nuclear densities depending on the isotope mass, reducing thus the total energy differences, see Figure 4. It is clearly apparent that a 5*spd* basis set suffices to get convergent total energy values for the three complexes.

As a second step, the geometry of the system was optimized using the 5*spd* basis set. The resulting total energy values were −5.8754, −5.8823, and −5.8855 a.u. for the $[He–H–He]^+$, $[He–D–He]^+$, and $[He–T–He]^+$ complexes, respectively. As expected from the higher level of theory adopted here, these energies are lower (∼0.04 a.u.) than those obtained with the APMO-MP2 method.[61] To gain further insight into isotope-dependent effects, we calculated the average values of the quantum nucleus kinetic energy T_n, the electronic repulsion V_{e-e}, the He–He repulsion V_{N-N}, the repulsion energy between the central nucleus and the classical He nuclei V_{n-N}, and the electron-central nucleus attraction V_{n-e}. The differences between the values obtained within the ENMO framework for the three systems and those resulting from standard CCSD(T) calculations for the $[He–H–He]^+$ complex are shown in Figure 5. Table IV lists the average internuclear distance $\langle R_{X-He}\rangle$ with the optimized molecular geometry, while the nuclear density distributions are displayed in Figure 6.

We observed isotope mass effects similar to those found in Ref. 61. They can be understood by considering: (1) the isotope mass increase from protium to tritium; (2) the concomitant localization of the nuclear densities (see Figure 6); and (3) the resulting compression of the electronic densities. Naturally, the nuclear kinetic energy increases if the isotope mass decreases, $1/M_n$ increases. Once again, as apparent from Figure 2, the most attractive electron-nuclear interaction corresponds to the infinite nuclear mass limit. Therefore, for heavier central nucleus, the average value of V_{n-e} is larger. On a contrary, the Coulomb repulsion between the central nucleus and the He nuclei is larger as the former becomes more localized (see the energy differences associated with the V_{n-N} component in Figure 5). Also, it can be noticed that the average V_{e-e} interaction becomes less repulsive as the central nucleus becomes more delocalized. As discussed above for the ^{4}He dimer, the electronic density is more sparse when a fixed point charge is replaced by a nuclear charge density, making their average interaction less repulsive. Considering the results presented in Table IV, we mention that the equilibrium He–H bond distance obtained with conventional electronic structure calculations (0.9249 Å from Table IV) agrees very well with previous calculations using highly correlated methods (i.e., 0.925 Å from Ref. 86), indicating that the electronic correlation is properly described. We can also notice from Table IV the shortening of the average internuclear distances $\langle R_{X-He}\rangle$ as the central nucleus becomes more localized, making the He–He interaction more repulsive (see Figure 5). On the other hand, the values of the Mulliken charges (see Table IV) are smaller than those obtained through a standard BO-based calculation, reflecting the delocalization of the electronic densities after the inclusion of finite-mass

TABLE IV. Average internuclear distances $\langle R_{X-He}\rangle$ (in Å), differences between $\langle R_{X-He}\rangle$ values obtained at HF and CCSD(T) levels of theory ($\Delta\langle R_{X-He}\rangle$, in Å), and Mulliken charges on the central nucleus (in a.u.) obtained for the $[He–X–He]^+$ isotopomers (i.e., X = H, D, and T) in the present work.

	$\langle R_{X-He}\rangle$ (Å)	$\Delta\langle R_{X-He}\rangle$ (Å)	Mulliken
	0.9608		0.387
$He–H–He^+$	0.9249[a]	0.0144[a]	0.635[a]
	0.9631[b]		
$He–D–He^+$	0.9498	0.0094	0.399
$He–T–He^+$	0.9451	0.0075	0.409

[a] Values obtained with conventional electronic structure calculations.
[b] APMO-MP2 value from Ref. 61.

This article is copyrighted as indicated in the article. Reuse of AIP content is subject to the terms at: http://scitation.aip.org/termsconditions. Downloaded to IP: 147.122.21.18 On: Fri, 21 Nov 2014 17:47:01

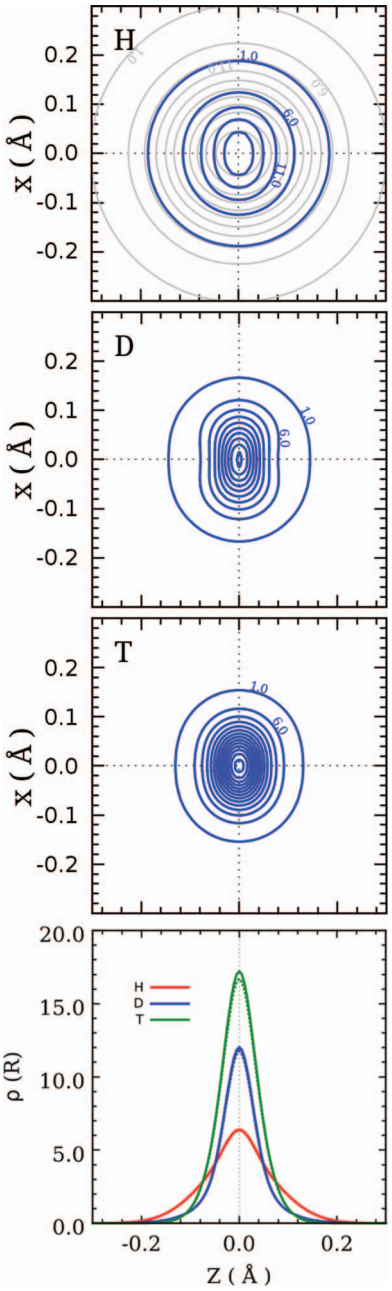

FIG. 6. Three top panels: Contour plots of the nuclear density distributions of $[He–X–He]^+$ for X = H, D, and T, on a plane containing the He–He internuclear axis (the z axis). The distances are given in Å. Adjacent contours are separated by 5.0 $Å.^{-2}$ A model spherical density distribution (grey color) has been superimposed to the protonic density in the $[He–H–He]^+$ system. Bottom panel: One-particle protonic density distributions, with the electrons described at either CCSD(T) (solid lines) or HF (dotted lines) levels of theory, calculated along the He–He internuclear axis of $[He–X–He]^+$ (with the origin located in the middle of the two He nuclei) for X = H, D, and T.

effects, as already discussed for the helium dimer. These effects become more pronounced as the nuclear mass decreases. Within standard BO-based theory, this is explained by considering the PES anharmonicity and the wider amplitude zero-point motions attained by the lightest isotopes (see, for example, Ref. 87). Within the ENMO approach, the latter trend is reflected in more delocalized nuclear densities as the nuclear mass decreases (see Figure 6). Interestingly, the protonic densities are rather isotropic in contrast to those attained by deuteron and triton nuclei, which are more confined in the direction of the internuclear He–He axis. In the standard BO-based picture, the heaviest tritium nuclear density shows the most anisotropic shape that adapts better to the anharmonic potential due to its smaller zero point energy. Physical insights into the system are thus gained directly with ENMO-type calculations before resorting to the quantum treatment of the nuclear motion on the electronic potential energy surface. The isotropic character of the protonic densities could be correlated with a quasi-degeneracy of zero point energies for asymmetric stretching and bending normal modes of the electronic ground state in standard BO-based calculations. Very similar energies for stretching and bending frequencies were found by Ko *et al.* in Ref. 49 using a single 1s GTF. The inclusion of GTFs with higher angular momentum quantum numbers in the present work enables a more balance description of stretching and bending modes. Also, previous works have shown that the vibro-rotational energy levels supported by the $[He–H–He]^+$ PES do not correspond to any particular mode but to a combination of them.[87] Focusing on the comparison with previous works using ENMO approaches, it can be noticed that our value for $\langle R_{X-He} \rangle$ is quite close to that obtained in Ref. 61 using the APMO-MP2 method (see Table IV). More significant differences are found, however, by comparing the protonic density distribution from the present work (see the bottom panel of Fig. 6) and that obtained using the NEO-XCHF2 method (see Fig. 1 from Ref. 49). Thus, the inclusion of the electron-nuclear correlation with the NEO-XCHF2 approach leads to a higher degree of delocalization for the protonic densities, as discussed in previous works for the same system.[49,61] On the contrary, as shown in the bottom panel of Fig. 6, nuclear density distributions at the equilibrium geometry obtained with the electrons described at HF and CCSD levels are almost indistinguishable. The equilibrium geometry itself, however, is affected by the nuclear response to the electronic correlation. This is clearly reflected in the isotope dependence of the differences between the $\langle R_{He\text{-}X} \rangle$ expectation values obtained at HF and CCSD(T) levels of theory, as shown in Table IV ($\Delta\langle R_{He\text{-}X} \rangle$ values). Thus, for protium, the enlargement of the average He–H distance at CCSD(T) level is about twice as larger than for tritium. The nuclear response to the electronic correlation is thus more pronounced for the lightest isotope, as expected.

C. Isotopomers of molecular hydrogen: Prototype model systems

The isotopomers of molecular hydrogen are prototype model systems to test the robustness of ENMO approaches and computational implementations[43,60] by virtue of their relative simplicity. The highly accurate non-BO calculations on these systems have been carried out by Adamowicz and collaborators[88–91] using an internal rotationally invariant molecular Hamiltonian and explicitly correlated GTFs, and including relativistic corrections to the resulting energies. These works thus provide reference values that can be used to test the accuracy of our results.

We have performed ENMO calculations applying a FCI (HF) treatment for the electrons (nuclei) of H_2, HD, HT,

This article is copyrighted as indicated in the article. Reuse of AIP content is subject to the terms at: http://scitation.aip.org/termsconditions. Downloaded to IP: 147.122.21.18 On: Fri, 21 Nov 2014 17:47:01

TABLE V. Average internuclear distances $\langle R_{n-n} \rangle$ (in Å) obtained for molecular hydrogen and its isotopomers.

	HF:HF[a]	HF:FCI[b]	Non-BO	Experimental[c]
H_2	0.7765	0.7628	0.7666[d]	0.7511
HD	0.7698	0.7602	0.7632[e]	0.7498
HT	0.7668	0.7599		0.7493
D_2	0.7632	0.7598	0.7591[f]	0.7484
DT	0.7603	0.7586		0.7476
T_2	0.7574	0.7585	0.7559[g]	0.7469

[a]Results using the HF approximations for both electrons and nuclei from Ref. 60.
[b]Results obtained in this work at HF (FCI) level of theory for the nuclei (the electrons).
[c]Values determined from experimental data.[92]
[d]Reference 88.
[e]Reference 89.
[f]Reference 90.
[g]Reference 91.

D_2, DT, and T_2. The nuclear GTFs were obtained using an even-tempered procedure, as outlined in the case of the $[He–H–He]^+$ complex above. Specifically, we employed a 5*spd*/AVQZ basis set for nuclei/electrons. Table V presents the average internuclear distances $\langle R_{n-n} \rangle$ in Å. Experimental,[92] high accurate non-BO results from Adamowicz and collaborators,[88–91] and ENMO results using a HF approach (referred to as HF:HF) for both electrons and nuclei with the APMO code[60] are also displayed. Electronic and nuclear density contours of the HT isotopomer are shown in Figure 7.

By comparing the average $\langle R_{n-n} \rangle$ values for the different isotopes, both experimental and obtained from highly accurate non-BO calculations, it is clear that the heavier the nuclear mass, the shorter the average internuclear distance. This can be understood by considering that the widest amplitude motion, accomplished by the lightest nuclei (i.e., protons), is associated with the highest delocalized nuclear density (see also Figure 7). This trend is well reproduced by both ENMO computations, while the inclusion of the electronic correlation through the FCI approach quantitatively improves the average $\langle R_{n-n} \rangle$ values, as compared to those obtained with highly accurate non-BO methods,[88–91] and estimated from experimental measurements.[92] On the other hand, the incorporation of electronic correlation through BO-based FCI calculations causes an increase of the H–H distance from 0.7326 and 0.7419 Å, indicating that the differences between HF:HF and HF:FCI results with the ENMO approach arise not only from the electronic correlation but also from the corresponding nuclear response. As in the helium dimer case, nuclear relaxation energies reach significant values at short internuclear distances only (see Table III), inducing smaller values of the $\langle R_{n-n} \rangle$ when electronic correlation effects are included. As expected, the shortening of the average $\langle R_{n-n} \rangle$ distances becomes more marked as the isotope mass decreases (see Table V). The isotope dependence of the response to the electronic correlation is also clearly apparent by comparing the electronic densities obtained at CCSD(T) and HF levels of theory (see Figure 7): the differences between CCSD(T) (red lines) and HF (grey lines) density contours are more pronounced around the lightest quantum nucleus, becoming almost indistinguishable at the infinite nuclear limit. This shows

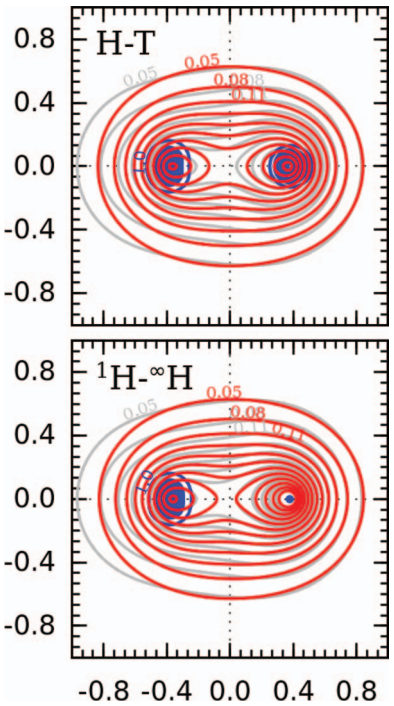

FIG. 7. Contour plots of the electronic (highlighted in red) and nuclear (highlighted in blue) densities on a plane containing the internuclear axis (in Å units). Electronic density distributions obtained at HF level of theory (grey color) have been superimposed. (Upper panel) molecular HT. (Lower panel) H_2 at the infinite nuclear limit for one of the hydrogen nuclei (denoted as $^\infty H_2$). Adjacent contours are separated by 0.03 a.u.

the importance of including the electronic correlation effects in the quantum treatment of the lightest nuclei.

Focusing on the electronic densities shown in Figure 7 for molecular HT, it can be noticed that the electronic cloud around the lightest isotope becomes more dispersed. On a contrary, the electronic charge tends to concentrate more at nuclear-rich regions as the isotope mass increases. This is further clarified in the infinite-nuclear mass limit for one of the hydrogen atoms (see the bottom panel of Figure 7). As discussed above for the helium dimer, this can be explained by comparing bare and dressed *e-n* Coulomb interactions in Figure 2: the bare Coulomb interaction, corresponding to the infinite-nuclear mass limit, is capable of attracting more electronic density into the nucleus position. Naturally, this is reflected in molecular dipole moment μ values. This property has been experimentally determined for heteronuclear HD by Nelson and Tabisz,[93] providing a value in the range 0.8–1.0 mD. This value is overestimated by a factor of 28 by our HF:FCI calculations which is similar to factor of 30 obtained from earlier HF:HF calculations.[60] As extensively discussed by Ishimoto *et al.*,[43] the inclusion of electron-nuclear correlation is very important to obtain μ values in good agreement with the experimental measurements. In fact, by resorting to the FCI *fully variational* MO method (see Sec. I), they provided a value of the HD dipole moment of 0.85 mD in excellent agreement with the experimental measurements. Similar to the $[He-H-He]^+$ system, electron-nuclear correlation effects result in more delocalized nuclear density distributions. Therefore, the electronic density becomes even more

This article is copyrighted as indicated in the article. Reuse of AIP content is subject to the terms at: http://scitation.aip.org/termsconditions. Downloaded to IP: 147.122.21.18 On: Fri, 21 Nov 2014 17:47:01

dispersed floating out from the classical nuclei positions and providing smaller μ values. Accurate results have been also given by Adamowicz and collaborators in Ref. 17 (for example, $\mu = 0.83$ mD for HD). The nuclear mass dependence of these values is already qualitatively captured in our calculations (μ(HT) > μ(HD) > μ(DT)). However, the poor quantitative agreement for the μ values indicates the importance of adopting higher levels of theory to describe this property. As already mentioned, the separation of the center-of-mass motion can be emulated by freezing the position of one nucleus and replacing the mass of the second nucleus by the molecular reduced mass. This numerical test has been carried out for the HD molecule resulting in the lowering of the nuclear kinetic energy by more than 0.02 a.u. Still, the electron-nuclear correlation must be included to provide more accurate values of diatomic non-BO energies. Moreover, it should be stressed that at present the APMO-MOLPRO interface allows to handle only maximum spin states for the nuclei with non-zero spin. Therefore, our results on H_2 correspond to the *ortho*-H_2 spin isomer. The experimental measurements, however, usually involve a mixture of *ortho*- and *para*-H_2 spin isomers.

IV. CONCLUDING REMARKS AND FUTURE PROSPECTS

We report the application of the APMO-MOLPRO interface to three model systems. This computational implementation allows to incorporate nuclear quantum effects at HF level into highly correlated electronic structure calculations carried out with the MOLPRO package.[69] On the other hand, the APMO-MOLPRO interface extends the capabilities of the APMO code by allowing not only to include the electronic correlation but also an efficient optimization of either the nuclear basis set or the molecular geometry. The APMO-MOLPRO implementation is designed in a way that MOLPRO calculations can be performed with an internal call to the APMO code.

To model a weakly interacting system, we have chosen an effective potential for the dimer $^4He_2$ with the bare electronic-nuclear Coulomb interaction replaced by a dressed interaction, substituting the point charges of classical nuclei by corresponding finite nuclear charge distributions. Our results indicate that the requirements for the electronic basis set size and the many-particle correlation treatment become less demanding when electron and nuclei are described simultaneously. This result is interpreted on the basis of *ab initio* calculations using *floating* electronic orbitals, and the relaxation of the cusp conditions upon replacing the bare Coulomb interaction by that obtained after including finite-mass effects. In a future, the distributed Gaussian functions method of Hamilton and Light[82] could be adapted to deal with vibrational ground and excited states of weakly bound systems in ENMO-type implementations.

As a second test case, the APMO-MOLPRO interface has been applied to the $[He–H–He]^+$ molecule and its isotopomers. As reported in previous ENMO studies on the same system,[61] the de-localization degree of the nuclear density is found to be strongly correlated with the nuclear mass. Thus, proton density is isotropic and much more delocalized compared to its deuteron and tritium counterparts. Similarly, the occurrence of anisotropic density shapes for deuteron and tritium is explained on the basis of their lower zero point energies and thus closer following the classical potential energy surface. On the other hand, the comparison with NEO-XCHF2 results from Hammes-Schiffer and collaborators[49] highlights the importance of the electron-nuclear correlation resulting in more delocalized nuclear densities.

A third application considers molecular hydrogen and isotopomers. Although our results are consistent with previous works using the ENMO approach at either lower or higher levels of theory, they clearly show that the inclusion of nuclear-electron correlation effects is necessary. The comparison of HF electronic densities with those calculated at CCSD(T) level of theory for the different isotopomers highlights the importance of including electronic correlation effects in the quantum treatment of the lightest nuclei. Numerical tests, including the separation of the nuclear mass motion, lead to significant total energy differences.

As a future extension, the trans-correlated Hamiltonian approach[84] can be implemented as it can be formulated to include inter-particle short-range correlation through Hartree-like equations. On the other hand, to describe excited states for the nuclear wave-function, the simple version of the frozen local hole approximation (FLHA) developed by Pahl and Birkenheuer[94] could be used, with electrons replaced by protons. This FLHA method has been already implemented in the development version of the MOLPRO package.[95] Since proton density distributions are rather localized as compared with electronic densities, the most obvious advantage of such approach is that only a few self-consistent field (SCF) and non-orthogonal CI calculations would be probably necessary.

Altogether, our results suggest that the simultaneous treatment of the lightest nuclei and electrons in weakly bound systems could provide better convergence with respect to the level of theory. However, it is very important to address the problems associated with: (1) the non-separation of the center-of-mass; (2) the insufficient flexibility of the nuclear basis set; and (3) the non-inclusion of the electron-nuclear correlation before the ENMO-type implementation can be used to accurately represent the molecular energy levels. These enhancements along with the implementation of *h*- and *i*-type functions for the electrons will allow us to perform more rigorous analysis of the electronic and total energies convergence with respect to the basis set size. Our numerical tests for diatomic molecules indicate that the ENMO approach could be reformulated in terms of a translationally invariant molecular Hamiltonian (see, for example, Ref. 96). To account for wide amplitude intramolecular quantum modes, the implementation of the distributed Gaussian method that has been successfully applied to post-BO studies of $^4He_2$ and $^4He_3$,[83] is envisaged. The most appealing advantage of this method is that it preserves the analogies with standard electronic structure implementations through the addition of mid-bond functions, enabling an extension to account also for excited vibrational states. Work along these lines is currently in progress.

This article is copyrighted as indicated in the article. Reuse of AIP content is subject to the terms at: http://scitation.aip.org/termsconditions. Downloaded to IP: 147.122.21.18 On: Fri, 21 Nov 2014 17:47:01

ACKNOWLEDGMENTS

We thank Claude Leforestier and Hendrik J. Monkhorst for very useful discussions and suggestions. This work has been performed under Grant Nos. FIS2011-29596-C02-01 from MEC, Spain and a CSIC-COLCIENCIAS joint project (Ref. P2008CO1). The support of COST Action CM1002 "Convergent Distributed Environment for Computational Spectroscopy" (CODECS) is also acknowledged. N.F.A. has been supported by a predoctoral JAE fellowship from the CSIC. The calculations were performed at the Cesga Super-Computer Center (Galicia) and the Computer Centers at the IFF (CSIC) and the Centro Técnico de Informática (CTI, CSIC).

[1]S. Grebenev, J. P. Toennies, and A. F. Vilesov, Science **279**, 2083 (1998).
[2]P. Jungwirth and A. I. Krylov, J. Chem. Phys. **115**, 10214 (2001).
[3]D. López-Durán, M. P. de Lara-Castells, G. Delgado-Barrio, P. Villarreal, C. Di Paola, F. A. Gianturco, and J. Jellinek, Phys. Rev. Lett. **93**, 053401 (2004).
[4]M. P. de Lara-Castells, D. López-Durán, G. Delgado-Barrio, P. Villarreal, C. Di Paola, F. A. Gianturco, and J. Jellinek, Phys. Rev. A **71**, 033203 (2005).
[5]M. P. de Lara-Castells, G. Delgado-Barrio, P. Villarreal, and A. O. Mitrushchenkov, J. Chem. Phys. **125**, 221101 (2006).
[6]M. P. de Lara-Castells, P. Villareal, G. Delgado-Barrio, and A. O. Mitrushchenkov, J. Chem. Phys. **131**, 194101 (2009).
[7]M. P. de Lara-Castells and A. O. Mitrushchenkov, J. Phys. Chem. Lett. **2**, 2145 (2011).
[8]N. F. Aguirre, P. Villarreal, G. Delgado-Barrio, A. O. Mitrushchenkov, and M. P. de Lara-Castells, Chem. Phys. Lett. **555**, 12 (2013).
[9]I. L. Thomas, Phys. Rev. **185**, 90 (1969).
[10]I. L. Thomas, Chem. Phys. Lett. **3**, 705 (1969).
[11]I. L. Thomas and H. W. Joy, Phys. Rev. A **2**, 1200 (1970).
[12]I. L. Thomas, Phys. Rev. A **3**, 565 (1971).
[13]D. M. Bishop, Mol. Phys. **28**, 1397 (1974).
[14]D. M. Bishop and L. M. Cheung, Phys. Rev. A **16**, 640 (1977).
[15]H. J. Monkhorst, Phys. Rev. A **36**, 1544 (1987).
[16]L. Wolniewicz, J. Chem. Phys. **99**, 1851 (1993).
[17]M. Cafiero, S. Bubin, and L. Adamowicz, Phys. Chem. Chem. Phys. **5**, 1491 (2003).
[18]S. Bubin, M. Cafiero, and L. Adamowicz, Adv. Chem. Phys. **131**, 377 (2005).
[19]S. Bubin, M. Pavanello, W. C. Tung, K. L. Sharkey, and L. Adamowicz, Chem. Rev. **113**, 36 (2013).
[20]E. Mátyus and M. Reiher, J. Chem. Phys. **137**, 024104 (2012).
[21]A. D. Bochevarov, E. F. Valeev, and C. D. Sherrill, Mol. Phys. **102**, 111 (2004).
[22]M. Goli and S. Shahbazian, Theor. Chem. Acc. **131**, 1208 (2012).
[23]M. Tachikawa, K. Mori, H. Nakai, and K. Iguchi, Chem. Phys. Lett. **290**, 437 (1998).
[24]H. Nakai, Int. J. Quantum Chem. **107**, 2849 (2007).
[25]H. Nakai, K. Sodeyama, and M. Hoshino, Chem. Phys. Lett. **345**, 118 (2001).
[26]H. Nakai, Int. J. Quantum Chem. **86**, 511 (2002).
[27]H. Nakai and K. Sodeyama, J. Chem. Phys. **118**, 1119 (2003).
[28]H. Nakai, M. Hoshino, K. Miyamoto, and S. Hyodo, J. Chem. Phys. **122**, 164101 (2005).
[29]H. Nakai, M. Hoschino, K. Miyamoto, and S.-a. Hyodo, J. Chem. Phys. **123**, 237102 (2005).
[30]M. Hoshino and H. Nakai, J. Chem. Phys. **124**, 194110 (2006).
[31]B. Sutcliffe, J. Chem. Phys. **123**, 237101 (2005).
[32]M. Hoshino, H. Nishizawa, and H. Nakai, J. Chem. Phys. **135**, 024111 (2011).
[33]H. Nishizawa, M. Hoshino, Y. Imamura, and H. Nakai, Chem. Phys. Lett. **521**, 142 (2012).
[34]H. Nishizawa, Y. Imamura, Y. Ikabata, and H. Nakai, Chem. Phys. Lett. **533**, 100 (2012).
[35]T. Ishimoto, M. Tachikawa, and U. Nagashima, Int. J. Quantum Chem. **109**, 2677 (2009).
[36]T. Udagawa and M. Tachikawa, *Multi-Component Molecular Orbital Theory* (Nova Science Publishers, New York, 2009).
[37]M. Tachikawa and K. Osamura, Theor. Chem. Acc. **104**, 29 (2000).
[38]M. Tachikawa, K. Mori, K. Suzuki, and K. Iguchi, Int. J. Quantum Chem. **70**, 491 (1998).
[39]M. Tachikawa, K. Taneda, and K. Mori, Int. J. Quantum Chem. **75**, 497 (1999).
[40]M. Tachikawa, Mol. Phys. **100**, 881 (2002).
[41]M. Tachikawa, Chem. Phys. Lett. **360**, 494 (2002).
[42]T. Ishimoto, M. Tachikawa, M. Yamauchi, H. Kitagawa, H. Tokiwa, and U. Nagashima, Chem. Phys. Lett. **372**, 503 (2003).
[43]T. Ishimoto, M. Tachikawa, and U. Nagashima, J. Chem. Phys. **128**, 164118 (2008).
[44]S. P. Webb, T. Iordanov, and S. Hammes-Schiffer, J. Chem. Phys. **117**, 4106 (2002).
[45]M. W. Schmidt, K. K. Baldrige, J. A. Boatz, S. T. Elbert, M. S. Gordon, J. H. Jensen, S. Koseki, N. Matsunaga, K. A. Nguyen, S. J. Su, T. L. Windus, M. Dupuis, and J. A. Montgomery, J. Comput. Chem. **14**, 1347 (1993).
[46]T. Iordanov and S. Hammes-Schiffer, J. Chem. Phys. **118**, 9489 (2003).
[47]A. Reyes, M. V. Pak, and S. Hammes-Schiffer, J. Chem. Phys. **123**, 064104 (2005).
[48]C. Swalina, M. V. Pak, A. Chakraborty, and S. Hammes-Schiffer, J. Phys. Chem. A **110**, 9983 (2006).
[49]C. Ko, M. V. Pak, C. Swalina, and S. Hammes-Schiffer, J. Chem. Phys. **135**, 054106 (2011).
[50]J. H. Skone, M. V. Pak, and S. Hammes-Schiffer, J. Chem. Phys. **123**, 134108 (2005).
[51]C. Swalina, M. V. Pak, and S. Hammes-Schiffer, Chem. Phys. Lett. **404**, 394 (2005).
[52]J. F. Capitani, R. F. Nalewajski, and R. G. Parr, J. Chem. Phys. **76**, 568 (1982).
[53]Y. Shigeta, H. Takahashi, S. Yamanaka, M. Mitani, H. Nagao, and K. Yamaguchi, Int. J. Quantum Chem. **70**, 659 (1998).
[54]T. Kreibich and E. K. U. Gross, Phys. Rev. Lett. **86**, 2984 (2001).
[55]Y. Imamura, H. Kiryu, and H. Nakai, J. Comput. Chem. **29**, 735 (2008).
[56]Y. Imamura, Y. Tsukamoto, H. Kiryu, and H. Nakai, Bull. Chem. Soc. Jpn. **82**, 1133 (2009).
[57]M. V. Pak, A. Chakraborty, and S. Hammes-Schiffer, J. Phys. Chem. A **111**, 4522 (2007).
[58]T. Udagawa and M. Tachikawa, J. Chem. Phys. **125**, 244105 (2006).
[59]R. Colle and O. Salvetti, Theor. Chem. Acta **37**, 329 (1975).
[60]S. A. González, N. F. Aguirre, and A. Reyes, Int. J. Quantum Chem. **108**, 1742 (2008).
[61]S. A. González and A. Reyes, Int. J. Quantum Chem. **110**, 689 (2010).
[62]D. V. Moreno, S. A. González, and A. Reyes, J. Phys. Chem. A **114**, 9231 (2010).
[63]D. V. Moreno, S. A. González, and A. Reyes, J. Chem. Phys. **134**, 024115 (2011).
[64]F. Moncada, S. A. González, and A. Reyes, Mol. Phys. **108**, 1545 (2010).
[65]F. Moncada, D. Cruz, and A. Reyes, Chem. Phys. Lett. **539**, 209 (2012).
[66]R. Flores-Moreno, V. G. Zakrzewski, and J. V. Ortiz, J. Chem. Phys. **127**, 134106 (2007).
[67]R. Flores-Moreno, S. A. González, N. F. Aguirre, E. F. Posada, J. Romero, F. Moncada, G. Merino, and A. Reyes, LOWDIN: A general code for the treatment of any particle, 2012, see https://sites.google.com/site/lowdinproject/home.
[68]J. Romero, E. F. Posada, R. Flores-Moreno, and A. Reyes, J. Chem. Phys. **137**, 074105 (2012).
[69]H. J. Werner, P. J. Knowles, R. Lindh, F. R. Manby, M. Schütz *et al.*, MOLPRO, version 2009.1, a package of *ab initio* programs, 2009, see http://www.molpro.net.
[70]K. Patkowski, J. Chem. Phys. **137**, 034103 (2012).
[71]D. E. Woon and T. H. Dunning, Jr., J. Chem. Phys. **100**, 2975 (1994).
[72]T. van Mourik, A. K. Wilson, and T. H. Dunning, Jr., Mol. Phys. **96**, 529 (1999).
[73]S. F. Boys and F. Bernardi, Mol. Phys. **19**, 553 (1970).
[74]W. Cencek, M. Przybytek, J. Komasa, J. B. Mehl, B. Jeziorski, and K. Szalewicz, J. Chem. Phys. **136**, 224303 (2012).
[75]K. Taneda and K. Mori, Chem. Phys. Lett. **298**, 293 (1998).
[76]S. Y. Leu and C. Y. Mou, J. Chem. Phys. **101**, 5910 (1994).
[77]M. P. de Lara-Castells, N. F. Aguirre, and A. O. Mitrushchenkov, Chem. Phys. **399**, 272 (2012).
[78]T. Kato, Commun. Pure Appl. Math. **10**, 151 (1957).

This article is copyrighted as indicated in the article. Reuse of AIP content is subject to the terms at: http://scitation.aip.org/termsconditions. Downloaded to IP: 147.122.21.18 On: Fri, 21 Nov 2014 17:47:01

[79]Y. Nakatsuka, T. Nakajima, and K. Hirao, J. Chem. Phys. **132**, 174108 (2010).
[80]N. C. Handy, Y. Yamaguchi, and H. F. Schaefer III, J. Chem. Phys. **84**, 4481 (1986).
[81]M. P. de Lara-Castells, N. F. Aguirre, P. Villarreal, G. Delgado-Barrio, and A. O. Mitrushchenkov, J. Chem. Phys. **132**, 194313 (2010).
[82]I. P. Hamilton and J. C. Light, J. Chem. Phys. **84**, 306 (1986).
[83]T. González-Lezana, J. Rubayo-Soneira, S. Mirét-Artés, F. A. Gianturco, G. Delgado-Barrio, and P. Villarreal, Phys. Rev. Lett. **82**, 1648 (1999).
[84]H. Luo, J. Chem. Phys. **133**, 154109 (2010).
[85]I. Baccarelli, F. Gianturco, and F. Schneider, J. Phys. Chem. A **101**, 6054 (1997).
[86]J. J. Liang, C. L. Yang, L. Z. Wang, and Q. G. Zhang, J. Chem. Phys. **136**, 094307 (2012).
[87]A. N. Panda and N. Sathyamurthy, J. Phys. Chem. A **107**, 7125 (2003).
[88]S. Bubin, F. Leonarski, M. Stanke, and L. Adamowicz, Chem. Phys. Lett. **477**, 12 (2009).
[89]M. Stanke, S. Bubin, M. Molski, and L. Adamowicz, Phys. Rev. A **79**, 032507 (2009).
[90]S. Bubin, M. Stanke, and L. Adamowicz, J. Chem. Phys. **135**, 074110 (2011).
[91]S. Bubin, M. Stanke, M. Molski, and L. Adamowicz, Chem. Phys. Lett. **494**, 21 (2010).
[92]K. P. Huber and G. Herzberg, *Molecular Spectra Molecular Structure, Constants of Diatomic Molecules* (Van Nostrand Reinhold, New York, 1979).
[93]J. B. Nelson and G. C. Tabisz, Phys. Rev. A **28**, 2157 (1983).
[94]E. Pahl and U. Birkenheuer, J. Chem. Phys. **124**, 214101 (2006).
[95]M. P. de Lara-Castells and A. O. Mitrushchenkov, J. Phys. Chem. C **115**, 17540 (2011).
[96]B. T. Sutcliffe and R. G. Woolley, J. Chem. Phys. **137**, 22A544 (2012).

This article is copyrighted as indicated in the article. Reuse of AIP content is subject to the terms at: http://scitation.aip.org/termsconditions. Downloaded to IP: 147.122.21.18 On: Fri, 21 Nov 2014 17:47:01

C. Paper III

THE JOURNAL OF PHYSICAL CHEMISTRY A

Article

pubs.acs.org/JPCA

Negative Muon Chemistry: The Quantum Muon Effect and the Finite Nuclear Mass Effect

Edwin Posada,[†] Félix Moncada,[†,‡] and Andrés Reyes*,[†]

[†]Departamento de Química, Universidad Nacional de Colombia, Av. Cra. 30 #45-03, Bogotá, Colombia

[‡]Programa de Química, Universidad de la Amazonia, Calle 17 Diagonal 17 - Carrera 3F, Florencia, Colombia

Supporting Information

ABSTRACT: The any-particle molecular orbital method at the full configuration interaction level has been employed to study atoms in which one electron has been replaced by a negative muon. In this approach electrons and muons are described as quantum waves. A scheme has been proposed to discriminate nuclear mass and quantum muon effects on chemical properties of muonic and regular atoms. This study reveals that the differences in the ionization potentials of isoelectronic muonic atoms and regular atoms are of the order of millielectronvolts. For the valence ionizations of muonic helium and muonic lithium the nuclear mass effects are more important. On the other hand, for 1s ionizations of muonic atoms heavier than beryllium, the quantum muon effects are more important. In addition, this study presents an assessment of the nuclear mass and quantum muon effects on the barrier of Heμ + H_2 reaction.

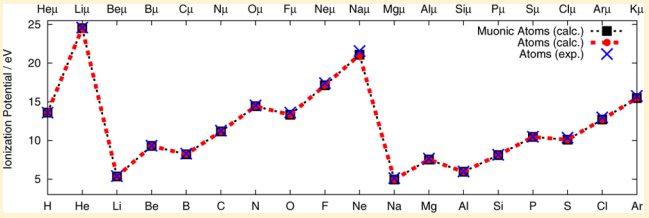

INTRODUCTION

The scope of chemistry, once limited to the study of systems containing electrons and atomic nuclei, has been evolving since the middle of the 20th century as a result of important advances in the generation and manipulation of molecules containing subatomic particles such as positive muons (μ^+), positrons (e^+), and antiprotons among others. The amount of information gathered so far on molecular systems containing μ^+ and e^+ is such that e^+ and μ^+ chemistry are nowadays well established areas of research.[1,2]

In contrast, exotic systems containing negative muons (denoted as muons or μ in the rest of the document) have mainly attracted the attention of the physics community for more than 60 years as a result of their potential to catalyze nuclear fusion processes. References 2−5 and references therein present overviews of muon catalyzed fusion in the dtμ molecule.

Nevertheless, the chemical properties of μ-atoms (denoted in the rest of the document by Xμ, where X is the atomic symbol) and μ-molecules were rarely investigated in the 20th century[6−12] due to serious experimental limitations associated with their preparation and manipulation.

In recent years, a series of breakthrough investigations by Fleming and co-workers[13−15] have suddenly revived the interest in the chemistry of muonic atoms and molecules. These investigations reported the measurement of reaction rates for the collisional process Heμ + H_2 → HeμH + H. In these studies the muonic helium atom (Heμ) is regarded as a heavy isotope of hydrogen, because the muon orbital is so close to the helium nucleus that it is assumed that the μ perfectly screens one of its positive charges.

Inspired by Fleming's work, Moncada et al. studied the electronic and muonic structure of muonic atoms with the any-particle molecular orbital Hartree−Fock (APMO/HF) approach.[16,17] Their studies showed that ionization potentials and radial distributions of valence electrons in neutral muonic atoms with atomic number Z followed very closely those of valence electrons of neutral all-electronic atoms with atomic number $Z - 1$. Although small differences in the calculated properties were observed, no effort was made to assess the extent of the full screening approximation of one positive nuclear charge used by Fleming and co-workers[14,15] in their studies of muonic helium.

Consequently, the present work aims at quantifying the differences between the ionization energies of muonic and regular atoms and assessing the impact of the quantum muon effect (QME) on the atomic properties and chemical reactivity. To do that, we analyze atomic muonic systems in which both electrons and muon are described as quantum waves at the APMO full-CI level of theory. We will refer to this method as APMO/FCI.

We analyzed in detail the nuclear mass effects (NMEs) and QMEs on the ionization potentials (IPs) of muonic atoms and on the reaction barriers for H + H_2 and Heμ + H_2 collisional systems previously studied by Fleming and co-workers.[14,15]

The NME on atomic IPs is investigated by including the finite nuclear mass correction (FNMC).[18,19] FNMCs were not performed on reaction barrier calculations because it has been reported that it wrongly predicts an increase of 53.6 cm^{-1} in

Received: February 5, 2014
Revised: September 3, 2014
Published: September 4, 2014

ACS Publications © 2014 American Chemical Society

reaction barrier of the H + H_2[20] rather than the lowering of 14 cm^{-1}.[21] The NME on reaction energies is estimated by comparison with previous results that included the diagonal Born−Oppenheimer correction (DBOC).[14,22]

This paper is organized as follows. We summarize the equations of the APMO/FCI method and the FNMC in the Theory section. We provide some computational details in Computational Details. We present the calculated ionization potentials for muonic atoms and the calculated energy barrier for the Heμ + H_2 reaction and discuss the differences of these chemical properties compared to those of all-electron atoms and molecules in the Results and Discussion. Finally, we provide concluding remarks and perspectives for future work in the conclusions section.

THEORY

Here we summarize the expressions of the APMO Hartree−Fock (APMO/HF)[23,24] and APMO/FCI methods including the FNMC for systems containing quantum electrons and muons and classical nuclei (point charges).

Note that APMO/HF and APMO/FCI expressions are closely related to those of the nuclear orbital plus molecular orbital (NOMO)[25−27] and multicomponent molecular orbital (MCMO)[28−30] methods. We use atomic units throughout this document.

APMO/HF Theory. The nonrelativistic Hamiltonian, H_{tot}, of a molecular system containing N^e electrons, N^μ muons, and N^{nuc} nuclei is

$$H_{tot} = -\sum_i^{N^e}\frac{1}{2}\nabla_i^2 - \sum_i^{N^\mu}\frac{1}{2m_\mu}\nabla_i^2 - \sum_A^{N^{nuc}}\frac{1}{2M_A}\nabla_i^2 + \sum_i^{N^e}\sum_{j>i}^{N^e}\frac{1}{r_{ij}} + \sum_i^{N^\mu}\sum_{j>i}^{N^\mu}\frac{1}{r_{ij}} + \sum_A^{N^{nuc}}\sum_{B>A}^{N^{nuc}}\frac{Z_A Z_B}{r_{AB}} + \sum_i^{N^e}\sum_j^{N^\mu}\frac{1}{r_{ij}} - \sum_i^{N^e}\sum_A^{N^{nuc}}\frac{Z_A}{r_{iA}} - \sum_i^{N^\mu}\sum_A^{N^{nuc}}\frac{Z_A}{r_{iA}} \quad (1)$$

here m_μ is the muon mass and M_A and Z_A are the mass and charge of nucleus A, respectively.

Under the framework of the Born−Oppenheimer (BO) approximation for nuclei, the BO Hamiltonian H_{BO} can be obtained by removing the nuclear kinetic energy operators from H_{tot}.

The APMO/HF wave function for the electron−muon system, Ψ_0, is approximated as a product of single configurational wave functions

$$\Psi_0 = |\Phi^e\rangle|\Phi^\mu\rangle \quad (2)$$

Because of their Fermionic nature, electronic and muonic wave functions, Φ^e and Φ^μ, are represented as Slater determinants of molecular orbitals (MOs), ψ_i. MOs for each quantum species are obtained by solving the one-particle APMO/HF equations

$$f^e(i)\psi_i^e = \varepsilon_i^e\psi_i^e \qquad i = 1, ..., N^e \quad (3)$$

$$f^\mu(i)\psi_i^\mu = \varepsilon_i^\mu\psi_i^\mu \qquad i = 1, ..., N^\mu \quad (4)$$

The above Fock operators f^α are defined as

$$f^e(i) = h^e(i) + \sum_j^{N^e}[J_j^e - K_j^e] + \sum_j^{N^\mu}J_j^\mu \quad (5)$$

$$f^\mu(i) = h^\mu(i) + \sum_j^{N^\mu}[J_j^\mu - K_j^\mu] + \sum_j^{N^e}J_j^e \quad (6)$$

where $h^\alpha(i)$, J_i^α, and K_i^α ($\alpha = e, \mu$) are the core, Coulomb, and exchange operators for particle i of species α. Converged MOs of electrons and muons are obtained after solving eqs 3 and 4 iteratively. These MOs are constructed as linear combinations of Gaussian type functions (GTFs). As observed in eqs 5 and 6, the effective field experienced by one quantum species depends on the MOs of all quantum species.

Finite Nuclear Mass Correction (FNMC). The use of the BOA for muonic systems leads to large errors in the calculation of total energies[31] because the mass of the μ is about one-ninth that of a proton. To correct for these errors, we previously extended the FNMC[18,19] to the APMO equations for electrons and muons.[17] At the APMO/HF level the corrected FNMC Fock matrix, F^α_{FNMC}, is obtained by summing a FNMC matrix, $\mathbf{Q}^\alpha$, and the BO Fock matrix, F^α:

$$\mathbf{F}^\alpha_{FNMC} = \mathbf{F}^\alpha + \mathbf{Q}^\alpha \quad (7)$$

Electronic and muonic FNMC matrix elements Q^α_{ijAB} are related to the corresponding kinetic energy matrix elements T^α_{ijAB},

$$Q^{\ \alpha}_{ijAB} = \begin{cases} \frac{m_\alpha}{M_A}T^\alpha_{ijAB} & \text{if A = B} \\ 0 & \text{if A} \neq \text{B} \end{cases} \quad (8)$$

$$T^\alpha_{ijAB} = \left\langle \phi^\alpha_{iA}\left| -\frac{\nabla^2}{2m_\alpha}\right|\phi^\alpha_{jB}\right\rangle \quad (9)$$

where ϕ^α_{iA} is a basis function of species α centered on nucleus A.

APMO/FCI Method. The APMO/FCI wave function of a system composed of quantum electrons and muons is given by

$$\Psi_{FCI} = C_0|\Phi_0^e\rangle|\Phi_0^\mu\rangle + \sum_{ar}C_{ar}|\Phi^e_{a\to r}\rangle|\Phi_0^\mu\rangle + \sum_{a'r'}C_{a'r'}|\Phi_0^e\rangle|\Phi^\mu_{a'\to r'}\rangle + \sum_{abrs}C_{abrs}|\Phi^e_{ab\to rs}\rangle|\Phi_0^\mu\rangle + \sum_{a'b'r's'}C_{a'b'r's'}|\Phi_0^e\rangle|\Phi^\mu_{a'b'\to r's'}\rangle + \sum_{aa'rr'}C_{aa'rr'}|\Phi^e_{a\to r}\rangle|\Phi^\mu_{a'\to r'}\rangle + ... \quad (10)$$

where Φ_0^e and Φ_0^μ are APMO/HF reference Slater determinants, and $a \to r$ represents a single excitation and $ab \to rs$ represents a double excitation. The FCI wave function is obtained by summing all possible configurations obtained from an APMO/HF reference wave function.

The combination coefficients, C, are obtained by diagonalizing the Hamiltonian matrix, $\mathbf{H}$. The matrix elements, H_{ij}, are given by

$$H_{ij} = \langle\Psi_i|\hat{H}|\Psi_j\rangle \quad (11)$$

In the above equation each Ψ_i is a product of electronic and muonic Slater determinants (as in eq 2). The correlation energy is calculated as the difference of FCI and HF energies,

dx.doi.org/10.1021/jp501289s | J. Phys. Chem. A 2014, 118, 9491−9499

Table 1. APMO/FCI $^4He\mu$ and $^4He\mu^+$ Total Energies, $^4He\mu$ Ionization Potential, Muon−Electron Interaction ($V_{\mu-e}$), and Muon−Electron Correlation Energies ($E_{\mu-e}^{corr}$)[a]

e:μ basis set	$E(He\mu)$/au	$E(He\mu^+)$/au	IP/eV	$V_{\mu-e}$/eV	$E_{\mu-e}^{corr}$/eV
31s25p:1s	−341.915636	−341.415693	13.60414	27.20917	-1.7×10^{-8}
31s25p:7s	−399.964618	−399.464673	13.60419	27.20838	-5.6×10^{-7}
31s25p:13s	−402.620822	−402.120878	13.60418	27.20837	-5.5×10^{-7}
31s25p:25s	−402.720712	−402.220767	13.60418	27.20837	-5.2×10^{-7}
31s25p:31s	−402.720813	−402.220869	13.60418	27.20837	-5.3×10^{-7}
31s25p:31s7p	−402.720814	−402.220869	13.60422	27.20837	-3.6×10^{-5}
31s25p:31s13p	−402.720814	−402.220869	13.60422	27.20837	-3.6×10^{-5}
31s25p:31s25p	−402.720814	−402.220869	13.60422	27.20837	-3.6×10^{-5}
31s25p:31s7p5d	−403.206489	−402.706544	13.60422	27.20876	-3.6×10^{-5}
31s25p:31s7p7d	−403.206494	−402.706549	13.60422	27.21090	-3.6×10^{-5}
accurate[b]	−402.637263	−402.137317	13.60424		

[a]Calculations were performed with the 31s25p electronic basis set and different choices of muonic basis sets. [b]IP calculated as the difference of the exact energy for $^4He\mu^+$ of eq 17 and high-precision variational energy for $^4He\mu$ of ref 34.

$$E^{corr} = \langle \Psi_{FCI}|\hat{H}|\Psi_{FCI}\rangle - \langle \Psi_0|\hat{H}|\Psi_0\rangle \quad (12)$$

COMPUTATIONAL DETAILS

All calculations were carried out with an updated version of the LOWDIN computational package[32] that incorporates new features: (1) a two particle APMO/FCI method for muonic helium-like atoms; (2) an interface to Knowles et al.'s FCI routine[33] to perform electronic FCI calculations at the APMO level. Calculations including electron and muon−electron correlation at the FCI level are denoted as APMO/FCI, and those including exclusively electron correlation at the FCI level are called APMO/eFCI. APMO/FCI calculations were performed for systems containing one electron and one muon employing the 31s25p muonic and the 31s25p electronic even tempered basis sets.[16] Basis set exponents are found in Table S.1 of the Supporting Information.

APMO/eFCI employing the cc-pVTZ electronic[34−36] and the 13s muonic[16] basis sets were carried out to analyze systems comprising multiple electrons and one muon.

All calculations in this study considered atomic nuclei as point charges. Calculations performed without the FNMC are referred to as infinite nuclear mass limit calculations. All calculations were performed by employing the nuclear mass of the most abundant isotope of corresponding element and Cartesian Gaussian basis sets for electrons and muons.

Ionization potentials, IPs, were calculated in terms of the energy difference,

$$IP(X) = E(X) - E(X^+) \quad (13)$$

of the neutral atom, X, and its cation, X^+.

To gain insight into the origin of the differences in the IPs of a muonic atom $X\mu$, with atomic number Z, and a regular atom Y, with atomic number $Z - 1$, we calculated the IP of five systems:

1. ^{M_Y}Y: regular atom including FNMC
2. $^{\infty}Y$: regular atom with infinite nuclear mass
3. $^{M_X}X\mu$: muonic atom including FNMC
4. $^{\infty}X\mu$: muonic atom with infinite nuclear mass
5. $^{(M_X+m_\mu)}Y$: muonic atom with nucleus-muon pseudonucleus including FNMC.

NMEs on IPs were estimated as

$$NME = IP(^{(M_X+m_\mu)}Y) - IP(^{M_Y}Y) \quad (14)$$

and QMEs on IPs were estimated as

$$QME = IP(^{\infty}X\mu) - IP(^{\infty}Y) \quad (15)$$

The sum of NME and QME is a good approximation to the difference in the IPs of regular and muonic atoms

$$\Delta IP = IP(^{M_X}X\mu) - IP(^{M_Y}Y) \approx NME + QME \quad (16)$$

An analogous scheme was utilized to analyze the energy differences of the reaction barriers of the $H + H_2$ and $He\mu + H_2$ collisional systems.

We computed the exact ground-state energy of hydrogen-like and muon-hydrogen-like atoms from the solution to the Schrödinger equation:

$$E = -\frac{m_\alpha M}{m_\alpha + M}\frac{Z^2}{2} \quad (17)$$

where M is the nuclear mass and m_α is either the electronic or muonic mass.

Fleming et al.[15] studied the QME on the reaction barrier of $He\mu + H_2$ using a pseudopotential approach to model the electron−muon interaction. In this approach electrons are considered explicitly as quantum particles and the attractive interaction of the electron with the helium−muon pseudonucleus is described with the expression $-(1/r + \alpha/2)\exp(-\alpha r) - 1/r$ ($\alpha = 2Zm_\mu = 827.07306$ au^{-1}). This electronic potential behaves like $-2/r$ near the helium nucleus and like $-1/r$ far from it. Figure S.1 in the Supporting Information plots this potential. We have implemented this pseudopotential in our LOWDIN code by fitting the expression $-(1/r + \alpha/2)\exp(-\alpha r)$ to a linear combination of ten Gaussian functions. Details of the fitting can be found in Table S.2 of the Supporting Information. We should note that the expression in ref 15 is missing a minus sign preceding the pseudopotential term.

RESULTS AND DISCUSSION

It is common practice to assume that the electronic properties of a muonic atom with atomic number Z are identical to those of a regular atom with atomic number $Z - 1$[14] as a result of the muon perfect screening of a positive nuclear charge.

Previous APMO/HF calculations revealed the existence of small but non-negligible differences in the ionization potentials of muonic atoms with atomic number Z and regular atoms with atomic number $Z - 1$.[16] Along those lines, in this study we

dx.doi.org/10.1021/jp501289s | J. Phys. Chem. A 2014, 118, 9491−9499

utilize the more accurate APMO/FCI method to quantify these differences and analyze their origin.

With these goals in mind in this section we (1) estimate the errors in the calculation of IPs of muonic atoms induced by the choice of theoretical methods and basis sets, (2) compare the IPs of neutral muonic and regular atoms, (3) analyze the NMEs and QMEs in the IPs of muonic helium and lithium, (4) analyze NME and QME on observed IP differences of helium-like muonic and hydrogen-like atoms, and (5) calculate NME and QME on the reaction barrier of the Heμ + H_2 and assess the validity of the full screening approximation employed in Fleming's papers.[14,15]

Muonic Basis Sets. Here we analyze the impact of the muonic basis set choice on the ionization potentials and muon-electron correlation energies.

Table 1 lists APMO/FCI ionization potentials for ^{4}Heμ. Calculations were performed employing the FNMC and the 31s25p electronic basis set and different muonic basis set choices. As observed, there is a weak dependence of the choice of muonic basis sets on the calculated IPs. For instance, the IPs calculated with the 1s and the 31s25p muonic basis sets only differ by 0.07 meV. For reference, Table 1 also includes a very accurate IP value, calculated as the difference of the exact energy for ^{4}Heμ^+ of eq 17 and the high-precision variational energy for ^{4}Heμ of ref 37. We observe that our APMO/FCI IP result differs from the latter by less than 0.10 meV, thus confirming that the APMO/FCI method accurately estimates the IPs of muonic atoms. We should note that our calculated energies are sometimes lower than the reference value, because the FNMC scheme neglects nondiagonal mass polarization terms.[17,18]

In addition, Table 1 lists Heμ muon−electron correlation energies calculated with eq 12 using different muonic basis sets. As observed, even with 31s25p:31s25p electronic:muonic basis sets we obtained a muon−electron correlation energy of -3.6×10^{-5} eV. This is negligible when compared to the correlation energy of the electron−muon interaction (27.2 eV). Therefore, we conclude that the muon−electron correlation energy contribution can be neglected in the calculation of the electronic IP of a muonic atom. Consequently, accurate calculations of the IPs of muonic atoms can be still be performed with the APMO/eFCI method, which includes only electronic correlation.

Ionization Potentials of Muonic Atoms. Table 2 presents the APMO/eFCI IPs of a helium atom and a muonic lithium atom calculated with different electronic basis sets. Calculations were performed by employing the FNMC and the 13s muonic basis set. Eleven s-type tight Gaussians were added to some of the electronic basis sets. For reference, this table also presents the experimental IP of the He atom. As observed, as the size of the electronic basis set increases, the calculated IP of the He and Liμ atoms approach the experimental IP of He. Furthermore, the difference between these IPs presents a weak dependence on the choice of electronic basis sets. For instance, the ΔIPs calculated with the cc-pVTZ and the cc-pVT5Z with 11 s-type tight Gaussians only differ in 0.17 meV. These results allow us to conclude that it is not necessary to use a very large electronic basis set to compare the IPs of muonic and regular atoms.

Figure 1 plots the APMO/eFCI IPs for muonic and regular atoms and contrast them with experimental results for regular atoms. It is evidenced in this figure that the IPs of muonic atoms coincide almost perfectly with the calculated and experimental IPs of regular atoms with atomic number $Z - 1$.

Table 2. APMO/eFCI Ionization Potential Energies for Liμ and He Atoms[a]

basis set	IP Liμ/eV	IP He/eV	ΔIP/meV
cc-pVTZ	24.52547	24.52356	1.91
cc-pVTZ + 11s	24.52342	24.52145	1.97
aug-cc-pVTZ + 11s	24.53420	24.53221	1.99
cc-pVQZ	24.56144	24.55942	2.02
cc-pVQZ + 11s	24.56320	24.56114	2.06
aug-cc-pVQZ + 11s	24.56787	24.56580	2.07
cc-pV5Z	24.57727	24.57522	2.05
cc-pV5Z + 11s	24.57750	24.57543	2.07
exp[b]		24.587	

[a]APMO/eFCI ionization potential energies for Liμ and He atoms. Calculations were performed by employing the 13s muonic basis set and different choices of electronic basis sets. [b]Experimental value taken from ref 38.

In addition, Table 3 lists the APMO/eFCI IPs of muonic atoms with $Z = 2-19$ and regular atoms with $Z = 1-18$. As observed, except for ^{39}Kμ, the IPs of muonic atoms are always larger than those of isoelectronic regular atoms with differences ranging between −0.03 and +5.85 meV. On average, these differences decrease when Z increases. Two types of effects are responsible for originating these differences in the IPs of regular and muonic atoms: the existing mass differences and the muon quantum effects.

Nuclear Mass and Quantum Muon Effects on Heμ and Liμ. These elements have been selected because they present the largest IP differences with respect to their regular atom counterparts. Prior to analyzing these small effects, it is necessary to assess the accuracy of the FNMC in the calculation of the NME. As shown in Table 4, the FNMC reduces the infinite mass IPs of ^{1}H and ^{4}He by 7.39 and 3.49 meV, respectively. These results are in good agreement with those obtained with the DBOC, 7.41 and 3.96 meV.[39]

The NME on the IPs of muonic helium and muonic lithium was deduced by comparing the IPs of ^{1}H and ^{4}He with those of their heavier isotopes $^{4.1}$H and $^{7.1}$He, respectively. Similarly, the QME on these IPs was estimated by comparing the IPs at the infinite nuclear mass limit of the muonic atoms $^\infty$Heμ and $^\infty$Liμ with those of the regular atoms $^\infty$H and $^\infty$He, respectively.

As observed in Table 4, NMEs on Heμ and Liμ account for 96% and 83% of the observed IP differences, respectively. On the other hand, QMEs contributions to the IP differences are only 0.3 and 0.4 meV for Heμ and Liμ, respectively. Although small, these effects are still significant for accurate calculations.

Any attempt to analyze the origin of the energy differences in other poly-electronic atoms is problematic because the IP difference is of the order of the numerical errors associated with the basis sets and the level of theory employed in the calculation. Therefore, to gain insight into the origin and magnitude of the NMEs and QMEs, we have analyzed the IPs of muonic helium-like atoms. These systems present two advantages over poly-electronic muonic atoms: (1) The differences between their IPs with respect to the IPs of hydrogen-like atoms are larger. (2) They comprise one nucleus, one muon, and one electron, and therefore it is easier to track the different QMEs on the different energy contributions.

Muonic Helium-Like Atoms. Figure 2 presents the IPs of muonic helium-like atoms from $Z = 2$ to 19 and hydrogen-like

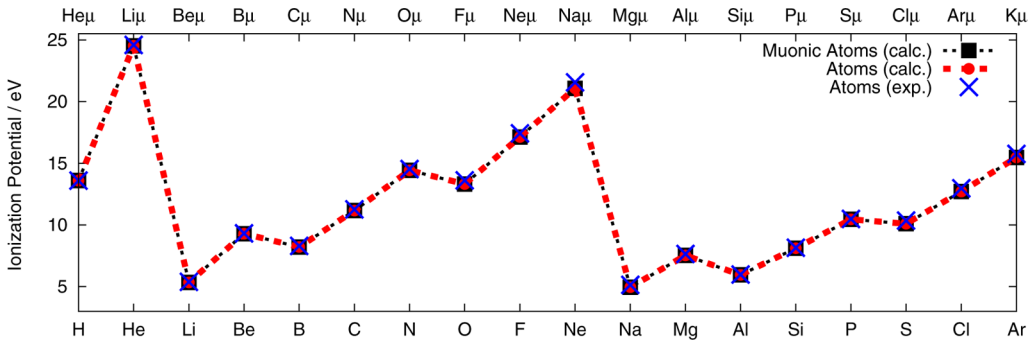

Figure 1. APMO/eFCI ionization potentials for regular and muonic atoms. Experimental IPs for regular atoms.

Table 3. APMO/eFCI IPs of Regular and Muonic Atoms[a]

	regular atoms IP/eV			muonic atoms IP/eV		ΔIP/meV
# e^-	atom	exp[b]	APMO/eFCI	atom	APMO/eFCI	APMO/eFCI
1	^{1}H	13.598	13.59313	^{4}Heμ	13.59898	5.85
2	^{4}He	24.587	24.52418	^{7}Liμ	24.52609	1.91
3	^{7}Li	5.392	5.34180	^{9}Beμ	5.34193	0.13
4	^{9}Be	9.323	9.28687	^{11}Bμ	9.28708	0.21
5	^{11}B	8.298	8.21068	^{12}Cμ	8.21089	0.20
6	^{12}C	11.260	11.16167	^{14}Nμ	11.16214	0.46
7	^{14}N	14.534	14.42488	^{16}Oμ	14.42529	0.41
8	^{16}O	13.618	13.31369	^{19}Fμ	13.31409	0.40
9	^{19}F	17.423	17.12591	^{20}Neμ	17.12598	0.08
10	^{20}Ne	21.565	21.07783	^{23}Naμ	21.07816	0.33
11	^{23}Na	5.139	4.95207	^{24} Mgμ	4.95209	0.01
12	^{24} Mg	7.646	7.52758	^{27}Alμ	7.52761	0.04
13	^{27}Al	5.986	5.94859	^{28}Siμ	5.94860	0.01
14	^{28}Si	8.152	8.11407	^{31}Pμ	8.11412	0.06
15	^{31}P	10.487	10.45600	^{32}Sμ	10.45600	0.00
16	^{32}S	10.360	10.09386	^{35}Clμ	10.09387	0.01
17	^{35}Cl	12.968	12.70387	^{40}Arμ	12.70390	0.02
18	^{40}Ar	15.760	15.46646	^{39}Kμ	15.46643	−0.03
	aad[c]		0.15405			

[a][cc-pVTZ:13s] electron:muon basis sets. Experimental IPs for regular atoms are included for comparison. [b]Experimental values taken from ref 38. [c]Average absolute deviation with respect to experimental values.

Table 4. Nuclear Mass and Quantum Muon Effects on the IPs of Heμ and Liμ[a]

atom	IP/eV	atom	IP/eV
^{1}H	13.59313	^{4}He	24.52418
$^{\infty}$H	13.60052	$^{\infty}$He	24.52767
^{4}Heμ	13.59898	^{7}Liμ	24.52609
$^{\infty}$Heμ	13.60081	$^{\infty}$Luμ	24.52807
$^{4.1}$H	13.59872	$^{7.1}$He	24.52576
NME/meV	5.60 (96%)	NME/meV	1.58 (83%)
QME/meV	0.29 (5%)	QME/meV	0.40 (21%)
ΔIP/meV	5.85 (100%)	ΔIP/meV	1.91 (100%)

[a]APMO/eFCI calculations were performed with the cc-pVTZ:13s electron:muon basis sets.

atoms from $Z = 1$ to 18. As expected, the IP of a muonic helium-like atom with atomic number Z approaches the IP of a hydrogen-like atom with atomic number $Z - 1$.

Nuclear Mass Effect and Quantum Muon Effect in Muonic Helium-Like Atoms. Figure 3 presents the calculated differences between the IPs of muonic helium-like atoms with atomic number Z and hydrogen-like atoms with atomic number $Z - 1$. As observed, the IP of the muonic helium-like atom is greater than that of the regular hydrogen-like atom. These differences tend to increase with Z, ranging from 4.41 to 27.02 meV.

We have analyzed these differences in terms of NMEs and QMEs using eqs 14 and 15, respectively. We observe that NMEs range from −1.36 to +7.80 meV, increasing with the difference in nuclear masses. For instance, when the mass difference is 1.1 Da (^{12}Cμ^{4+}−^{11}B^{4+}), the NME is 1.54 meV and when the mass difference is 5.1 Da (^{40}Arμ^{16+}−^{35}Cl^{16+}) the NME is 7.80 meV. In the case of ^{39}Kμ^{17+}−^{40}Ar^{17+} the NME reduces the IP by 1.36 meV because the muonic atom has a smaller nuclear mass than the regular atom. On the other hand, the QME increases the IP of muonic atoms linearly with the atomic number, ranging from 0.35 meV (^{4}Heμ−^{1}H) to 20.52 meV (^{39}Kμ^{17+}−^{40}Ar^{17+}).

Further analysis reveals that the NME is the most important contribution to the IP differences of ^{4}Heμ−^{1}H and ^{7}Liμ^{+}−^{4}He^{+}. However, for muonic atoms with $Z > 3$ the relative contribution of the QME becomes larger. For instance, it accounts for 90% of the ^{32}Sμ^{14+}−^{31}P^{14+} IP difference. Furthermore, in the ^{39}Kμ^{17+}−^{40}Ar^{17+} case, the NME has the opposite sign and is 1 order of magnitude smaller than the QME.

The results collected so far show that the NME is more predominant in the ionization of 1s electrons of light muonic atoms, such as ^{4}Heμ, whereas the QME is the most important effect in the core ionizations of heavier muonic atoms, such as ^{39}Kμ.

Origin of the Quantum Muon Effect in Muonic Helium-Like Atoms. Here we analyze the different contributions to the QME. The energy of a muonic helium-like atom with atomic number Z, denoted here as $^{\infty}$Yμe, is

$$E(^{\infty}\mathrm{Y}\mu e) = K_{\mu} + K_{e} + V_{\mathrm{Y}\mu} + V_{\mathrm{Y}e} + V_{\mu e} + E^{\mathrm{corr}}_{\mu-e} \quad (18)$$

Similarly, the energies of the muonic hydrogen-like atom, denoted as $^{\infty}$Yμ, and the hydrogen-like atom with atomic number $Z - 1$, denoted here as $^{\infty}$Xe, are

$$E(^{\infty}\mathrm{X}e) = -\mathrm{IP}(^{\infty}\mathrm{X}e) = K_{e} + \Delta K_{e} + V_{\mathrm{X}e} \quad (19)$$

$$E(^{\infty}\mathrm{Y}\mu) = K_{\mu} + \Delta K_{\mu} + V_{\mathrm{Y}\mu} + \Delta V_{\mathrm{Y}\mu} \quad (20)$$

The IP of a muonic helium-like atom is

$$\mathrm{IP}(^{\infty}\mathrm{Y}\mu e) = E(^{\infty}\mathrm{Y}\mu) - E(^{\infty}\mathrm{Y}\mu e) = \Delta K_{\mu} + \Delta V_{\mathrm{Y}\mu} - K_{e} - V_{\mathrm{Y}e} - V_{\mu e} - E^{\mathrm{corr}}_{\mu-e} \quad (21)$$

dx.doi.org/10.1021/jp501289s | J. Phys. Chem. A 2014, 118, 9491−9499

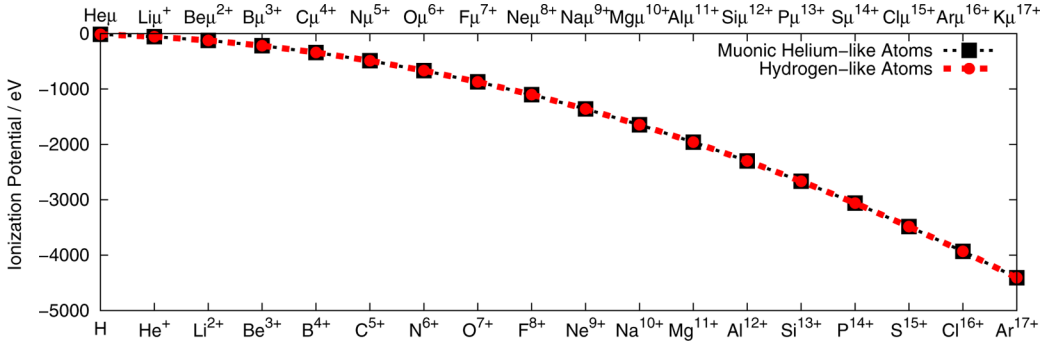

Figure 2. APMO/eFCI ionization potentials for hydrogen-like and muonic helium-like atoms. 31s25p:31s25p electron:muon basis sets were employed.

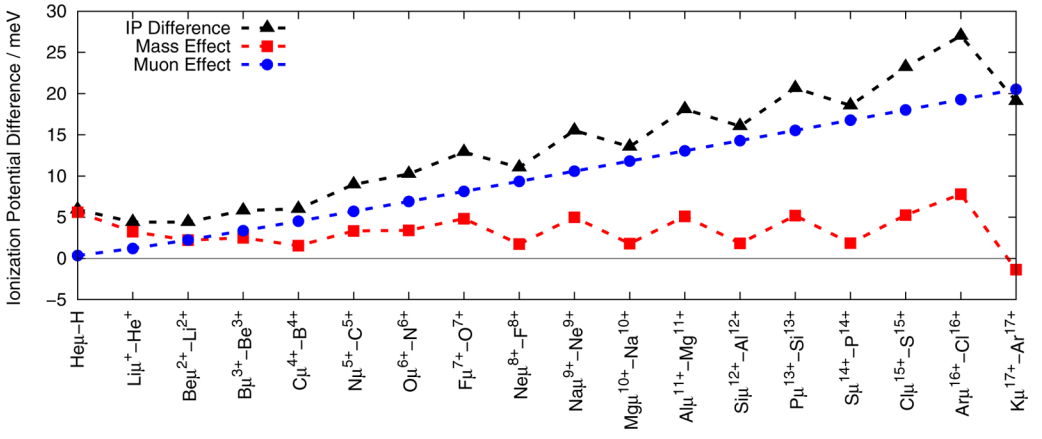

Figure 3. NMEs (red squares) and QMEs (blue circles) on the IP differences (black triangles) between muonic helium-like and regular hydrogen-like atoms (in meV).

and the IP difference is equal to

$$\begin{aligned}\Delta\mathrm{IP} &= \mathrm{IP}(^{\infty}\mathrm{Y}\mu e) - \mathrm{IP}(^{\infty}\mathrm{X}e) \\ &= \Delta K_{\mu} + \Delta V_{\mathrm{Y}\mu} + \Delta K_{e} + V_{\mathrm{X}e} - V_{\mathrm{Y}e} - V_{\mu e} - E^{\mathrm{corr}}_{\mu-e}\end{aligned} \tag{22}$$

We will refer to the difference in electronic potential energies as the partial screening effect, ΔV_s

$$\Delta V_{\mathrm{s}} = V_{\mathrm{X}e} - V_{\mathrm{Y}e} - V_{\mu e} \tag{23}$$

ΔK_{μ} and $\Delta V_{\mathrm{Y}\mu}$ are a result of the muon relaxation upon electronic removal, whereas ΔK_e and ΔV_s are a result of the imperfect screening of a positive nuclear charge exerted by the muonic density. Table 5 presents these values for muonic helium-like atoms from Z = 2−19.

For all the muonic helium-like atoms studied in Table 5 the muon relaxation terms, ΔK_{μ} and $\Delta V_{\mathrm{Y}\mu}$, compensate each other in such a way that their contribution to the QME is negligible.

The electronic contributions, ΔK_e and ΔV_s, to the IP difference are presented in Table 5. We observe that the partial screening effect is always positive and increases linearly with Z ranging from 1 to 81 meV. On the other hand, the kinetic energy change is negative and decreases linearly with Z, ranging from −1 to −60 meV. Furthermore, the partial screening effect is always larger in magnitude than the kinetic energy contribution. We also observe that these are the most important contributions to the QME.

From the fact that ΔV_s is positive we can conclude that from the electrons perspective the nucleus−muon moeity has an effective charge slightly larger than $Z - 1$.

Table 5. Contributions to the QMEs on the IPs of Muonic Helium-Like Atoms (Effects in meV)[a]

system	$-E^{\mathrm{corr}}_{\mu-e}$	ΔK_{μ}	$\Delta V_{\mathrm{Y}\mu}$	ΔK_e	ΔV_s
$^{\infty}\mathrm{He}\mu$	0.03	0.63	−0.63	−0.95	1.27
$^{\infty}\mathrm{Li}\mu^{+}$	0.08	2.24	−2.24	−3.36	4.48
$^{\infty}\mathrm{Be}\mu^{2+}$	0.11	4.24	−4.24	−6.37	8.50
$^{\infty}\mathrm{B}\mu^{3+}$	0.13	6.43	−6.43	−9.65	12.87
$^{\infty}\mathrm{C}\mu^{4+}$	0.15	8.71	−8.71	−13.08	17.45
$^{\infty}\mathrm{N}\mu^{5+}$	0.16	11.06	−11.06	−16.59	22.14
$^{\infty}\mathrm{O}\mu^{6+}$	0.17	13.44	−13.44	−20.16	26.91
$^{\infty}\mathrm{F}\mu^{7+}$	0.17	15.84	−15.84	−23.78	31.73
$^{\infty}\mathrm{Ne}\mu^{8+}$	0.18	18.27	−18.27	−27.41	36.59
$^{\infty}\mathrm{Na}\mu^{9+}$	0.18	20.70	−20.70	−31.07	41.47
$^{\infty}\mathrm{Mg}\mu^{10+}$	0.19	23.15	−23.15	−34.75	46.37
$^{\infty}\mathrm{Al}\mu^{11+}$	0.19	25.61	−25.61	−38.43	51.29
$^{\infty}\mathrm{Si}\mu^{12+}$	0.20	28.07	−28.07	−42.13	56.22
$^{\infty}\mathrm{P}\mu^{13+}$	0.20	30.53	−30.53	−45.83	61.16
$^{\infty}\mathrm{S}\mu^{14+}$	0.20	33.00	−33.00	−49.54	66.11
$^{\infty}\mathrm{Cl}\mu^{15+}$	0.20	35.48	−35.48	−53.25	71.07
$^{\infty}\mathrm{Ar}\mu^{16+}$	0.20	37.95	−37.95	−56.97	76.03
$^{\infty}\mathrm{K}\mu^{17+}$	0.21	40.43	−40.43	−60.69	81.00

[a] 31s25p:31s25p electronic:muonic basis sets.

Table 5 also presents the contribution of the muon−electron correlation to the IP of muonic helium-like atoms. These results reveal that this contribution increases with the atomic number, ranging from 0.03 to 0.21 meV. However, this

dx.doi.org/10.1021/jp501289s | J. Phys. Chem. A 2014, 118, 9491−9499

Table 6. APMO/eFCI Transition-State Coordinates, Reactants Energy, Transition-State Energy, and Reaction Barrier for the Heμ + H_2 and H + H_2 Reactions

	R_1/Å	R_2/Å	E(X+H_2)/au	E[X−H−H]‡/au	E_b/eV	QME/meV
			[cc-pVTZ:13s][a]			
$^{\infty}$H + $^{\infty}H_2$	0.9304	0.9304	−1.672266	−1.656465	0.42998	
$^{\infty}$Heμ + $^{\infty}H_2$	0.9305	0.9308	−415.101734	−415.085936	0.42991	−0.07
			[cc-pVTZ+11s:13s][a]			
$^{\infty}$H + $^{\infty}H_2$	0.9301	0.9301	−1.672649	−1.656848	0.42996	
$^{\infty}$Heμ + $^{\infty}H_2$	0.9301	0.9301	−415.102119	−415.086320	0.42990	−0.06
			[cc-pVTZ+11s:PP][b]			
$^{\infty}$H + $^{\infty}H_2$	0.9304	0.9304	−1.672266	−1.656465	0.42998	
$^{\infty}$Heμ + $^{\infty}H_2$	0.9304	0.9304	−1.672277	−1.656478	0.42992	−0.06

[a]Electronic:muonic basis sets. [b]Electronic basis set. Muon−electron interaction described using the pseudopotential proposed in ref 15.

contribution is very small compared to the partial screening discussed above.

We are now in a better position to evaluate the QME on the reaction energies.

QME on the Reaction Barrier of ^{4}Heμ + $^1H_2$. The NME on the reaction barrier of ^{4}Heμ + $^1H_2$ can be easily deduced by comparing the barriers of the $^{4.1}$H + $^1H_2$ and ^{1}H + $^1H_2$ reactions. However, it has been reported that the FNMC performs poorly close to critical points[18] and incorrectly predicts the lowering of the H + H_2 barrier height.[20] Therefore, we have calculated the NME from very accurate Born−Huang results previously reported for these reactions in refs 14 and 22. The Born−Huang PESs were obtained by adding the diagonal Born Oppernheimer correction (DBOC) to practically complete configuration interaction calculations. We will refer to these results as NME(ΔDBOC).

These studies reveal that the DBOC increases the $^{4.1}$H + $^1H_2$ and ^{1}H + $^1H_2$ reaction barriers by 5.64[14] and 6.66 meV,[22] respectively. From these results we deduced that the NME(ΔDBOC) reduces the barrier of the ^{4}Heμ + $^1H_2$ reaction by 1.02 meV when compared to that of ^{1}H + $^1H_2$ reaction.

We have already shown that QMEs and NMEs can be studied separately. Therefore, here we analyze the QME on the ^{4}Heμ + $^1H_2$ reaction barrier. To that aim, we calculated at the APMO/eFCI level the PESs for the $^{\infty}$H + $^{\infty}H_2$ and $^{\infty}$Heμ + $^{\infty}H_2$ collinear reactions assuming infinite nuclear mass. As pointed out in the previous section, the difference between both reaction barriers can only be attributed to the partial screening of the muon.

Table 6 presents APMO/eFCI results with the cc-pVTZ electronic basis set, and with the same basis set with 11 additional even-tempered s-type tight gaussians. Results presented in Table 6 reveal that the QME reduces the reaction barrier by 0.07 meV with the cc-pVTZ basis and by 0.06 meV with the cc-pVTZ basis, including the tight functions. This effect is 17 times smaller than the NME(ΔDBOC) discussed above and should be taken into account only if very accurate calculations are needed. For comparison, Table 6 presents the results calculated with the pseudopotential approach proposed by Fleming et al. in ref 15 using a cc-pVTZ electronic basis set. These results reveal that the QME reduces the reaction barrier by 0.06 meV. This result is in excellent agreement with the APMO/eFCI results discussed above. In contradiction to our results, ref 15 claims that the QME increases the barrier by 0.04 or 0.05 meV. However, these calculations are incorrect as a result of a missing negative sign in their pseudopotential.

We have evaluated the dependence of the QME on the choice of electronic basis set for the $^{\infty}$Heμ + $^{\infty}H_2$ barrier using APMO/HF calculations. We used several Dunning basis sets, including additional s-type tight Gaussians. Results presented in Table S.3 in the Supporting Information display weak dependence of the QME with the basis set choice, as these values range bewteen 0.05 and 0.07 meV.

Mielke et al.[40] proposed an equation to estimate the rate constant, k, of the H + H_2 reaction for given isotopologues using a DBOC calculation and the rate constant calculated with the BO approximation, k^{BO}.

$$k(T) = \exp\left(-\frac{\Delta E_b}{k_b T}\right) k^{BO}(T) \tag{24}$$

where ΔE_b is the difference of the BO barrier and the barrier including the DBOC. We can use this expression to calculate the kinetic isotope effect (KIE) by comparing the rate constants of the ^{1}H + $^1H_2$ and ^{4}Heμ + $^1H_2$ reactions. The resulting expression can be approximated using our estimates for the NME(ΔDBOC), −1.02 meV, and the QME, −0.06 meV.

$$\mathrm{KIE} = \frac{k(^1\mathrm{H})}{k(^4\mathrm{He}\mu)} = \exp\left(\frac{\Delta E_b(^4\mathrm{He}\mu) - \Delta E_b(^1\mathrm{H})}{k_b T}\right)\frac{k^{BO}(^1\mathrm{H})}{k^{BO}(^4\mathrm{He}\mu)}$$
$$\approx \exp\left(\frac{\mathrm{NME}}{k_b T}\right)\exp\left(\frac{\mathrm{QME}}{k_b T}\right)\mathrm{KIE}^{BO}$$

where KIE^{BO} is the kinetic isotope effect calculated from the BO PES.

This equation reveals that the NME(ΔDBOC) and the QME terms will increase the ^{4}Heμ reaction rate with respect to the ^{1}H reaction rate, because both contributions are negative. For instance, at 100 K the NME(ΔDBOC) and the QME terms increase the ^{4}Heμ reaction rate by 12.6% and 0.7%, respectively, whereas at 500 K the effects are smaller, as the NME(ΔDBOC) and the QME terms increase the ^{4}Heμ reaction rate by 2.4% and 0.1% respectively.

CONCLUDING REMARKS

We investigated the differences between the ionization energies of regular and muonic atoms with the nonrelativistic any particle molecular orbital method at the FCI level of theory.

We proposed a scheme to discriminate the contributions of the nuclear mass and the quantum muon effects to the differences on the chemical properties of muonic atoms and regular atoms.

dx.doi.org/10.1021/jp501289s | J. Phys. Chem. A 2014, 118, 9491−9499

Our results revealed that the differences in the ionization potentials of isoelectronic muonic atoms and regular atoms for elements with one and two electrons are of the order of millielectronvolts and become smaller with an increasing atomic number. Furthermore, for muonic helium and muonic lithium the nuclear mass effects are more important than the quantum muon effects.

On the other hand, our results for muonic helium-like atoms revealed that the quantum muon effects are more important than the nuclear mass effects for atoms with atomic number $Z > 3$.

Further analysis of the IPs of muonic helium-like atoms revealed that the most important contribution to the quantum muon effect is the imperfect muonic screening of the positive charge. Furthermore, the contributions of the muon−electron correlation and muon relaxation are negligible.

We quantified the quantum muon effect on the energy barrier of the $^{\infty}He\mu + {}^{\infty}H_2$ reaction using the same methodology. The partial muonic screening effect reduces the energy barrier of the $^{\infty}H + {}^{\infty}H_2$ reaction barrier by 0.06 meV. We deduced from accurate results presented in refs 14 and 22 that the nuclear mass effect (ΔDBOC) reduces the barrier of the $^4He\mu + {}^1H_2$ reaction by 1.02 meV when compared to that of $^1H + {}^1H_2$.

Although small in most chemical applications, nuclear mass and quantum muon effects should be considered in calculations aiming for spectroscopic accuracy.

■ ASSOCIATED CONTENT

Ⓢ Supporting Information

Table S.1 presents the 31s25p muonic and the 31s25p electronic basis sets exponents. Table S.2 presents the parameters used in the muonic-helium pseudopotential fitting. Table S.3 presents APMO/HF reactions barriers calculated with different electronic basis sets. Figure S.1 shows the muonic helium-electron pseudopotential. This material is available free of charge via the Internet at http://pubs.acs.org.

■ AUTHOR INFORMATION

Corresponding Author

*A. Reyes. E-mail: areyesv@unal.edu.co.

Notes

The authors declare no competing financial interest.

■ ACKNOWLEDGMENTS

We thank Jonathan Romero for helpful discussions. We gratefully acknowledge the support of Colciencias and UNAL (División Investigación Bogotá).

■ REFERENCES

(1) Jean, Y.; Mallon, P.; Schrader, D. *Principles and Applications of Positron & Positronium Chemistry*; World Scientific: Singapore, 2003.

(2) Nagamine, K. *Introductory Muon Science*; Cambridge University Press: Cambridge, U.K., 2003.

(3) Ponomarev, L. I. Muon Catalysed Fusion. *Contemp. Phys.* **1990**, *31*, 219−245.

(4) Froelich, P. Muon Catalysed Fusion Chemical Confinement of Nuclei Within the Muonic Molecule dtu. *Adv. Phys.* **1992**, *41*, 405−508.

(5) Ishida, K.; Nagamine, K.; Matsuzaki, T.; Kawamura, N. Muon Catalyzed Fusion. *J. Phys. G: Nucl. Part. Phys.* **2003**, *29*, 2043.

(6) Yamazaki, T.; Nagamine, K.; Nagamiya, S.; Hashimoto, O.; Sugimoto, K.; Nakai, K.; Kobayashi, S. Negative Moun Spin Rotation. *Phys. Scr.* **1975**, *11*, 133−139.

(7) Mallow, J. V.; Desclaux, J. P.; Freeman, A. J. Dirac-Fock Method for Muonic Atoms: Transition Energies, Wave Functions, and Charge Densities. *Phys. Rev. A* **1978**, *17*, 1804−1809.

(8) Nagamine, K. Negative Muon Spin Rotation in Solids. *Hyperfine Interact.* **1979**, *6*, 347−355.

(9) Yamazaki, T. Distribution of Electron Spin Densities Probed by Negative Muons. *Hyperfine Interact.* **1981**, *8*, 463−469.

(10) Mallow, J. V.; Desclaux, J. P.; Freeman, A. J.; Weinert, M. Relativistic Self-Consistent Field Theory for Muonic Atoms: The Muonic Hyperfine Anomaly. *Hyperfine Interact.* **1981**, *8*, 455−461.

(11) Torikai, E.; Nagamine, K.; Nishiyama, K.; Hirose, E.; Birrer, P.; Tanaka, I.; Kojima, H.; Srinivas, S.; Das, T.; Maekawa, S. Interaction of Paramagnetic Electron with High Tc Supercurrent in LaSrCuO Studied by (μ-O) Probe. *Hyperfine Interact.* **1996**, *97−98*, 387−394.

(12) Mamedov, T.; Andrianov, D.; Gerlach, D.; Gritsai, K.; Gorelkin, V.; Cormann, O.; Major, J.; Stoikov, A.; Shevchik, M.; Zimmerman, U. μ-spin Rotation Study of the Temperature-Dependent Relaxation Rate of Acceptor Centers in Silicon. *JETP Lett.* **2000**, *71*, 438−441.

(13) Arseneau, D. J.; Fleming, D. G.; Sukhorukov, O.; Brewer, J. H.; Garrett, B. C.; Truhlar, D. G. The Muonic He Atom and a Preliminary Study of the $^4He\mu + H_2$ Reaction. *Physica B* **2009**, *404*, 946−949.

(14) Fleming, D.; Arseneau, D.; Sukhorukov, O.; Brewer, J.; Mielke, S.; Schatz, G.; Garrett, B.; Peterson, K.; Truhlar, D. Kinetic Isotope Effects for the Reactions of Muonic Helium and Muonium with H2. *Science* **2011**, *331*, 448−450.

(15) Fleming, D. G.; Arseneau, D. J.; Sukhorukov, O.; Brewer, J. H.; Mielke, S. L.; Truhlar, D. G.; Schatz, G. C.; Garrett, B. C.; Peterson, K. A. Kinetics of the Reaction of the Heaviest Hydrogen Atom with H_2, the $^4He\mu + H_2 \rightarrow {}^4He\mu H + H$ reaction: Experiments, Accurate Quantal Calculations, and Variational Transition State Theory, Including Kinetic Isotope Effects for a Factor of 36.1 in Isotopic Mass. *J. Chem. Phys.* **2011**, *135*, 184310.

(16) Moncada, F.; Cruz, D.; Reyes, A. Muonic Alchemy: Transmuting Elements With the Inclusion of Negative Muons. *Chem. Phys. Lett.* **2012**, *539−540*, 209−213.

(17) Moncada, F.; Cruz, D.; Reyes, A. Electronic Properties of Atoms and Molecules Containing One and Two Negative Muons. *Chem. Phys. Lett.* **2013**, *570*, 16−21.

(18) Mohallem, J. R.; Diniz, L. G.; Dutra, A. S. Separation of Motions of Atomic Cores and Valence Electrons in Molecules. *Chem. Phys. Lett.* **2011**, *501*, 575−579.

(19) Gonçalves, C. P.; Mohallem, J. R. Self-Consistent-Field - Hartree-Fock Method With Finite Nuclear Mass Corrections. *Theor. Chem. Acc.* **2003**, *110*, 367−370.

(20) Gonçalves, C. P.; Mohallem, J. R. A New Algorithm to Handle Finite Nuclear Mass Effects in Electronic Calculations: The ISOTOPE Program. *J. Comput. Chem.* **2004**, *25*, 1736−1739.

(21) Mielke, S. L.; Schwenke, D. W.; Peterson, K. A. Benchmark calculations of the complete configuration-interaction limit of Born-Oppenheimer diagonal corrections to the saddle points of isotopomers of the $H+H_2$ reaction. *J. Chem. Phys.* **2005**, *122*, 224313.

(22) Mielke, S. L.; Schwenke, D. W.; Schatz, G. C.; Garrett, B. C.; Peterson, K. A. Functional Representation for the Born-Oppenheimer Diagonal Correction and Born-Huang Adiabatic Potential Energy Surfaces for Isotopomers of H_3. *J. Phys. Chem. A* **2009**, *113*, 4479−4488.

(23) González, S.; Aguirre, N.; Reyes, A. Theoretical Investigation of Isotope Effects: The Any-Particle Molecular Orbital Code. *Int. J. Quantum Chem.* **2008**, *108*, 1742−1749.

(24) González, S.; Reyes, A. Nuclear Quantum Effects on the He_2H^+ Complex With the Nuclear Molecular Orbital Approach. *Int. J. Quantum Chem.* **2010**, *110*, 689−696.

(25) Nakai, H.; Sodeyama, K.; Hoshino, M. Non-Born-Oppenheimer Theory for Simultaneous Determination of Vibrational and Electronic Excited States: ab Initio NO+MO/CIS Theory. *Chem. Phys. Lett.* **2001**, *345*, 118−124.

(26) Nakai, H. Simultaneous determination of nuclear and electronic wave functions without Born-Oppenheimer approximation: Ab initio NO+ MO/HF theory. *Int. J. Quantum Chem.* **2002**, *86*, 511−517.
(27) Nakai, H. Nuclear Orbital Plus Molecular Orbital Theory: Simultaneous Determination of Nuclear and Electronic Wave Functions Without Born-Oppenheimer Approximation. *Int. J. Quantum Chem.* **2007**, *107*, 2849−2869.
(28) Tachikawa, M.; Osamura, Y. Simultaneous Optimization of Exponents, Centers of Gaussian-type Basis Functions, and Geometry With Full-Configuration Interaction Wave Function: Application to the Ground and Excited States of Hydrogen Molecule. *J. Chem. Phys.* **2000**, *113*, 4942.
(29) Tachikawa, M. Multi-component Molecular Orbital Theory for Electrons and Nuclei Including Many-Body Effect With Full Configuration Interaction Treatment: Isotope Effects on Hydrogen Molecules. *Chem. Phys. Lett.* **2002**, *360*, 494−500.
(30) Ishimoto, T.; Tachikawa, M.; Nagashima, U. Simultaneous Analytical Optimization of Variational Parameters in Gaussian-Type Functions With Full Configuration Interaction of Multicomponent Molecular Orbital Method by Elimination of Translational and Rotational Motions: Application to Isotopomers of the Hydrogen Molecule. *J. Chem. Phys.* **2008**, *128*, 164118.
(31) Takahashi, S.; Takatsuka, K. On the Validity Range of the Born-Oppenheimer Approximation: A semiclassical Study for All-Particle Quantization of Three-Body Coulomb Systems. *J. Chem. Phys.* **2006**, *124*, 144101.
(32) Flores-Moreno, R.; Posada, E.; Moncada, F.; Romero, J.; Charry, J.; Díaz-Tinoco, M.; González, S. A.; Aguirre, N. F.; Reyes, A. LOWDIN: The Any Particle Molecular Orbital Code. *Int. J. Quantum Chem.* **2014**, *114*, 50−56.
(33) Knowles, P. J.; Handy, N. C. A Determinant Based Full Configuration Interaction Program. *Comput. Phys. Commun.* **1989**, *54*, 75−83.
(34) T.H. Dunning, J. Gaussian Basis Sets for Use in Correlated Molecular Calculations. I. The Atoms Boron Through Neon and Hydrogen. *J. Chem. Phys.* **1989**, *90*, 1007.
(35) Woon, D.; T.H. Dunning, J. Gaussian Basis Sets for Use in Correlated Molecular Calculations. IV. Calculation of Static Electrical Response Properties. *J. Chem. Phys.* **1994**, *100*, 2975.
(36) Woon, D.; T.H. Dunning, J. Gaussian Basis Sets for Use in Correlated Molecular Calculations. III. The Atoms Aluminum Through Argon. *J. Chem. Phys.* **1993**, *98*, 1358.
(37) Frolov, A. M. Properties and Hyperfine Structure of Helium-Muonic Atoms. *Phys. Rev. A* **2000**, *61*, 022509.
(38) Lias, S. G. In *CRC Handbook of Chemistry and Physics*; Lide, D. R., Ed.; CRC Press: Boca Raton, FL, 2010; pp 10−206.
(39) Klopper, W.; Bachorz, R. A.; Tew, D. P.; Hättig, C. Sub-meV accuracy in first-principles computations of the ionization potentials and electron affinities of the atoms H to Ne. *Phys. Rev. A* **2010**, *81*, 022503.
(40) Mielke, S. L.; Peterson, K. A.; Schwenke, D. W.; Garrett, B. C.; Truhlar, D. G.; Michael, J. V.; Su, M.-C.; Sutherland, J. W. H+H_2 Thermal Reaction: A Convergence of Theory and Experiment. *Phys. Rev. Lett.* **2003**, *91*, 063201.

D. Paper IV

The Any Particle Molecular Orbital Grid-based Hartree-Fock (APMO-GBHF) Approach

Edwin Posada[1] and Andrés Reyes[1, a)]

Department of Chemistry, Universidad Nacional de Colombia

(Dated: 7 November 2017)

The any particle molecular orbital grid-based Hartree-Fock approach (APMO-GBHF) is proposed as an initial step to perform multi-component (MC) post-Hartree-Fock, explicitly correlated, and density functional theory methods without basis set errors. The method has been applied to a number of electronic and multi-species molecular systems. Results of these calculations show that the APMO-GBHF total energies are comparable with those obtained at the APMO-HF complete basis set limit. In addition, results reveal a considerable improvement in the description of the nuclear cusps of electronic and non-electronic densities.

Keywords: Grid-based methods, multi-component methods, exotic systems, non-Born-Oppenheimer

[a)]Electronic mail: areyesv@unal.edu.co.

I. INTRODUCTION

In recent decades, a number of theoretical methodologies have been developed to extend regular electronic structure methods to study atomic and molecular systems comprising electrons and other quantum species.[1–6] These multi-component (MC) methodologies have emerged as alternative choices for describing nuclear quantum effects beyond the Born-Oppenheimer approximation (BOA) such as isotope effects, nuclear delocalization and tunneling in hydrogen-containing molecules and hydrogen-bonded systems. Comprehensive reviews of MC methodologies can be found in references.[7,8]

In addition, MC methodologies have been used to analyze exotic molecules (*i.e.* molecular systems containing subatomic particles such as positrons, muons, among others).[2,9–20] For instance, calculations for muonic atoms (*i.e.* atoms in which one electron has been replaced with a muon) were carried out at MC-CI level of theory.[14,16] Also, studies for the positron binding energies of the 20 standard amino acids at MC-PT2 (generalized second order propagator) level of theory.[19,20] In such calculations, electrons, muons and positrons were described quantum-mechanically while atomic nuclei were considered as point charges under the BOA.

The application of the MC methods have unveiled major pitfalls in the MC description of the quantum state of these exotic systems. The source of these problems can be linked to one of the following: (a) the lack of inter-species correlation, which cannot be efficiently recovered with the use of MC-post HF extensions,[21] (b) the truncation of the basis set (*i.e.* the basis set incompleteness) which can lead to the inability to properly describe the inter-species cusps.[22]

In regards to (a), the description of the inter-species correlation can be improved by including the explicit dependence of the interparticle distances in terms of Gaussian-type geminal functions within a explicitly correlated MC approach (MC-XCHF).[21,23–28] Respecting (b), to the best of our knowledge, the basis set related limitations have not been properly addressed. This is the main focus of the present contribution.

Regularly, MC methods are derived as extensions of conventional electronic structure methods. As a consequence, current MC approaches rely on Gaussian basis functions (Gaussian-type orbitals (GTOs)) for the representation of MC wavefunction. This is in principle an obvious choice, since all the required integrals in MC calculations can be ob-

tained directly from the same routines employed in regular electronic structure methods.[2,29]

However, it has been observed repeatedly in MC studies that GTOs are not ideal for representing the wavefunctions of the different quantum species. For instance, since densities are strongly peaked at clamped nuclei, a superposition of several GTOs (*i.e.* a linear combination of GTOs) is required for a satisfactory representation of densities and single-particle orbitals. The need of a linear combination of GTOs may reduce the efficiency of the method and, in the case of superpositions of large numbers of functions, may result in numerical instabilities.[30]

Furthermore, finding an adequate basis set to represent non-electronic particles within MC models poses additional challenges, since there are not well established and physically motivated hierarchies for this purpose such as in the electronic counterpart. For instance, in the case of positronic atoms and molecules, basis set coefficients, exponent and centers are usually individually crafted for each system following physical or chemical intuition. This is due to the strong dependence of the basis set on the chemical environment.[2,15,31–33]

Moreover, the use of GTOs with fixed exponents and positions is not sufficiently adequate for studying systems containing quantum particles with non-standard masses. In such cases, it is necessary to use *mobile* functions (*i.e.* Gaussian functions in which exponents, positions, and linear coefficients are optimized variationally during the MC SCF procedure).[34]

The main goal of this contribution is to face these basis set related issues by proposing a grid-based representation of the wavefunction in MC methodologies as an alternative to GTOs. This contribution may be viewed as an initial step to realizing MC- MC-post-HF, MC-XCHF, or MC Density Functional Theory (MC-DFT) methods without basis set induced errors.

To this aim, we propose the Any-Particle Molecular Orbital Grid-Based Hartree-Fock (APMO-GBHF) approach. This method is along the lines of that of Becke and Dickson[35]: We expand orbitals and potentials in Becke's multicenter grid to solve Poisson's equation (to obtain the Coulomb, exchange and coupling potentials), and to represent the action of the Laplace operator in both kinetic operator and Laplace equation. We expect our methodology to provide an improved representation of the ground-state densities and single-particle orbitals.

This paper is organized as follows, in the next section, we provide some details of the theory and computational implementation. In the Results section, we report the numerical

grid-based Hartree-Fock (GBHF) solutions of a number of electronic and multi-species systems compared to their analytical HF and APMO-HF limit solution. Finally, we provide some concluding remarks and perspectives.

II. METHODOLOGY

A. APMO-HF Theory

Here, we summarize the equations of the APMO Hartree-Fock (APMO-HF) approach.[6] Let us consider a system containing N^Q fermionic quantum particles and N^C point charge nuclei. The Hamiltonian, H, of this system is written in terms of kinetic and potential energy operators as

$$H = -\sum_{i}^{N^Q} \frac{1}{2M_i}\nabla^2 + \sum_{i}^{N^Q}\sum_{j>i}^{N^Q} \frac{q_i q_j}{\mathbf{r}_{ij}} + \sum_{i}^{N^Q}\sum_{j}^{N^C} \frac{q_i q_j}{\mathbf{r}_{ij}} + \sum_{i}^{N^C}\sum_{j>i}^{N^C} \frac{q_i q_j}{\mathbf{r}_{ij}}, \quad (1)$$

here, q_i is the charge of particle i. At the APMO-HF level of theory, the molecular wave-function, Ψ_0, is expressed as a product of single-configurational wave-functions, Φ^α, for each type of quantum species α:

$$\Psi_0 = \prod_{\alpha}^{N^{species}} \Phi^\alpha. \quad (2)$$

Here, each Φ^α is expressed in terms of molecular orbitals (MOs) ψ_i^α, obtained by solving the Fock equations

$$f^\alpha(i)\psi_i^\alpha = \varepsilon_i^\alpha \psi_i^\alpha. \quad (3)$$

The effective one-particle HF operator, f^α, is expressed as

$$f^\alpha(i) = h^\alpha(i) + q_\alpha^2 \sum_{j\in\alpha}[J_j^\alpha - K_j^\alpha] + q_\alpha \sum_{\beta\neq\alpha}^{N^Q} q_\beta \sum_{j\in\beta} J_j^\beta, \quad (4)$$

where h^α is the one-particle core Hamiltonian,

$$h^\alpha(i) = -\frac{\nabla_i^2}{2M_\alpha} + \sum_{j}^{N^C} \frac{q_\alpha q_j}{|\mathbf{r}_i - \mathbf{R}_j|}, \quad (5)$$

and J and K are Coulomb and exchange operators, defined as

$$J^\gamma(1)\psi_i^\alpha(1) = \left[\int d\mathbf{r}_2 \psi_j^{\gamma*}(2)\frac{1}{\mathbf{r}_{12}}\psi_j^\gamma(2)\right]\psi_i^\alpha(1), \quad (6)$$

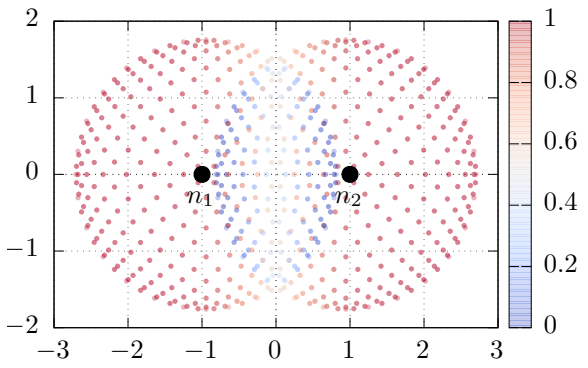

FIG. 1. Two overlapped spherical grids with centers n_1 and n_2 with their corresponding $w_n(\mathbf{r})$ values (color-bar)

for $\gamma = \alpha, \beta$, and

$$K^{\alpha}(1)\psi_i^{\alpha}(1) = \left[\int d\mathbf{r}_2 \psi_j^{\alpha *}(2)\frac{1}{\mathbf{r}_{12}}\psi_i^{\alpha}(2)\right]\psi_j^{\alpha}(1). \tag{7}$$

Equation 4 shows that the effective field experienced by one quantum species depends on the MOs of the remaining ones.

B. Grid-Based HF

Here, we summarize the key aspects of this approach. Further details can be found in references.[35–38]

1. Multicenter numerical integration

Any multicenter molecular function, $F(\mathbf{r})$, can be decomposed as a sum of single-center components, $F_n(\mathbf{r})$:

$$F(\mathbf{r}) = \sum_n F_n(\mathbf{r}). \tag{8}$$

These $F_n(\mathbf{r})$ are calculated multiplying function $F(\mathbf{r})$ by a set of n-centered relative weight functions$w_n(\mathbf{r})$, as follows

$$F_n(\mathbf{r}) = F(\mathbf{r})w_n(\mathbf{r}). \tag{9}$$

Each $w_n(\mathbf{r})$ has unit value in the vicinity of its center and vanishes uniformly in the proximity of other centers. Figure 1 illustrates the behavior of the relative weight function $w_n(\mathbf{r})$.

The integral of $F(\mathbf{r})$, thus, can be simplified to the integration of single-center components. Consequently, the total integral can be expressed as,

$$\int F(\mathbf{r})d\mathbf{r} = \sum_n \int F_n(\mathbf{r})d\mathbf{r} = \sum_n I_n \tag{10}$$

Each single-center integral I_n, is calculated numerically in a spherical coordinate system centered at n, more explicitly

$$I_n = \iiint F_n(r, \vartheta, \varphi) r^2 \sin\vartheta dr d\vartheta d\varphi. \tag{11}$$

This three-dimensional integral can be computed by using Gauss-type quadratures for two-dimensional integration on the surface of a unit sphere. Therefore, the integral of equation 11 can be rewritten as

$$I_n = \iint F_n(r, \Omega) r^2 dr d\Omega \tag{12}$$

where Ω denotes the solid angle. The solid-angle integration is carried out by using Lebedev grids,[39] which are designed to integrate exactly spherical harmonics ($Y_{\ell m}$) up to $\ell = 35$.

The radial integration is performed using Gauss-Chebyshev quadrature of the second kind. However, the regular Gauss-Chebyshev integration interval $-1 < x < +1$, must be mapped into the semi-infinite interval $0 < r < \infty$. This mapping is accomplished through the coordinate transformation

$$r = r_m \frac{1+x}{1-x}, \tag{13}$$

where r_m takes a value of 1/2 the atomic radius for all atoms[40] except for hydrogen, in which case the factor 1/2 is not applied.

2. Numerical solution of Poisson's equation

The Poisson's equation for a potential $V(\mathbf{r})$ of an arbitrary density distribution $\rho(\mathbf{r})$ is defined as,

$$\nabla^2 V(\mathbf{r}) = -4\pi\rho(\mathbf{r}). \tag{14}$$

Solving equation 14 is equivalent to solving the integral

$$V(\mathbf{r}_2) = \int \frac{\rho(\mathbf{r}_1)}{\mathbf{r}_{12}} d\mathbf{r}_1 \tag{15}$$

for all points $\mathbf{r}_2$. Combining the solution of the Poisson's equation and the multi-center numerical integration presented above, the two-center integrals, *e.g.*, the expectation values of equation 6

$$\langle\psi_i^\alpha(\mathbf{r}_1)|J_j^\alpha(\mathbf{r}_1)|\psi_i^\alpha(\mathbf{r}_1)\rangle = \langle ij|ij\rangle = \int \psi_i^{\alpha*}(\mathbf{r}_1)\psi_j^{\alpha*}(\mathbf{r}_2)\frac{1}{\mathbf{r}_{12}}\psi_i^\alpha(\mathbf{r}_1)\psi_j^\alpha(\mathbf{r}_2)d\mathbf{r}_1 d\mathbf{r}_2 \tag{16}$$

can be calculated first solving the Poisson's equation for potential $V_{ii}(2)$ of charge distribution $\psi_i^\alpha(\mathbf{r}_1)\psi_i^{\alpha*}(\mathbf{r}_1)$ and then evaluating the integral

$$\langle ij|ij\rangle = \int V_{ii}(\mathbf{r}_2)\psi_j^\alpha(\mathbf{r}_2)\psi_j^{\alpha*}(\mathbf{r}_2)d\mathbf{r}_2. \tag{17}$$

To solve equation 14, charge distribution $\rho(\mathbf{r}_1)$, ρ for simplification, has to be decomposed into single-center components as shown in equation 9, that is

$$\rho_n = \rho w_n. \tag{18}$$

Each single-center charge distribution leads to n single-center Poisson's equations of the form

$$\nabla^2 V^{(n)} = -4\pi\rho_n \tag{19}$$

so that the total potential V can be calculated by summing over all $V^{(n)}$potentials. It is worth stressing that the single-center $V^{(n)}$s are not related to $V$by the decomposition of equation 9, hence index $n$is superscripted to avoid possible confusion. To solve equation 19 the single-center charge distribution is expressed a multi-polar expansion[36]

$$\rho_n(r,\vartheta,\varphi) = \sum_{\ell m}\rho_{\ell m}(r)Y_{\ell m}(\vartheta,\varphi) \tag{20}$$

where $Y_{\ell m}(\vartheta,\varphi)$ is a real spherical harmonic function and $\rho_{\ell m}(r)$ is a function of the r variable. $\rho_{\ell m}(r)$ functions can be calculated by considering the orthogonality of the spherical expansion as follows

$$\rho_{\ell m}(r) = \int_\Omega \rho_n(r,\vartheta,\varphi)Y_{\ell m}(\vartheta,\varphi)d\Omega. \tag{21}$$

These integrals can be calculated by using the aforementioned Lebedev quadratures.[39] In principle, the multipolar expansion is infinite; however, the truncation order of the expansion $l_{\max}$ has been chosen to be 1/2 of the order of the Lebedev quadrature l_{quad}

$$l_{\max} = l_{quad}/2 \tag{22}$$

Bibliography

[1] A. D. Becke and R. M. Dickson, "Numerical solution of Schrödinger's equation in polyatomic molecules", The Journal of Chemical Physics **92**, 3610–3612 (1990).

[2] I. L. Thomas, "Protonic Structure of Molecules. I. Ammonia Molecules", Physical Review **185**, 90–94 (1969).

[3] M. Tachikawa, K. Mori, H. Nakai, and K. Iguchi, "An extension of ab initio molecular orbital theory to nuclear motion", Chemical Physics Letters **290**, 437–442 (1998).

[4] H. Nakai, "Simultaneous determination of nuclear and electronic wave functions without Born-Oppenheimer approximation: Ab initio NO+MO/HF theory", International Journal of Quantum Chemistry **86**, 511–517 (2002).

[5] T. Ishimoto, M. Tachikawa, and U. Nagashima, "Review of multicomponent molecular orbital method for direct treatment of nuclear quantum effect", International Journal of Quantum Chemistry **109**, 2677–2694 (2009).

[6] S. A. González, N. F. Aguirre, and A. Reyes, "Theoretical investigation of isotope effects: The any-particle molecular orbital code", International Journal of Quantum Chemistry **108**, 1742–1749 (2008).

[7] S. P. Webb, T. Iordanov, and S. Hammes–Schiffer, "Multiconfigurational nuclear-electronic orbital approach: Incorporation of nuclear quantum effects in electronic structure calculations", The Journal of Chemical Physics **117**, 4106–4118 (2002).

[8] N. F. Aguirre, P. Villarreal, G. Delgado-Barrio, E. Posada, A. Reyes, M. Biczysko, A. O. Mitrushchenkov, and M. P. de Lara-Castells, "Including nuclear quantum effects into highly correlated electronic structure calculations of weakly bound systems", The Journal of Chemical Physics **138**, 184113 (2013).

[9] I. L. Thomas and H. W. Joy, "Protonic Structure of Molecules. II. Methodology, Center-of-Mass Transformation, and the Structure of Methane, Ammonia, and Water", Physical Review A **2**, 1200–1208 (1970).

[10] M. Tachikawa and Y. Osamura, "Isotope effect of hydrogen and lithium hydride molecules. Application of the dynamic extended molecular orbital method and energy component analysis", Theoretical Chemistry Accounts: Theory, Computation, and Modeling (Theoretica Chimica Acta) **104**, 29–39 (2000).

[11] T. Iordanov and S. Hammes–Schiffer, "Vibrational analysis for the nuclear–electronic orbital method", The Journal of Chemical Physics **118**, 9489–9496 (2003).

[12] M. V. Pak, C. Swalina, S. P. Webb, and S. Hammes-Schiffer, "Application of the nuclear–electronic orbital method to hydrogen transfer systems: multiple centers and multiconfigurational wavefunctions", Chemical Physics **304**, 227–236 (2004).

[13] M. V. Pak and S. Hammes–Schiffer, "Electron–Proton Correlation for Hydrogen Tunneling Systems", Physical Review Letters **92**, 103002 (2004).

[14] A. Reyes, M. V. Pak, and S. Hammes–Schiffer, "Investigation of isotope effects with the nuclear–electronic orbital approach", The Journal of Chemical Physics **123**, 064104 (2005).

[15] J. H. Skone, M. V. Pak, and S. Hammes–Schiffer, "Nuclear–electronic orbital nonorthogonal configuration interaction approach", The Journal of Chemical Physics **123**, 134108 (2005).

[16] C. Swalina and S. Hammes–Schiffer, "Impact of Nuclear Quantum Effects on the Molecular Structure of Bihalides and the Hydrogen Fluoride Dimer", The Journal of Physical Chemistry A **109**, 10410–10417 (2005).

[17] A. D. Bochevarov, E. F. Valeev, and C. David Sherrill, "The electron and nuclear orbitals model: current challenges and future prospects", Molecular Physics **102**, 111–123 (2004).

[18] H. Nakai, K. Sodeyama, and M. Hoshino, "Non-Born–Oppenheimer theory for simultaneous determination of vibrational and electronic excited states: ab initio NO+MO/CIS theory", Chemical Physics Letters **345**, 118–124 (2001).

[19] H. Nakai and K. Sodeyama, "Many-body effects in nonadiabatic molecular theory for simultaneous determination of nuclear and electronic wave functions: Ab initio NOMO/MBPT and CC methods", The Journal of Chemical Physics **118**, 1119–1127 (2003).

[20] H. Nakai, M. Hoshino, K. Miyamoto, and S. Hyodo, "Elimination of translational and rotational motions in nuclear orbital plus molecular orbital theory", The Journal of Chemical Physics **122**, 164101 (2005).

[21] H. Nakai, "Nuclear orbital plus molecular orbital theory: Simultaneous determination of nuclear and electronic wave functions without Born–Oppenheimer approximation", International Journal of Quantum Chemistry **107**, 2849–2869 (2007).

[22] C. Swalina, M. V. Pak, A. Chakraborty, and S. Hammes–Schiffer, "Explicit Dynamical Electron–Proton Correlation in the Nuclear–Electronic Orbital Framework", The Journal of Physical Chemistry A **110**, 9983–9987 (2006).

[23] S. A. González and A. Reyes, "Nuclear quantum effects on the He 2H+ complex with the nuclear molecular orbital approach", International Journal of Quantum Chemistry **110**, 689–696 (2010).

[24] F. Moncada, S. A. González, and A. Reyes, "First principles investigation of hydrogen isotope effects in [XSO4-H-SO4X]- (X = H, K) complexes", Molecular Physics **108**, 1545–1552 (2010).

[25] F. Moncada, D. Cruz, and A. Reyes, "Muonic alchemy: Transmuting elements with the inclusion of negative muons", Chemical Physics Letters **539-540**, 209–213 (2012).

[26] R. Flores–Moreno, V. G. Zakrzewski, and J. V. Ortiz, "Assessment of transition operator reference states in electron propagator calculations", The Journal of Chemical Physics **127**, 134106 (2007).

[27] R. Flores-Moreno, E. Posada, F. Moncada, J. Romero, J. A. Charry, M. Díaz-Tinoco, S. A. González, N. F. Aguirre, and A. Reyes, "LOWDIN: The any particle molecular orbital code", International Journal of Quantum Chemistry **114**, 50–56 (2014).

[28] J. Romero, E. Posada, R. Flores-Moreno, and A. Reyes, "A generalized any particle propagator theory: Assessment of nuclear quantum effects on electron propagator calculations", The Journal of Chemical Physics **137**, 074105 (2012).

[29] Springer Nature, *Exotic atoms and molecules*, (2017) `https://www.nature.com/subjects/exotic-atoms-and-molecules` (visited on 05/15/2017).

[30] S. L. Saito, "Is positronium hydride atom or molecule?", Nuclear Instruments and Methods in Physics Research Section B: Beam Interactions with Materials and Atoms **171**, 60–66 (2000).

[31] J. A. Charry, J. Romero, M. T. d. N. Varella, and A. Reyes, "Calculation of positron binding energies of amino acids with the any-particle molecular-orbital approach", Physical Review A **89**, 052709 (2014).

[32] J. Romero, J. A. Charry, R. Flores-Moreno, M. T. d. N. Varella, and A. Reyes, "Calculation of positron binding energies using the generalized any particle propagator theory", The Journal of Chemical Physics **141**, 114103 (2014).

[33] A. D. Becke, "A multicenter numerical integration scheme for polyatomic molecules", The Journal of Chemical Physics **88**, 2547–2553 (1988).

[34] A. Szabo and N. S. Ostlund, *Modern Quantum Chemistry: Introduction to Advanced Electronic Structure Theory*, Dover Books on Chemistry (Dover Publications, 1989).

[35] L. Laaksonen, D. Sundholm, and P. Pyykkö, "Two-Dimensional, fully numerical molecular calculations. IV. hartree-fock-slater results on second-row diatomic molecules", International Journal of Quantum Chemistry **27**, 601–612 (1985).

[36] J. Kobus, "A finite difference Hartree–Fock program for atoms and diatomic molecules", Computer Physics Communications **184**, 799–811 (2013).

[37] P. M. Boerrigter, G. Te Velde, and J. E. Baerends, "Three-dimensional numerical integration for electronic structure calculations", International Journal of Quantum Chemistry **33**, 87–113 (1988).

[38] H. Murakami, V. Sonnad, and E. Clementi, "A three-dimensional finite element approach towards molecular SCF computations", International Journal of Quantum Chemistry **42**, 785–817 (1992).

[39] S. a. Losilla, M. a. Watson, A. Aspuru-Guzik, and D. Sundholm, "Construction of the Fock Matrix on a Grid-Based Molecular Orbital Basis Using GPGPUs", Journal of Chemical Theory and Computation **11**, 2053–2062 (2015).

[40] J. M. Pérez-Jordá and E. San-Fabián, "A simple, efficient and more reliable scheme for automatic numerical integration", Computer Physics Communications **77**, 46–56 (1993).

[41] J. M. Pérez-Jordá, E. San-Fabián, and F. Moscardó, "A simple, reliable and efficient scheme for automatic numerical integration", Computer Physics Communications **70**, 271–284 (1992).

[42] J. M. Pérez-Jordá, A. D. Becke, and E. San-Fabián, "Automatic numerical integration techniques for polyatomic molecules", The Journal of Chemical Physics **100**, 6520–6534 (1994).

[43] J. M. Pérez-Jordá, "Automatic numerical integration techniques for polyatomic molecules. Backward trimming", The Journal of Chemical Physics **101**, 1738–1740 (1994).

[44] M. Krack and A. M. Köster, "An adaptive numerical integrator for molecular integrals", The Journal of Chemical Physics **108**, 3226–3234 (1998).

[45] A. M. Köster, R. Flores-Moreno, and J. U. Reveles, "Efficient and reliable numerical integration of exchange-correlation energies and potentials", The Journal of Chemical Physics **121**, 681–690 (2004).

[46] B. Cordero, V. Gómez, A. E. Platero-Prats, M. Revés, J. Echeverría, E. Cremades, F. Barragán, and S. Alvarez, "Covalent radii revisited", Dalton Transactions, 2832 (2008).

[47] V. Lebedev, "Quadratures on a sphere", eng, USSR Computational Mathematics and Mathematical Physics **16**, 10–24 (1976).

[48] W. J. Hehre, R. Ditchfield, and J. A. Pople, "Self-Consistent Molecular Orbital Methods. XII. Further Extensions of Gaussian-Type Basis Sets for Use in Molecular Orbital Studies of Organic Molecules", The Journal of Chemical Physics **56**, 2257–2261 (1972).

[49] A. D. Becke and R. M. Dickson, "Numerical solution of Poisson's equation in polyatomic molecules", The Journal of Chemical Physics **89**, 2993–2997 (1988).

[50] W. J. Hehre, R. F. Stewart, and J. A. Pople, "Self-Consistent Molecular-Orbital Methods. I. Use of Gaussian Expansions of Slater-Type Atomic Orbitals", The Journal of Chemical Physics **51**, 2657–2664 (1969).

[51] E. F. Valeev, *A library for the evaluation of molecular integrals of many-body operators over Gaussian functions*, (2017) http://libint.valeyev.net/ (visited on 05/05/2017).

[52] T. Shiozaki and S. Hirata, "Grid-based numerical Hartree-Fock solutions of polyatomic molecules", Physical Review A **76**, 040503 (2007).

[53] J. F. Epperson, "On the Runge Example", The American Mathematical Monthly **94**, 329 (1987).

[54] T. Clark, J. Chandrasekhar, G. W. Spitznagel, and P. V. R. Schleyer, "Efficient diffuse function-augmented basis sets for anion calculations. III. The 3-21+G basis set for first-row elements, Li-F", Journal of Computational Chemistry **4**, 294–301 (1983).

[55] R. Celeste, H. da Costa, A. da Silva, and M. Trsic, "On the helium ground-state Hartree-Fock energy", Chemical Physics Letters **183**, 31–33 (1991).

[56] J. Kobus, "Finite-difference versus finite-element methods", Chemical Physics Letters **202**, 7–12 (1993).

[57] A. M. Frolov and D. M. Wardlaw, "Properties and hyperfine structure of the beryllium-muonic atoms", Journal of Physics B: Atomic, Molecular and Optical Physics **40**, 4179–4186 (2007).

[58] E. Posada, F. Moncada, and A. Reyes, "Negative Muon Chemistry: The Quantum Muon Effect and the Finite Nuclear Mass Effect", The Journal of Physical Chemistry A **118**, 9491–9499 (2014).

[59] D. J. Arseneau, D. G. Fleming, Y. Li, J. Li, Y. V. Suleimanov, and H. Guo, "Rate Coefficient for the 4 Heμ + CH 4 Reaction at 500 K: Comparison between Theory and Experiment", The Journal of Physical Chemistry B **120**, 1641–1648 (2016).

[60] S. van der Walt, S. C. Colbert, and G. Varoquaux, "The NumPy Array: A Structure for Efficient Numerical Computation", Computing in Science & Engineering **13**, 22–30 (2011).

[61] E. Jones, T. Oliphant, P. Peterson, et al., *SciPy: Open source scientific tools for Python*, (2015) http://www.scipy.org/ (visited on 12/01/2015).

[62] J. D. Hunter, "Matplotlib: A 2D Graphics Environment", Computing in Science & Engineering **9**, 90–95 (2007).

[63] E. Posada, *nAPMO's Documentation*, (2015) http://efposadac.github.io/nAPMO/index.html (visited on 11/18/2015).

[64] Intel Corporation, *Intel VTune Amplifier 2016*, (2015) https://software.intel.com/en-us/intel-vtune-amplifier-xe (visited on 11/24/2015).

[65] G. M. Amdahl, "Computer Architecture and Amdahl's Law", Computer **46**, 38–46 (2013).

[66] NVIDIA Corporation, *CUDA Toolkit Documentation v7.5*, (2015) http://docs.nvidia.com/cuda/index.html (visited on 11/25/2015).

[67] E. Posada, F. Moncada, and A. Reyes, "Optimization of Software Package for Studies of Quantum Nuclear Effects: APMO", Revista Colombiana de Química **40**, 35–45 (2011).

[68] R. Flores-Moreno, J. M. del Campo, and T. Ida, *Parakata*, (2008) https://sites.google.com/site/gdlquantumchemistrygroup/home/software/ (visited on 06/21/2013).

[69] D. G. Fleming, D. J. Arseneau, O. Sukhorukov, J. H. Brewer, S. L. Mielke, G. C. Schatz, B. C. Garrett, K. a. Peterson, and D. G. Truhlar, "Kinetic Isotope Effects for the Reactions of Muonic Helium and Muonium with H2", Science **331**, 448–450 (2011).